

**NANOSECOND OPTICAL PARAMETRIC
OSCILLATORS GENERATING
EYE-SAFE RADIATION**

**A THESIS
SUBMITTED TO THE DEPARTMENT OF ELECTRICAL AND
ELECTRONICS ENGINEERING
AND THE INSTITUTE OF ENGINEERING AND SCIENCES
OF BILKENT UNIVERSITY
IN PARTIAL FULFILLMENT OF THE REQUIREMENTS
FOR THE DEGREE OF
MASTER OF SCIENCE**

**By
Lütfiye Durak
October 1998**

**TK
7822
.07
D87
1998**

NANOSECOND OPTICAL PARAMETRIC
OSCILLATORS GENERATING EYE-SAFE RADIATION

A THESIS

SUBMITTED TO THE DEPARTMENT OF ELECTRICAL AND
ELECTRONICS ENGINEERING

AND THE INSTITUTE OF ENGINEERING AND SCIENCES
OF BILKENT UNIVERSITY

IN PARTIAL FULFILLMENT OF THE REQUIREMENTS
FOR THE DEGREE OF
MASTER OF SCIENCE

By

Lütfiye Durak

October 1998

TK

7872

-07

-D87

1998

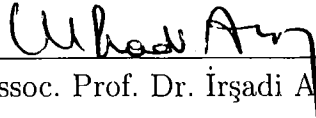
B 043647

I certify that I have read this thesis and that in my opinion it is fully adequate,
in scope and in quality, as a thesis for the degree of Master of Science.



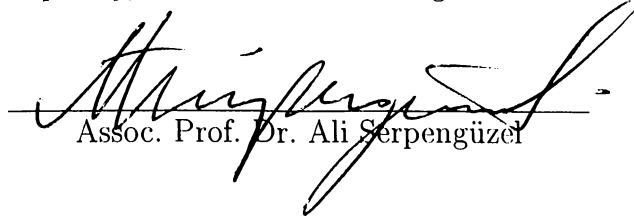
Assoc. Prof. Dr. Orhan Aytür (Supervisor)

I certify that I have read this thesis and that in my opinion it is fully adequate,
in scope and in quality, as a thesis for the degree of Master of Science.



Assoc. Prof. Dr. İrşadi Aksun

I certify that I have read this thesis and that in my opinion it is fully adequate,
in scope and in quality, as a thesis for the degree of Master of Science.



Assoc. Prof. Dr. Ali Serpengüzel

Approved for the Institute of Engineering and Sciences:



Prof. Dr. Mehmet Baray
Director of Institute of Engineering and Sciences

ABSTRACT

NANOSECOND OPTICAL PARAMETRIC OSCILLATORS GENERATING EYE-SAFE RADIATION

Lütfiye Durak

M.S. in Electrical and Electronics Engineering

Supervisor: Assoc. Prof. Dr. Orhan Aytür

October 1998

In this thesis, construction and characterization of nanosecond optical parametric oscillators (OPO's) generating eye-safe radiation are presented. These OPO's convert the output of an Nd:YAG laser at $1.06 \mu\text{m}$ wavelength to $1.57 \mu\text{m}$ wavelength which is in the eye-safe band of the spectrum. A potassium titanyl phosphate (KTP) crystal is employed in these OPO's. In the experiments, output signal energies, pulse durations, spectral characteristics, and divergence angles of the OPO outputs have been measured. We have obtained 35% conversion efficiency by using pump pulses having 15 mJ energy and 7 ns pulse duration. These low energy OPO's can be used in range finders. We have also constructed OPO's that are pumped by 100 mJ pulses of 15 ns pulse duration, and 38% conversion efficiency was achieved. These high energy OPO's can be used in target designators. The divergence angles of the low energy and the high energy OPO's have been measured as 4 mrad and 3 mrad, respectively. A numerical model which takes into account the temporal and spatial beam profiles, diffraction, and absorptions in the crystal has been constructed. The model is in qualitative agreement with the experimental results.

Keywords: optical parametric oscillation, nonlinear crystals, KTP, nanosecond lasers, Nd:YAG.

ÖZET

GÖZE ZARARSIZ IŞIN ÜRETEEN NANOSANIYE OPTİK PARAMETRİK OSİLATÖRLER

Lütfiye Durak

Elektrik ve Elektronik Mühendisliği Bölümü Yüksek Lisans

Tez Yöneticisi: Doç. Dr. Orhan Aytür

Ekim 1998

Bu tezde göze zararsız ışın üreten nanosaniye optik parametrik osilatörlerin (OPO'lar) oluşturulması ve değerlendirilmesi sunulmaktadır. Bu OPO'lar $1.06 \mu\text{m}$ dalgaboyu olan Nd:YAG laser çıkışı spektrumunda göze zararsız aralıkta yer alan $1.57 \mu\text{m}$ 'ye dönüştürmektedir. Bu OPO'larda potasyum titanil fosfat (KTP) kristali kullanılmıştır. Deneylede çıkış sinyali enerjileri, darbe uzunlukları, spektrum ve OPO çıkışı ayrılma açıları ölçülmüştür. OPO'lar 15 mJ enerjisi ve 7 ns darbe uzunluğu olan darbelerle pompalandığında, %35 dönüşüm verimi elde edilmiştir. Bu düşük enerjili OPO'lar mesafe ölçüm uygulamalarında kullanılabilir. Ayrıca, 100 mJ enerjili, 15 ns uzunluğu olan darbelerle pompalanmış OPO'lar kurulmuş ve %38 dönüşüm verimi elde edilmiştir. Bu yüksek enerjili OPO'lar ise hedef işaretleme uygulamalarında kullanılabilir. Ayrılma açıları düşük enerjili OPO'larda 4 mrad, yüksek enerjili OPO'larda 3 mrad olarak ölçülmüştür. Aynı zamanda, zamansal ve uzaysal ışın profillerini, kırınımı ve kristaldeki emilimi hesaba katan bir model oluşturulmuştur. Bu model, deneysel sonuçlarla uyum göstermektedir.

Anahtar kelimeler: optik parametrik osilasyon, doğrusal olmayan kristaller, KTP, nanosaniye lazerler, Nd:YAG.

ACKNOWLEDGMENTS

I would like to express my sincere gratitude to Dr. Orhan Aytür for his supervision, guidance, suggestions, and encouragement throughout the development of this thesis. I would like to thank the members of my committee, Dr. İřşadi Aksun and Dr. Ali Serpengüzel, for their valuable comments on the thesis.

I would also like to extend my thanks to ASELSAN for their support of this work, and to Dr. řefik Süzer for his help in taking some measurements in the laboratories of the Chemistry Department. I am grateful to Mürüvet Parlakay, İsmail Kır, Ersin Başar, Ergün Hırlakođlu for all their help.

I would like to thank Tolga Kartalođlu for his help in the optics laboratory besides his friendship. I am indebted to Güçlü Köprülü not only for his help during the development of this thesis, but also for his support and friendship.

I am grateful to my friends Yamaç Dikmelik, Gülbin Akgün, Deniz Bařkent, Meliha Aksoy, Sevgi Babacan, Birsal Ayrulu, Bahar Deler, Özer Akdemir and Deniz Gürkan for their friendship, encouragement and support whenever I needed.

Special thanks go to Tolga Ekmekçi for his lasting friendship, patience, and all his support on both academic and personal issues. I am grateful to Ayten Türkcan for all her help, too. I feel extremely fortunate to have known her. I would also like to thank Sevgi Recberođlu. I greatly appreciate her friendship.

I am deeply indebted to Nedret Öztan for her patience, understanding, encouragement, and especially her trust.

I would also like to thank Gülçin, Sema and Yasemin for the love and support they have provided me.

Finally, I would like to thank my parents, Sevim and Tarık Durak for their endless love, trust, support and encouragement throughout my life.

Contents

1	Introduction	1
2	Theory of Optical Parametric Oscillation	4
2.1	Nonlinear Materials	4
2.2	The Driven Wave Equation	5
2.3	Phase Matching	7
2.4	Optical Parametric Amplification	8
2.5	Optical Parametric Oscillation	10
3	Historical Review of Nanosecond OPO Experiments	14
3.1	Nanosecond OPO's in Visible and Near-IR	15
3.1.1	LiNbO ₃ OPO's	15
3.1.2	KNbO ₃ OPO's	16
3.1.3	KTP OPO's	17
3.2	Nanosecond OPO's in Near-UV and Visible	19
3.2.1	Urea OPO's	19
3.2.2	BBO OPO's	19
3.2.3	LBO OPO's	21
3.3	Nanosecond OPO's in Mid-IR	22
4	OPO Experiments	24
4.1	Experimental Setup	24
4.1.1	Pump Laser	24
4.1.2	Crystal	25
4.1.3	Cavity Configurations	26
4.1.4	Characterization	28
4.2	Experimental Results	29
4.2.1	Summary of the Results	29

4.2.2	OPO's Pumped up to 20-28 mJ	32
4.2.3	OPO's Pumped up to 15-20 mJ	42
4.2.4	OPO's Pumped up to 100 mJ	51
5	Simulations of OPO Experiments	58
5.1	Model	59
5.2	Analysis of the Coupled Mode Equations	62
5.3	Simulation Results	65
5.3.1	Simulations of the Low Energy OPO's	65
5.3.2	Simulations of the High Energy OPO's	70
5.4	Discussions	71
6	Conclusions	72

List of Tables

2.1	Phase matching types for possible polarizations of the interacting fields.	8
4.1	Sellmeier coefficients of hydrothermally grown KTP crystals	26
4.2	The computed refractive indices that pump, signal and idler experience in NCPM type-II interaction.	26
4.3	Threshold energies of the single-pass and double-pass OPO's with different output couplers.	33
4.4	Maximum conversion efficiency and maximum pump depletion data of the single-pass OPO's.	34
4.5	The maximum conversion efficiency data of the double-pass OPO's	36
4.6	Pulse durations of both single-pass and double-pass OPO's with different output couplers.	39
4.7	Signal divergence data of various double-pass OPO cavities.	41
4.8	Threshold energies of the single-pass and double-pass OPO's with different output couplers.	43
4.9	Maximum conversion efficiency and maximum pump depletion data of the single-pass OPO's.	44
4.10	Maximum conversion efficiency data of the double-pass OPO's. . .	46
4.11	Pulse durations of both single-pass and double-pass OPO's with different output couplers.	49
4.12	Signal divergence data for various double-pass OPO cavities. . . .	51
4.13	Threshold energies of the single-pass OPO's with different output couplers.	52
4.14	Maximum conversion efficiency and maximum pump depletion data of the single-pass OPO's.	53
5.1	Values of the physical parameters used in the model.	61

List of Figures

2.1	Simple schematic of optical parametric amplification process. . . .	8
2.2	Evolution of photon flux densities in an optical parametric amplification process.	10
2.3	A simple OPO schematic.	11
2.4	Photon conversion efficiency vs. pump intensity values that are normalized with respect to the threshold pump intensity.	12
4.1	Single-pass OPO configuration.	27
4.2	Double-pass OPO configuration.	27
4.3	Signal energy vs. pump energy and conversion efficiency vs. pump energy plots of the low energy and high energy experiments.	30
4.4	Oscilloscope traces of the signal of (a) the low energy OPO and (b) the high energy OPO.	31
4.5	Spectrum of the signal of (a) the low energy OPO and (b) the high energy OPO.	31
4.6	The signal profile at 30 cm away from (a) the low energy OPO and (b) the high energy OPO.	31
4.7	Telescope constructed for the first OPO experiment set with focal length values of 127.1 mm and -50.9 mm at 1064 nm.	32
4.8	Pump profile on the KTP crystal.	32
4.9	Signal energy vs. pump energy plots of the single-pass OPO's. . .	34
4.10	Conversion efficiency vs. pump energy plots of the single-pass OPO's.	35
4.11	Pump depletion vs. pump energy plots of the single-pass OPO's. .	35
4.12	Signal energy vs. pump energy plots of the double-pass OPO's. . .	36
4.13	Conversion efficiency vs. pump energy plots of the double-pass OPO's.	37
4.14	Signal energy and conversion efficiency vs. pump energy plots of the double-pass OPO with $R = 70\%$ output coupler.	37

4.15	Conversion efficiency vs. pump energy plots with different cavity lengths.	38
4.16	Oscilloscope traces of the pump, the depleted pump, and the signal of a single-pass OPO.	39
4.17	Oscilloscope trace of the signal of the double-pass OPO with $R = 70\%$ output coupler	39
4.18	Spectrum of the signal.	40
4.19	Signal profiles of double-pass OPO's.	41
4.20	Pump profile on the KTP crystal.	42
4.21	Signal energy vs. pump energy plots of the single-pass OPO's. . .	44
4.22	Conversion efficiency vs. pump energy plots of the single-pass OPO's.	45
4.23	Pump depletion vs. pump energy plots of the single-pass OPO's. .	45
4.24	Signal energy vs. pump energy plots of the double-pass OPO's. . .	46
4.25	Conversion efficiency vs. pump energy plots of the double-pass OPO's.	47
4.26	Signal energy and conversion efficiency vs. pump energy plots of the double-pass OPO with $R = 70\%$ output coupler.	47
4.27	Conversion efficiency vs. pump energy plots with different cavity lengths.	48
4.28	Oscilloscope traces of the pump, the depleted pump, and the signal of a single-pass OPO.	48
4.29	Oscilloscope trace of the signal of the double-pass OPO with $R = 70\%$ output coupler.	49
4.30	Signal profiles of the double-pass OPO's.	50
4.31	Pump profile on the KTP crystal.	51
4.32	Signal energy vs. pump energy plots of the single-pass OPO's.	53
4.33	Conversion efficiency vs. pump energy plots of the single-pass OPO's.	53
4.34	Pump depletion vs. pump energy plots of the single-pass OPO's. .	53
4.35	Pump energy vs. signal energy and conversion efficiency plots.	54
4.36	Signal energy and conversion efficiency vs. pump energy plots with $R = 70\%$ output coupler.	54
4.37	Oscilloscope traces of the pump and the signal of the double-pass OPO.	55
4.38	Spectrum of the signal.	55
4.39	Signal profiles of the double-pass OPO's.	56

5.1	A simple sketch of the discretization of a pump pulse.	59
5.2	Optical parametric oscillation in a single-pass OPO cavity.	60
5.3	Optical parametric oscillation in a double-pass OPO cavity.	61
5.4	Signal energy vs. pump energy data of the single-pass OPO with $R = 80\%$ output coupler.	66
5.5	Simulation and experimental results of the conversion efficiency and pump depletion vs. pump energy data of the single-pass OPO with $R = 90\%$ output coupler.	66
5.6	Simulation and experimental results of the signal energy vs. pump energy data of the double-pass OPO with $R = 80\%$ output coupler.	67
5.7	Simulation and experimental results of the conversion efficiency vs. pump energy data of the double-pass OPO with $R = 80\%$ output coupler.	67
5.8	Simulations and experimental measurements of the time traces of the pump, the depleted pump, and the signal of a single-pass OPO.	68
5.9	Conversion efficiency plots with different cavity lengths.	69
5.10	Simulation and experimental results of the conversion efficiency vs. pump energy data of the single-pass OPO with $R = 70\%$ output coupler.	69
5.11	Simulation and experimental results of the signal energy and con- version efficiency v.s. pump energy data of the double-pass OPO with $R = 60\%$ output coupler.	70
5.12	Simulations and experimental measurements of the time traces of the signal pulse of the double-pass OPO.	70

Chapter 1

Introduction

Optical parametric oscillators (OPO's) are optical devices that convert the wavelength of lasers to different wavelengths where laser sources are unavailable. OPO's are constructed by inserting a nonlinear crystal into an optical cavity which provides optical feedback.

Frequency conversion of lasers can be achieved by using nonlinear optical materials. In nonlinear materials, the polarization density has a nonlinear dependence on the electric field which can be expressed in a power series form. When the quadratic nonlinear dependence is dominant, three fields at different optical frequencies interact by exchanging their energies.

Various frequency mixing processes can be achieved by nonlinear interactions. Second order nonlinear interactions lead three wave mixing, and they are the most frequently used ones. These interactions are sum frequency generation (SFG), second harmonic generation (SHG), difference frequency generation (DFG), and optical parametric amplification. In SFG, two beams at different frequencies are used to generate the sum frequency of these beams. SHG is a special case of SFG. With SHG, the output frequency of a laser is doubled. In DFG process, difference frequency of two input beams is obtained. At the same time, the input beam at the lower frequency is amplified by the process of DFG. Therefore, DFG process is also used for amplification which is called optical parametric amplification. In optical parametric amplification, the two input optical fields are a strong field at a higher frequency (pump), and a weak field at a lower frequency (signal). Through the process, lower frequency field is amplified, and a third field at the difference frequency (idler) is also generated.

An OPO is constructed by inserting an optical parametric amplifier (OPA)

in an optical cavity. Unlike OPA's, OPO's require only one input beam: the pump. The oscillation starts by the spontaneous decay of the pump photons to signal and idler photons, and the interaction evolves efficiently if the momentum conservation (phase matching) condition is satisfied. Therefore, frequency tuning is possible in OPO's. The frequency tuning is achieved either by varying the direction of propagation of the fields in the nonlinear crystal (angular tuning), or by changing the temperature which results a change in the refractive indices of the crystal (temperature tuning), or by using a tunable pump source. The continuous tunability of OPO's is an advantage over lasers. Lasers usually generate light at specific wavelengths, because laser radiation is obtained by stimulated emission between fixed energy levels of a gain medium. There are some exceptional cases where a limited tunability is possible such as dye lasers or Ti:sapphire lasers which have broad energy bands. However, they have much less tuning range than what an OPO can provide.

The temporal profiles of the OPO outputs depend on the temporal nature of the pump lasers. There are continuous wave (cw) OPO's or pulsed OPO's with pulse durations on the order of nanoseconds, picoseconds or femtoseconds. In cw and nanosecond OPO's, the signal makes many round trips in the cavity as the pump passes through the cavity. In nanosecond OPO's, in order to increase the number of round trips that the signal makes during the pump pulse duration, it is advantageous to choose the cavity length as small as possible .

The first OPO, constructed in 1965 [1], was a nanosecond OPO employing a LiNbO₃ crystal. As new crystals and pump lasers appeared on the scene, many other nanosecond OPO experiments have been reported. These OPO's operate at spectral ranges from near ultraviolet (UV) to middle infrared (IR).

In the optical spectrum, the band of 1.54–1.60 μm is accepted as eye-safe. According to the eye-safety criterion of the American National Standard Institute (ANSI), “at 1.54 μm a single exposure of 1 J/cm² is 400,000 times more eye-safe than a corresponding exposure at 1.06 μm ” [2]. Wavelengths in the eye-safe region are mostly absorbed in the aqueous humor portion of the eye which is filled by the ocular fluid next to the cornea. Therefore absorptions on the retina and cornea surfaces are much less than the absorption in aqueous humor, and such a volume absorption is much less harmful than the surface absorptions [3].

In this thesis, nanosecond KTP OPO's generating eye-safe radiation were designed and demonstrated. These OPO's convert the output of an Nd:YAG

laser at 1064 nm wavelength to 1571 nm wavelength which is in the eye-safe band of the spectrum. Eye-safe lasers are preferred for some military applications such as range finding, target designation, and laser radar. The OPO's were constructed to operate either at low energy levels (~ 15 mJ) for range finding applications or at high energy levels (~ 100 mJ) for target designation applications.

Two different types of OPO cavities were constructed. The pump beam is either passed through the KTP crystal once (single-pass OPO), or the depleted pump is reflected back to the crystal providing a second pass of the pump for each round trip (double-pass OPO). Each OPO is characterized by measuring output signal energies, temporal profiles, spectrum, and divergence of the signal.

The experiments were also modeled numerically. In the model, time is discretized by cavity round trip times for each pump pulse. At each time point, the interaction in the nonlinear crystal is handled by finite difference methods. The model takes into account the temporal and spatial beam profiles, diffraction, and absorption in the crystal.

The thesis is structured as follows: Theoretical background information for optical parametric oscillation is provided in Chapter 2. Chapter 3 presents a historical overview of nanosecond OPO experiments from their invention in 1965 up to the present. The setups and the results of the experiments are presented in Chapter 4. Next, the numerical modeling of the OPO's in comparison with the measured results are discussed in Chapter 5. Finally, the conclusions with future directions are given in Chapter 6.

Chapter 2

Theory of Optical Parametric Oscillation

This chapter presents the theory of optical parametric oscillation. The chapter starts with the interaction of light beams with different frequencies in a second order nonlinear material. The evolution of the fields in such a medium is described by using classical electromagnetic theory. Next, the phase matching condition which provides efficient OPO operation is stated. Finally, after explaining optical parametric amplification process, the optical parametric oscillation is discussed.

2.1 Nonlinear Materials

In a nonlinear material, the response of the medium to the applied optical field depends on the field nonlinearly. The relationship between the electric field (\mathbf{E}) and the polarization density (\mathbf{P}) can be expressed in a power series form as

$$\mathbf{P} = \epsilon_0[\chi^{(1)}\mathbf{E} + \mathbf{E} \cdot \chi^{(2)} \cdot \mathbf{E} + \mathbf{E} \cdot (\mathbf{E} \cdot \chi^{(3)} \cdot \mathbf{E}) + \dots] \quad (2.1)$$

$$= \mathbf{P}^{(1)} + \mathbf{P}^{(2)} + \mathbf{P}^{(3)} + \dots \quad (2.2)$$

where ϵ_0 is the permittivity of the free space, $\chi^{(1)}$ is the linear susceptibility tensor, and $\chi^{(2)}$ is the second order nonlinear susceptibility tensor. The higher order nonlinear susceptibilities ($\chi^{(n)}$, $n \geq 3$) are usually negligible compared to the second order term unless $\chi^{(2)}$ is zero. $\chi^{(2)}$ vanishes in centrosymmetric materials which have inversion symmetry, and when this is the case, the third order nonlinearity is dominant.

2.2 The Driven Wave Equation

The evolution of the fields in a second order nonlinear medium are described by the driven wave equation. The source-free Maxwell's equations

$$\nabla \times \mathbf{E} = -\mu_0 \frac{\partial \mathbf{H}}{\partial t} \quad (2.3)$$

$$\nabla \times \mathbf{H} = \frac{\partial \mathbf{D}}{\partial t} \quad (2.4)$$

$$\nabla \cdot \mathbf{D} = 0 \quad (2.5)$$

$$\nabla \cdot \mathbf{B} = 0 \quad (2.6)$$

and the constitutive relations

$$\mathbf{D} = \epsilon_0 \mathbf{E} + \mathbf{P} \quad (2.7)$$

$$\mathbf{B} = \mu_0 \mathbf{H} \quad (2.8)$$

describing the effects of electromagnetic fields in a nonmagnetic medium are used to form the driven wave equation [4]

$$\nabla^2 \mathbf{E} - \frac{n^2}{c^2} \frac{\partial^2}{\partial t^2} \mathbf{E} = \mu_0 \frac{\partial^2}{\partial t^2} \mathbf{P}^{(2)} \quad (2.9)$$

where n is the refractive index of the medium. In the derivation of Equation (2.9), the first approximation is [4]

$$\nabla \cdot \mathbf{E} \simeq 0. \quad (2.10)$$

If the fields are plane waves, then $\nabla \cdot \mathbf{E}$ is exactly zero [5]. If the fields are not plane waves, but have slowly varying amplitudes, this is a valid approximation [4]. Moreover, as a second approximation

$$n^2 \simeq 1 + \chi^{(1)} \quad (2.11)$$

is used. For isotropic materials, n^2 is exactly equal to $1 + \chi^{(1)}$. For anisotropic materials, if \mathbf{D} and \mathbf{E} vectors are parallel then this is a valid approximation. However, if the direction of propagation is not along one of the principal axes of the anisotropic crystal, there is an angle between \mathbf{D} and \mathbf{E} vectors which is called the walkoff effect [4]. This approximation fails unless walkoff is small.

In a second order nonlinear medium, in the most general situation, three optical fields satisfying the frequency relation of

$$\omega_3 = \omega_1 + \omega_2 \quad (2.12)$$

interact. One can choose three monochromatic plane waves propagating along the z -axis such as

$$\mathbf{E}_i(\mathbf{r}, t) = \text{Re}[\mathbf{E}_i(z)e^{j(\omega_i t - k_i z)}] \quad i = 1, 2, 3 \quad (2.13)$$

with nonlinear polarization densities

$$\mathbf{P}_i^{(2)}(\mathbf{r}, t) = \text{Re}[\mathbf{P}_i^{(2)}(z)e^{j\omega_i t}] \quad i = 1, 2, 3. \quad (2.14)$$

By inserting the expressions of $\mathbf{E}_i(\mathbf{r}, t)$ and $\mathbf{P}_i^{(2)}(\mathbf{r}, t)$ into Equation (2.9),

$$\nabla^2(\mathbf{E}_i(z)e^{-jk_i z}) + \frac{n_i^2 \omega_i^2}{c^2} \mathbf{E}_i(z)e^{-jk_i z} = -\mu_0 \omega_i^2 \mathbf{P}_i^{(2)}(z). \quad (2.15)$$

is obtained. If we substitute

$$\mathbf{E}_i(z) = E_i(z)\mathbf{a}_i \quad (2.16)$$

and assume that the change of the field amplitudes in one wavelength distance is much smaller than the field amplitude itself (slowly varying amplitude approximation) as

$$\left| \frac{d^2}{dz^2} E_i \right| \ll \left| k_i \frac{d}{dz} E_i \right| \quad i = 1, 2, 3 \quad (2.17)$$

which is valid for waves at optical frequencies, Equation (2.15) becomes

$$\frac{d}{dz} E_i(z)e^{-jk_i z} = -j \frac{\mu_0 \omega_i^2}{2k_i} \mathbf{a}_i \cdot \mathbf{P}_i^{(2)}(z). \quad (2.18)$$

For the field at frequency ω_1 , $\mathbf{a}_1 \cdot \mathbf{P}_1^{(2)}(z)$ is

$$\begin{aligned} \mathbf{a}_1 \cdot \mathbf{P}_1^{(2)}(z) &= \mathbf{a}_1 \cdot \epsilon_0 (\mathbf{E}_3(z)e^{-jk_3 z} \cdot \chi^{(2)} \cdot \mathbf{E}_2^*(z)e^{jk_2 z}) \\ &= \epsilon_0 E_3(z) E_2^*(z) e^{-j(k_3 - k_2)z} (\mathbf{a}_1 \cdot (\mathbf{a}_2 \cdot \chi^{(2)} \cdot \mathbf{a}_3)) \end{aligned} \quad (2.19)$$

where $\mathbf{a}_1 \cdot (\mathbf{a}_2 \cdot \chi^{(2)} \cdot \mathbf{a}_3)$ is the element of the $\chi^{(2)}$ tensor corresponding to this polarization geometry, and usually the following notation

$$d_1 = \frac{1}{2} \mathbf{a}_1 \cdot (\mathbf{a}_2 \cdot \chi^{(2)} \cdot \mathbf{a}_3) \quad (2.20)$$

is used. In a similar way, one can express Equation (2.15) for each field as

$$\frac{d}{dz} E_1(z) = -j \frac{\omega_1 d_1}{n_1 c} E_2^*(z) E_3(z) e^{-j\Delta k z} \quad (2.21)$$

$$\frac{d}{dz} E_2(z) = -j \frac{\omega_2 d_2}{n_2 c} E_1^*(z) E_3(z) e^{-j\Delta k z} \quad (2.22)$$

$$\frac{d}{dz} E_3(z) = -j \frac{\omega_3 d_3}{n_3 c} E_1(z) E_2(z) e^{j\Delta k z} \quad (2.23)$$

where $\Delta k = k_3 - k_1 - k_2$ is the phase-mismatch term. If the nonlinear medium is lossless,

$$d_1 = d_2 = d_3 = d_e \quad (2.24)$$

and d_e is called the effective second order nonlinear coefficient. The equations (2.21)–(2.23) are called coupled mode equations. As seen in the equations, two fields together behave as a source term of the remaining third field.

The type of the nonlinear interaction of these three waves depends on the initial conditions of the fields. For example, DFG is a second order nonlinear process, where two input fields at frequencies ω_1 and ω_3 are combined to form a third field at the difference frequency ($\omega_2 = \omega_3 - \omega_1$).

2.3 Phase Matching

In the coupled mode equations (Equations (2.21)–(2.23)), the phase mismatch factor (Δk) should vanish in order to provide efficient interaction of the three coupled fields [4]. The phase matching condition for collinear beams is

$$\Delta k = k_3 - k_2 - k_1 = 0 \quad (2.25)$$

and if it holds, the phase velocities of both the fields and the polarization densities at the same frequency remain equal during the interaction. Therefore, in second order interactions besides the energy conservation condition

$$\omega_3 = \omega_1 + \omega_2 \quad (2.26)$$

Equation (2.25) stating

$$n_3\omega_3 = n_1\omega_1 + n_2\omega_2 \quad (2.27)$$

should also be satisfied.

However refractive indices of materials usually increase as the frequency of the wave increases (normal dispersion). In other words, for fields at frequencies of $\omega_3 > \omega_2 \geq \omega_1$, the refractive indices are $n_3 > n_2 \geq n_1$. In dispersive materials, it is impossible to satisfy the two conservation conditions simultaneously.

In order to achieve phase-matching, one method is to use the birefringence of anisotropic crystals. In anisotropic crystals, for each propagation direction, there are two eigenpolarizations of a field which experience two different eigenrefractive

Type	ω_1	ω_2	ω_3
I	slow	slow	fast
II	fast	slow	fast
III	slow	fast	fast

Table 2.1: Phase matching types for possible polarizations of the interacting fields.

indices. For the phase matching condition to be satisfied, the field at the highest frequency should be polarized in the direction of the lower refractive index (fast axis), and the lower frequency fields should either be polarized both in the direction of the higher refractive index (slow axis) or be polarized perpendicular to each other (one at the fast axis, other at the slow axis). The phase matching schemes that are formed for each possibility of the field polarizations are labeled as type I, type II and type III, and are presented in Table 2.1.

If the phase matching condition is satisfied when the direction of propagation is along one of the optic axes of the crystal, this condition is called noncritical phase matching [6]. In this case there is no walkoff.

Also, in order to achieve phase matching, the interacting waves do not have to be collinear. If the beams propagate noncollinearly, the phase matching condition (noncollinear phase matching) is expressed as

$$\mathbf{k}_3 - \mathbf{k}_1 - \mathbf{k}_2 = 0. \quad (2.28)$$

2.4 Optical Parametric Amplification

In optical parametric amplification process, a strong pump field at ω_3 is used to amplify a weak signal field at ω_1 . An idler beam at $\omega_2 = \omega_3 - \omega_1$ is also generated throughout the interaction. Figure 2.1 presents a simple schematic of the optical parametric amplification process.

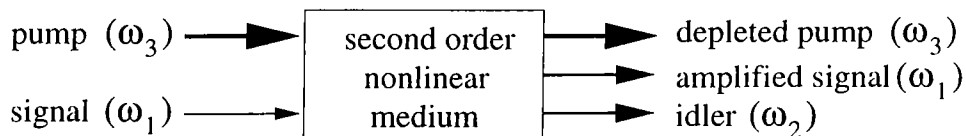


Figure 2.1: Simple schematic of optical parametric amplification process.

The evolution of the fields in an OPA can be calculated by solving the coupled

mode equations (Equations (2.21)–(2.23)). If the phase matching condition is satisfied, the coupled mode equations become

$$\frac{d}{dz}E_1 = -j\frac{d_e\omega_1}{n_1c}E_3E_2^* \quad (2.29)$$

$$\frac{d}{dz}E_2 = -j\frac{d_e\omega_2}{n_2c}E_3E_1^* \quad (2.30)$$

$$\frac{d}{dz}E_3 = -j\frac{d_e\omega_3}{n_3c}E_1E_2. \quad (2.31)$$

The general solutions of the fields are in terms of Jacobi elliptic functions [7].

We can normalize the complex field amplitudes as

$$E_i = \sqrt{\frac{2\hbar\omega_i}{n_i c \epsilon_0}} a_i e^{-j\phi_i} \quad i = 1, 2, 3 \quad (2.32)$$

where a_i^2 's are the photon flux densities.

In the optical parametric amplification process, when a pump photon is used to form a signal photon, an idler photon is generated. So the following quantities are conserved:

$$c_1 = a_1^2(z) + a_3^2(z) \quad (2.33)$$

$$c_2 = a_2^2(z) + a_3^2(z). \quad (2.34)$$

These conservation relations (Equations (2.21)–(2.23)) are called as Manley-Rowe relations. By using the constants of the Manley-Rowe relations, the solutions for the normalized field amplitudes are

$$a_1(z) = \sqrt{c_1} \operatorname{dn}(Z_a|m_a) \quad (2.35)$$

$$a_2(z) = \sqrt{c_2} \operatorname{cn}(Z_a|m_a) \quad (2.36)$$

$$a_3(z) = \sqrt{c_2} \operatorname{sn}(Z_a|m_a) \quad (2.37)$$

where dn , cn , and sn are the Jacobi elliptic functions, $m_a = c_1/c_2$, and Z_a is

$$Z_a = K(m_a) - d_e \sqrt{\frac{2\hbar\omega_1\omega_2\omega_3}{c^3\epsilon_0 n_1 n_2 n_3}} \sqrt{c_2} z \quad (2.38)$$

where $K(m_a)$ is the complete elliptic integral of the first kind [8].

Figure 2.2 presents the evolution of photon flux densities in an OPA. (The parameters of the OPA are arbitrarily chosen as: $d_e = 3.6 \times 10^{-12}$, a signal beam at 1571 nm, and a pump beam at 1064 nm.) The photon flux densities are

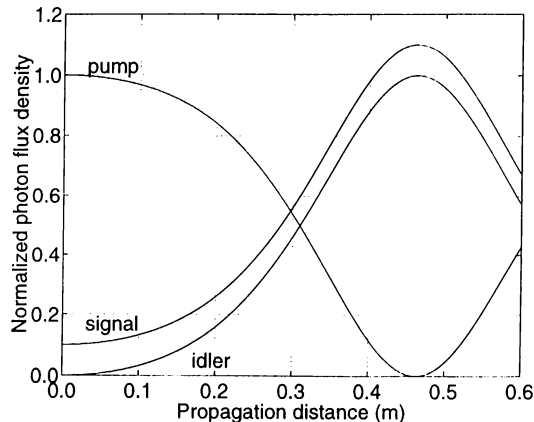


Figure 2.2: Evolution of photon flux densities in an optical parametric amplification process. The photon flux densities are normalized by the pump photon flux density.

normalized by the pump photon flux density. The initial signal is chosen as 10% of the initial pump. The signal gets amplified until the pump is fully depleted. Then the interaction gets reversed, where signal and idler photons combine to form pump photons. This is called backconversion.

In OPA's, parametric gain is defined as

$$G = \frac{a_1^2(l)}{a_1^2(0)} \quad (2.39)$$

where l is the interaction length.

Small-signal gain is the gain that the signal experiences when the depletion of the pump is negligible. With constant input pump assumption, the coupled mode equations can be simplified, and they lead to an approximate solution for the small-signal gain as

$$G_0 = \cosh^2 \left[d_e \sqrt{\frac{2\hbar\omega_1\omega_2\omega_3}{c^3\epsilon_0 n_1 n_2 n_3}} a_3(0)z \right]. \quad (2.40)$$

2.5 Optical Parametric Oscillation

An OPO is constructed by inserting an OPA into an optical cavity which provides feedback for the signal. OPO's require only one input beam: the pump. The initial signal field is obtained by the spontaneous decay of the pump photons into the signal and idler photons, a process known as parametric fluorescence. Initially, signal experiences small signal gain. When this unsaturated gain compensates for the total loss in the cavity, oscillation starts. In an OPO, signal is coupled

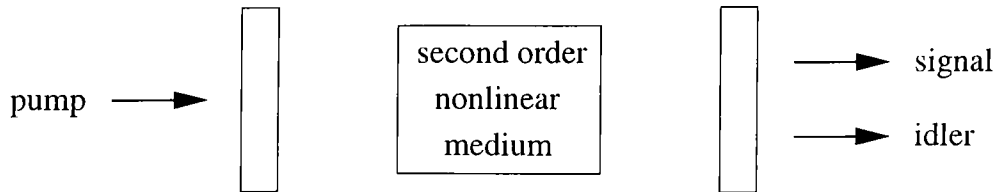


Figure 2.3: A simple OPO schematic. The nonlinear crystal is inserted in a cavity which provides feedback to the parametric amplification process.

out of the cavity by a partially transmitting mirror at the signal wavelength. As the signal intensity in the cavity increases, gain saturates. OPO's operate at steady state as long as this saturated gain compensates for the total loss exactly. Figure 2.3 presents a simple OPO schematic.

There are two types of OPO resonators depending on the resonating fields in the cavity: singly-resonant OPO's (SROPO's) and doubly-resonant OPO's (DROPO's). In SROPO's, only the signal field is resonated, and the idler is removed away with each round trip of the signal. In DROPO's both the signal and the idler are resonated. DROPO's have lower pump threshold intensities when compared to SROPO's, however SROPO's are much more stable than DROPO's [6].

In an OPO, taking the signal out of the cavity is a useful loss. Useless losses are all other losses including reflection losses, absorption, scattering and transmission losses. If the useless losses are denoted as L , then let

$$R_L = 1 - L. \quad (2.41)$$

So, when there is no loss $R_L = 1$, and R is defined as

$$R = R_L R_{OC} \quad (2.42)$$

where R_{OC} is the reflectivity of the output coupler. The steady state oscillation condition is

$$G = \frac{1}{R}. \quad (2.43)$$

where G is the saturated signal gain.

In a cw OPO, by using the small signal gain expression (Equation (2.40)), threshold intensity (I_{TH}) is expressed as

$$I_{TH} = \frac{\epsilon_0 c^3 n_1 n_2 n_3}{2d_e^2 \omega_1 \omega_2 l^2} \left[\frac{1}{\cosh^2(\sqrt{1/1-R})} \right]. \quad (2.44)$$

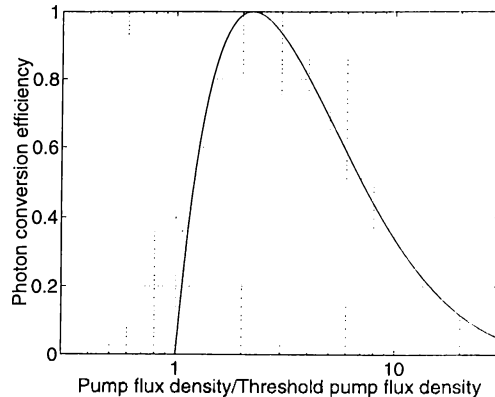


Figure 2.4: Photon conversion efficiency vs. pump intensity values that are normalized with respect to the threshold pump intensity.

As the loss in the cavity increases, the threshold intensity increases as well.

An important measure of performance of an OPO is the conversion efficiency. The photon conversion efficiency of OPO's is defined as

$$\eta = (1 - R_{OC}) \frac{a_1^2(l)}{a_3^2(0)}. \quad (2.45)$$

Figure 2.4 presents the photon conversion efficiency vs. pump intensity values of an OPO. The parameters of the OPO are arbitrarily chosen as: A 2 mm long nonlinear crystal with $d_e = 3.6 \times 10^{-12}$, a signal beam at 1571 nm, and a pump beam at 1064 nm. R_{OC} is chosen as 50%, and there are no useless losses. The pump intensity values are normalized with respect to the threshold pump intensity of the OPO. As seen in Figure 2.4, the photon conversion efficiency increases to 100%. At this point, the pump is totally depleted. If we increase the pump intensity further, the efficiency drops because of backconversion. For a specific pump intensity value, a loss value can always be found which maximizes the conversion efficiency value. Therefore, output coupler reflectivity is an important design parameter for OPO's, given the pump intensity.

Power conversion efficiency is the ratio of the output signal power and the input pump power and the relationship between the photon conversion efficiency (η) and the power conversion efficiency is

$$\eta_{\text{power}} = \eta \frac{\omega_1}{\omega_3}. \quad (2.46)$$

We can also investigate the OPO's according to their temporal behavior. In cw and nanosecond OPO's, pump pulse lengths are usually longer than cavity lengths, so signal makes many round trips as the pump passes through the cavity.

In ultrafast OPO's, the pulse lengths are almost always shorter than the cavity lengths, so the OPO cavity length should be adjusted such that each pump pulse meets the resonant signal in the cavity. After several round trips of the signal, OPO reaches a steady state.

These analytical solutions explain the behavior of cw OPO's operating with plane waves. Analytical solutions which take into account the temporal and spatial beam profiles of the fields do not exist. Therefore, such physical effects can be handled by numerical models.

Chapter 3

Historical Review of Nanosecond OPO Experiments

OPO's, as efficient and widely tunable coherent light sources, have attracted the attention of many researchers since their first demonstration in 1965 [1]. This chapter establishes a perspective on the progress of nanosecond OPO's from their invention up to the present. We classify the experiments according to the spectral range they cover, such as near-UV and visible, visible and near-IR, and mid-IR, and for each range we investigate the OPO experiments according to the crystals they employ.

An OPO crystal should satisfy some properties in order to achieve oscillation [9]. First of all, OPO crystals must have high nonlinearity in order to provide sufficient gain. Secondly, the birefringence of the crystals should be adequate for phase matching within their transparency ranges. As the third requirement, the crystals should have high optical damage threshold, since large pump intensities are required for the oscillation to start. They must also have high optical quality and be long enough. Most of the crystals employed in optical parametric processes are LiNbO_3 , LiIO_3 , KNbO_3 , KTiOPO_4 (KTP) and its isomorphs, such as KTA, CTA, RTA, RTP for the visible, and near IR; $\beta\text{-BaB}_2\text{O}_4$ (BBO), LiB_3O_5 (LBO), and urea for the visible, and near UV; chalcopyrites (AgGaS_2 , AgGaSe_2 , ZnGeP_2 , and CdGaAs_2), Tl_3AsSe_3 , and GaSe for the mid-IR [9], [10], [6]. Pump lasers employed in the nanosecond OPO experiments are generally the fundamental, and the harmonics of Nd:YAG lasers, Nd:YLF lasers, Ti:sapphire lasers, and excimer lasers.

There is a vast literature on both experimental and theoretical aspects of

this subject. In this chapter, we emphasized on the experiments conducted after 1980's, but also included the milestone works of 1960's, and 1970's as well.

3.1 Nanosecond OPO's in Visible and Near-IR

3.1.1 LiNbO₃ OPO's

Until 1980's OPO's generally employed LiNbO₃ (lithium niobate) crystals which have damage threshold intensity on the order of 100 MW/cm², and transparency range from 0.8 μm to 3.5 μm [6]. As other crystals appeared, the popularity of LiNbO₃ substantially decreased in the eighties and nineties, except the growing interest in periodically poled LiNbO₃ (PPLN) crystals in late-nineties [11], [12], [13].

The first OPO was a nanosecond doubly resonant OPO, and it was demonstrated by Giordmaine and Miller [1] in 1965. They obtained less than 1% conversion efficiency, with a tuning range from 0.97 μm to 1.15 μm by temperature tuning. Later Bjorkholm [14] performed the first singly resonant OPO experiment with a 0.94 cm long LiNbO₃ crystal in 1968. Bjorkholm reported 22% conversion from pump power to signal power in a doubly resonant configuration and 6% conversion in a singly resonant configuration.

Harris [15] reviewed the studies on OPO's up to 1969 with a detailed theoretical analysis. In those years other than the LiNbO₃ crystal, KDP and Ba₂NaNb₅O₁₅ crystals were used in the OPO experiments.

By the end of 1972, LiNbO₃ crystals up to 5 cm were available [9]. The highest conversion efficiency up to that time was reached by Wallace [16] in 1970. They achieved approximately 67% pump depletion, and 46% conversion to both signal and idler in the spectral range from 0.54 μm to 3.65 μm . Tuning of the OPO was achieved by using different transitions of the pump laser and temperature tuning of the LiNbO₃ crystal.

In another experiment, Herbst *et al.* [17] demonstrated a singly-resonant angle-tuned OPO and obtained 15% conversion efficiency. Pump threshold intensity was approximately 30 MW/cm². The oscillator covered the entire 1.4–4 μm spectral range.

In 1979, Brosnan and Byer [18] described a theoretical model for time dependent OPO threshold pump powers, and also they built Nd:YAG laser pumped SROPO's with LiNbO₃ crystals. They both computed numerically and observed

experimentally OPO threshold intensities by varying the cavity length, crystal length, signal reflectance of the output coupler, pump spot size, and pump pulse width parameters separately. The pump threshold values varied from 0.2 J/cm^2 to 0.5 J/cm^2 . They obtained 18% conversion to signal and idler. Their model was in agreement with the demonstrated results.

In a recent experiment in 1996, an intracavity optical parametric oscillation configuration was implemented. By inserting a LiNbO_3 OPO into a pump laser (a diode pumped Nd:YAG laser) cavity, Lavi *et al.* [19] utilized two advantages. The first advantage is that intensity inside the cavity is always larger than the intensity coupled to the outside. As the second advantage, effective length of the interaction increased due to the many round trips of the pump beam. In the experiment, threshold pump intensity was about 9 MW/cm^2 , and they obtained 1.8% conversion efficiency from diode energy inside the cavity to idler at $3.7 \mu\text{m}$. By angle tuning they obtained outputs from $3.3 \mu\text{m}$ to $4.15 \mu\text{m}$.

3.1.2 KNbO_3 OPO's

KNbO_3 (potassium niobate) crystal is a biaxial crystal which operates in the near-IR region of the spectrum. It has large effective nonlinear coefficient, large transmission range (400–4500 nm) and high damage threshold. KNbO_3 OPO's are usually pumped by the fundamental or the second harmonic of Nd:YAG lasers [20], [21], [22], or Ti:sapphire lasers [23].

In 1982, Kato [20] accomplished parametric oscillation in a Type I noncritically phase matched (NCPM) crystal KNbO_3 which was tunable over 0.88– $1.35 \mu\text{m}$ region by temperature tuning. He obtained 32% conversion from pump power to signal and idler powers and threshold pump intensity was measured as 3.5 MW/cm^2 .

Another type I phase matched KNbO_3 OPO was reported by Urschel *et al.* [21] in 1995. They achieved a tuning range of 1.45 – $2.01 \mu\text{m}$ for signal and 2.27 – $4.0 \mu\text{m}$ for idler. Threshold intensity was 65 MW/cm^2 and when pumped twice the threshold, 14% conversion efficiency was achieved.

Type II phase matched KNbO_3 OPO's were first demonstrated by Bosenberg *et al.* [22] in 1993. These OPO's were operating at $1.87 \mu\text{m}$ signal and $2.47 \mu\text{m}$ idler wavelength with 240 MW/cm^2 threshold intensity. In a similar configuration but a cavity employing a type I phase-matched KNbO_3 crystal at the same signal wavelength, threshold intensity was 145 MW/cm^2 . Since effective nonlinear

coefficient of type II phase matching is less than type I phase matching.

By using a tunable Ti:sapphire laser as the pump source, Rambaldi *et al.* [23] constructed a KNbO₃ OPO, and obtained tuning ranges of 908 nm to 1402 nm for the signal, and 2103 nm to 3803 nm for the idler. Oscillation threshold was 15 MW/cm². Maximum signal output they had obtained was 3 mJ at 70 mJ pump energy where this value is limited by the low damage threshold of the OPO mirror coatings.

3.1.3 KTP OPO's

KTP is a biaxial crystal operating in the near-IR range. KTP crystals are grown by either hydrothermal or flux methods. KTP crystal has many advantages over the other crystals in the same spectral range. The damage threshold of the KTP (~ 1 GW/cm²) crystal is much higher than LiNbO₃ (~ 140 MW/cm²) crystal. It has a broad transparency range (0.35 μ m to 4.3 μ m). However, efficiency of the OPO outputs between 3–4 μ m is lower because of the weak multiphonon absorption at ~ 3.5 μ m [6]. KTP OPO's are usually pumped by the fundamental and the second harmonic of Nd:YAG lasers, Nd:YLF lasers, or Ti:sapphire lasers.

In 1989, Burnham *et al.* [24] demonstrated the first KTP OPO with a 6 mm long flux grown KTP crystal. The OPO was pumped by an Nd:YAG laser. They achieved optical parametric oscillation near degeneracy at 2.12 μ m with a threshold intensity of 40 MW/cm². Soon after, Lin *et al.* [25] reported a tunable KTP OPO (between 1.8–2.4 μ m) pumped by an Nd:YAG laser, and achieved approximately 2.4% conversion efficiency.

Tunable IR generation around 3.2 μ m from a KTP OPO was experimentally demonstrated in 1991. Kato [26] achieved 35% pump depletion and 18% conversion to 1579 nm, and 5% conversion to 3264 nm with a pump threshold intensity of 80 MW/cm².

Between 1991–1993, Marshall *et al.* [27], [28], [29] carried out eye-safe OPO experiments. In these experiments, the OPO's were pumped by Nd:YAG lasers, and flux-grown KTP crystals were used. In the first experiment, Marshall *et al.* [27] reported threshold intensity as approximately 100 MW/cm², and conversion efficiency as 25% to the eye-safe signal at 1.61 μ m with a 15 mm long crystal. Soon after in 1991, Marshall *et al.* [28] obtained 35% conversion efficiency from 1.064 μ m pump to 1.61 μ m signal in a confocal cavity. In 1993, Marshall and Kaz [29] reported 47% conversion efficiency with a 20 mm long flux grown KTP

crystal. The threshold intensity for the oscillation was about 38 MW/cm².

OPO's generating narrow linewidth outputs are necessary in some applications, such as high resolution spectroscopy. For this reason, KTP OPO's with narrow linewidths were constructed either by injection seeding the OPO's [30], or by inserting some etalons [31], gratings [32] to the OPO cavities. In these experiments linewidths less than 500 MHz were obtained.

KTP OPO's pumped by tunable lasers are demonstrated in 1992 by Jani *et al.* [33] where the pump laser was a tunable alexandrite laser (720–800 nm range). Their OPO was doubly-resonant. They obtained 2.25% total conversion efficiency to both signal (1527–1540 nm) and idler (1399–1616 nm). In a consecutive study, with the same pump source, Jani *et al.* [34] achieved the first optical parametric oscillation in KTA crystal. The tuning range for both the idler and the signal was 1400–1700 nm. With a 7 mm KTA crystal, they obtained approximately %0.4 total conversion efficiency.

Another tunable laser pumped KTP OPO was constructed by Zenzie *et al.* [35] in 1994, with a Ti:sapphire laser. By using a NCPM 15 mm long flux grown KTP crystal, they achieved signal and idler outputs in the spectral range of 1030–1280 nm and 2180–3030 nm, respectively. They achieved %45 total conversion efficiency. They also reported degenerate OPO operation with a type I phase matched KNbO₃ crystal, and measured 44% conversion efficiency.

In two studies, Nd:YLF pumped KTP OPO's with low pump threshold energies are reported by Terry *et al.* [36] in 1994, and Tang *et al.* [37] in 1997. Terry *et al.* [36] measured threshold energies less than 0.5 mJ. In their experiment, conversion efficiency was 20%, whereas the pump depletion was 50%. The OPO was employing a flux grown, 20 mm long KTP crystal in a NCPM geometry, where the signal and idler wavelengths were 1.54 μm and 3.28 μm , respectively. They also developed a model for computing the threshold energies which takes into account unequal absorption coefficients of the beams in a nonlinear crystal.

A numerical model of nanosecond OPO's was developed by Smith *et al.* [38] at Sandia National Laboratories, and they obtained experimental results that are in agreement with the model. In the experiments, they constructed an injection seeded ring OPO cavity employing a 10 mm KTP crystal, and pumped the OPO with the second harmonic of an injection seeded Nd:YAG laser. They measured 0.7 J/cm² threshold energy fluence, and achieved 29% conversion to signal at 780 nm. In a later study in 1997, the same group of researchers experimentally

demonstrated and numerically modeled parametric amplification and oscillation processes with walkoff compensating crystals in a similar manner (Armstrong *et al.* [39]).

3.2 Nanosecond OPO's in Near-UV and Visible

3.2.1 Urea OPO's

The studies on urea OPO's began in 1984 [40] and continued until early nineties. Unlike the OPO's built up to that time, urea OPO's exhibit tunability from blue-green up to near-IR. However, urea crystal has significant disadvantages. One of the disadvantages is its low damage threshold (~ 180 MW/cm²) [10]. Moreover, in order to obtain a usable sized crystal, a long time period (on the order of one year) is required. Urea OPO's are generally pumped by the third harmonic of Nd:YAG lasers at 355 nm [40], [41], [42], [43] or excimer lasers at 308 nm [44], [45], [46].

In the first urea OPO experiment, Donaldson *et al.* [40] achieved 6% conversion efficiency from pump at 355 nm to idler at 1.22 μ m with a 13 mm long crystal. Soon after, with the same OPO configuration Rosker *et al.* [41] demonstrated 8.5% conversion to signal between 498–640 nm with a 23 mm crystal.

Excimer laser pumped urea OPO experiments were carried out in the J. F. Allen Physics Research Laboratories between 1988 and 1990. In the first experiment, Ebrahimzadeh *et al.* [44] reported 2.5% conversion efficiency with an 8 mm long crystal. Later by employing a 15 mm long urea crystal and double-passing the pump beam through the OPO cavity, they reached 37% conversion efficiency from pump to both idler at 670 nm and signal at 570 nm [45]. Oscillation threshold intensities were about 16–20 MW/cm². In the third experiment, Henderson *et al.* [46] obtained OPO outputs from 537 nm to 720 nm by angle tuning. In this case the urea crystal was 25 mm long, and the oscillation threshold intensity was 2.3 MW/cm². They obtained approximately 26% efficiency from pump to signal at 570 nm.

3.2.2 BBO OPO's

BBO (β -barium borate) crystal was introduced in 1986. BBO crystals have significant superiority over the urea crystals operating in similar spectral ranges. They have higher damage threshold (~ 10 GW/cm² for BBO vs. ~ 180 MW/cm²

for urea) and larger transparency range (0.2–3.3 μm for BBO vs. 230–1020 nm for urea). They are mechanically robust, chemically stable, and can be grown easier than urea crystals [10]. However, BBO crystals are hygroscopic. BBO OPO's are generally pumped by the second, third and fourth harmonics of Nd:YAG lasers or excimer lasers. In optical spectroscopic applications (such as photoacoustic absorption, optical double resonance, and coherent Raman spectroscopy) BBO OPO's are used. [47], [48].

Earlier BBO OPO's suffered from lower efficiencies because of the low damage threshold of OPO mirrors, poorer quality of the crystals, and large walkoff imposed by the phase matching geometries. In the first BBO OPO experiment, Fan *et al.* [49] obtained 10% conversion efficiency in a tuning range of 0.94 μm to 1.22 μm by pumping the OPO with the second harmonic of an Nd:YAG laser. In 1988, Cheng *et al.* [50] reported 9.4% conversion efficiency by pumping their BBO OPO with the third harmonic of an Nd:YAG laser. In another study, Fan *et al.* [51] accomplished 13% conversion to signal at 532 nm, and 11% conversion to idler at 1064 nm.

In three consecutive studies of Bosenberg *et al.*, a novel cavity design for BBO OPO's was presented [52], [53], [54] in 1989, and 1990. They inserted a pair of pump reflecting mirrors at Brewster angle with respect to the cavity axis, just after the OPO cavity mirrors. Therefore, pump transmission condition of the cavity mirrors had been abolished. In the first experiment [52], the pump source was the fourth harmonic of an Nd:YAG laser at 266 nm. By rotating the crystal, the OPO outputs were tuned from 0.33 μm to 1.37 μm . In order to minimize walkoff effects, in the second experiment, Bosenberg *et al.* [53] used two BBO crystals in a proper orientation such that walkoff created by the first crystal is eliminated by the second one. They accomplished 32% total conversion efficiency throughout the 0.42–2.3 μm spectral range. Walkoff compensation provided a remarkable increase in the efficiency when compared to the other designs.

In 1988, Kominc [55] constructed an XeCl excimer laser pumped BBO OPO, and measured 10% conversion efficiency. The tuning range was between 422–477 nm for the signal. Other excimer laser pumped BBO OPO studies were performed by Ebrahimzadeh *et al.* [56] in 1990. They achieved more than 10% conversion efficiency in the 354–2370 nm spectral range. The pump threshold intensities were between 12.5–28 MW/cm² throughout the tuning range.

Highly efficient BBO OPO's are obtained by double-pass OPO cavity configurations [57], [58]. In 1991, Wang *et al.* [57] achieved 41% conversion efficiency in such a configuration. This OPO was tunable over the 415–2411 nm spectral range.

Although noncollinear phase matching of a LiNbO₃ OPO was first demonstrated in 1969, little work was carried out on noncollinear phase matching until 1994. Gloster *et al.* [59], [60] demonstrated nanosecond noncollinearly phase-matched BBO OPO's. They pumped these OPO's by the second or the third harmonic of an Nd:YAG laser, and achieved maximum 31% conversion efficiency. Another noncollinearly phase matched BBO OPO experiment was reported by Lee *et al.* [61] in 1997. Their pump was the second harmonic of an Nd:YAG laser. In a double-pass pump configuration, they achieved 23% conversion efficiency.

In BBO OPO's, effective nonlinear coefficient for type I interactions is larger than type II. So a few type II phase matched BBO OPO experiments were performed [54], [62]. The maximum conversion efficiency obtained in type II OPO's is 25% by Wu *et al.* [62] in 1997.

3.2.3 LBO OPO's

BBO and LBO (lithium triborate) crystals have similar growth techniques. Effective nonlinear coefficient of LBO crystal is less than BBO, and LBO has a smaller tuning range. However, this new crystal offered some advantages over BBO for OPO applications in the UV spectral range. Among these advantages are the higher damage threshold, possibility of noncritical phase matching, smaller walkoff, and outputs with narrower linewidths because of smaller birefringence [6].

The first LBO OPO was reported by Kato in 1990 [63]. By pumping the OPO with the second harmonic of an Nd:YAG laser, he achieved a tuning range of 0.95–1.006 μm and 1.130–1.210 μm in a type II NCPM configuration. The oscillation threshold intensity was approximately 220 MW/cm². He obtained 1% conversion efficiency with a 5 mm long LBO crystal. Soon after in 1991, Wang *et al.* [64] accomplished 22% conversion efficiency to visible output at 502.8 nm with a 16 mm long LBO crystal. The pump was the third harmonic of an Nd:YAG laser.

In J. F. Allen Physics Research Laboratories, a series of nanosecond LBO OPO experiments were performed. In these experiments, pump sources were XeCl excimer lasers [65], [66], [67], fourth harmonic [68] and third harmonic [69], [70]

of Nd:YAG lasers, or second harmonic of Nd:YLF lasers [71]. Two of these experiments employed critically phase matched OPO's [66], [70], while all the remaining experiments employed NCPM OPO's. In the NCPM OPO's conversion efficiencies to signal outputs up to 20% and pump depletions up to 40% were obtained. In critically phase matched LBO OPO's, comparable results to BBO OPO's were reported for threshold energy fluences (~ 0.2 J/cm² for BBO OPO's, ~ 0.3 J/cm² for LBO OPO's) and pump depletions (50% for BBO OPO's, 40% for LBO OPO's). In 1992, Tang *et al.* [68], demonstrated the first LBO OPO pumped by the fourth harmonic of an Nd:YAG laser at 266 nm. Their OPO generated signal output at 314 nm, which is the shortest OPO output obtained up to that date. Threshold pump intensity was 10 MW/cm², and they obtained 25% pump depletion and 10% conversion to signal and idler.

In the same laboratories, Cui *et al.* performed two consecutive LBO OPO experiments by using the third harmonic of Nd:YAG laser as the pump source [69], [70]. In 1992, they constructed a type II NCPM LBO OPO tunable over 481–457 nm and 1355–1590 nm. Threshold energy was 0.4 mJ. They achieved 50% pump depletion and 27% total conversion efficiency. In 1993, in a type I critically phase matched LBO OPO experiment, they obtained 35% pump depletion and 0.3 mJ threshold energy [70]. The signal and the idler beams were tuned in 455–665 nm and 760–1620 nm spectral ranges, respectively.

In 1994, Schröder *et al.* [72] reported LBO OPO experiments, and presented the spectral properties of the OPO's with a numerical model. In the experiments, they pumped the OPO's by the second, third, or fourth harmonic of injection seeded Nd:YAG lasers. They obtained the widest tuning range (from 414 nm to 2.47 μ m) in a type I critically phase matched OPO with the third harmonic of the Nd:YAG laser as the pump source. In this case, total conversion efficiency was approximately 45%.

3.3 Nanosecond OPO's in Mid-IR

Remote chemical sensing in 3–5 μ m and 8–12 μ m spectra is important in some military and civilian applications. OPO's employing AgGaSe₂, AgGaS₂, Tl₃AsSe₃, and CdSe crystals are promising sources in the mid-IR spectral range [6].

Eckardt, *et al.* [73] conducted the first AgGaSe₂ OPO experiment in 1986. They achieved tuning ranges of 1.6–1.7 μ m and 6.7–6.9 μ m when pumped by

an Nd:YAG laser at $1.34\ \mu\text{m}$; and tuning ranges of $2.65\text{--}9.02\ \mu\text{m}$ when pumped by an Ho:YLF laser at $2.05\ \mu\text{m}$. In the experiments, they achieved conversion efficiencies up to 18%.

In another experiment, Kirton [74] pumped an AgGaSe₂ OPO by the output of a LiNbO₃ OPO generating $2.54\ \mu\text{m}$ signal. The signal and idler wavelengths of the AgGaSe₂ OPO were $4.1\ \mu\text{m}$ and $6.7\ \mu\text{m}$, respectively. They measured the OPO threshold energy as 0.6 mJ, and conversion efficiency as 0.5%.

By constructing two different OPO's pumped by the same laser, Allik *et al.* [75] obtained OPO outputs covering the whole $7\text{--}12\ \mu\text{m}$ spectral range. They carried out Cr,Er:YSGG laser pumped (at $2.79\ \mu\text{m}$) CdSe OPO experiments generating outputs at $8.5\text{--}12.3\ \mu\text{m}$ spectral range with a 39% total conversion efficiency. They also presented ZnGeP₂ OPO experiments pumped by the same laser with a tuning range of $6.9\text{--}9.9\ \mu\text{m}$, and achieved 29% total conversion efficiency.

In this chapter, nanosecond OPO experiments are reviewed. As a result of advances in nonlinear crystal technology, OPO's are becoming powerful solid state sources of tunable radiation. In the earlier days, OPO's were operating in the near-IR (usually LiNbO₃ OPO's) where the OPO crystals suffered from low threshold energies. Nowadays, KTP, BBO and LBO are the most widely used nonlinear crystals. In many nanosecond OPO experiments high conversion efficiencies are obtained. Moreover, tunable OPO's with very large tuning ranges (from $0.4\ \mu\text{m}$ to $2.5\ \mu\text{m}$ [53], [57]) were reported.

Using OPO's in frequency conversion has important practical consequences, such as obtaining eye-safe radiation from an OPO. In 1993, Marshall *et al.* [29] reported 47% power conversion efficiency to eye-safe output with a flux grown KTP crystal, and they pumped the OPO's up to 20 mJ at $1.06\ \mu\text{m}$. In this thesis, we have constructed OPO's for obtaining eye-safe radiation. These OPO's are either pumped at less than 30 mJ (low energy OPO's) or at 100 mJ (high energy OPO's).

Chapter 4

OPO Experiments

The goal of our experiments is to convert the output of Nd:YAG lasers at 1064 nm wavelength to the eye-safe band of the spectrum (1.54–1.60 μm) for two different applications. These applications are range finders generating 15 mJ pulses with 7 ns pulse duration, and target designators generating 100 mJ pulses with 15 ns long pulse duration. For this purpose, we designed, implemented and characterized three different KTP OPO's in three experimental sets. In the first experimental set, the OPO's are pumped up to 20–28 mJ. In the second set, pump beam intensity on the KTP crystal is increased, and the OPO's are pumped up to 15–20 mJ. Therefore, suitable OPO's for low energy applications (range finders) that operate at 15 mJ are provided. In the third set, the OPO's are pumped by pulses of energy up to 100 mJ and duration of 15 ns for high energy applications (target designators). This chapter presents experimental setups and the results of these experiments.

4.1 Experimental Setup

This section presents the properties of the pump laser and the nonlinear crystal (KTP) used in the experiments. After this, cavity configurations are described. Finally, the methods used to characterize the OPO's are discussed.

4.1.1 Pump Laser

In the OPO experiments, we use a flashlamp pumped Q-switched Nd:YAG laser (Powerlite 6020, by Continuum) at 1064 nm wavelength. This laser is an electro-optically Q-switched laser generating 20 pulses in a second (20 Hz repetition rate).

Q-switching is one of the common methods to obtain nanosecond pulses. In a Q-switched laser, resonator loss is increased periodically. During the high loss period, the inverted population of the laser gain medium increases since there is no oscillation. When the loss is reduced suddenly by the Q-switch, oscillation starts and a pulse is generated.

Q-switch delay is the time delay from the on-time of the flashlamp to the on-time of the Q-switch. The energy and duration of the pulses depend on the Q-switch delay of the laser. In the experiments, pump pulses with two different pulse durations (7 ns and 15 ns) are generated by adjusting the Q-switch delay appropriately.

The laser generates pulses up to 300 mJ energy. In the first two experimental sets where the pump energy values are less than 30 mJ, the OPO pump is obtained by the surface reflection of the full energy beam from a glass wedge. In all experiments, variable OPO pump energies are obtained by using a half wave plate and a polarizer.

4.1.2 Crystal

In the experiments, a hydrothermally grown KTP crystal produced by Cleveland Crystals is used. The KTP crystal is 22.4 mm long, with a 6.0×6.0 mm cross sectional area. It has anti-reflection coatings for both signal and pump wavelengths with reflectivities of less than 1.0% and 1.5%, respectively.

For KTP OPO/OPA experiments, usually type-II phase matching is used because of the higher effective nonlinear coefficient of type-II interactions. It is also preferable to achieve phase matching along one of the optic axis of the crystal because of zero walkoff angle. In these experiments, the direction of the propagation is along the x axis, so phase matching condition is satisfied at $\theta = 90^\circ$ and $\phi = 0^\circ$. The effective nonlinear coefficient is 3.6×10^{-12} m/V [76].

When type-II NCPM interaction is employed with 1064 nm pump beam, the signal and idler wavelengths are computed as 1571 nm and 3297 nm, respectively, where the signal wavelength is in the defined eye-safe band. The signal and the pump beams are both p-polarized (fast axes), and the idler is s-polarized (slow axis).

Refractive indices on the x , y and z axes of the KTP crystal depend on the

wavelengths (λ) according to the Sellmeier equations [77]

$$n_i = A_i + \frac{B_i \lambda^2}{\lambda^2 - C_i^2} - D_i \lambda^2 \quad i = x, y, z \quad (4.1)$$

where A_i, B_i, C_i , and D_i are the Sellmeier coefficients, and λ is in μm 's. Sellmeier coefficients for hydrothermally grown KTP crystals are given in Table 4.1 [77].

	A	B	C	D
x	2.1146	0.89188	0.20861	0.01320
y	2.1518	0.87862	0.21801	0.01327
z	2.3136	1.00012	0.23831	0.01679

Table 4.1: Sellmeier coefficients of hydrothermally grown KTP crystals

Using the Sellmeier equations, the refractive indices of each wave are calculated as:

	Refractive index
pump	1.74754
signal	1.73635
idler	1.77102

Table 4.2: The computed refractive indices that pump, signal and idler experience in NCPM type-II interaction.

In the experiments, the damage threshold of the KTP is an important restriction on the peak pump intensity values. The damage threshold of the KTP crystals are reported as approximately $1 \text{ GW}/\text{cm}^2$ at 1064 nm [6]. In the single-pass and double-pass OPO experiments, we applied pulses having peak intensities less than $250 \text{ MW}/\text{cm}^2$, and $200 \text{ MW}/\text{cm}^2$, respectively. We estimate the surface damage threshold of the KTP between $0.5\text{--}1 \text{ GW}/\text{cm}^2$.

4.1.3 Cavity Configurations

In the experiments, OPO's with two different cavity configurations have been constructed. In one configuration, the pump beam passes through the cavity once (single-pass OPO). Therefore, depleted pump is coupled out of the OPO cavity besides the signal beam. The signal and the depleted pump are separated

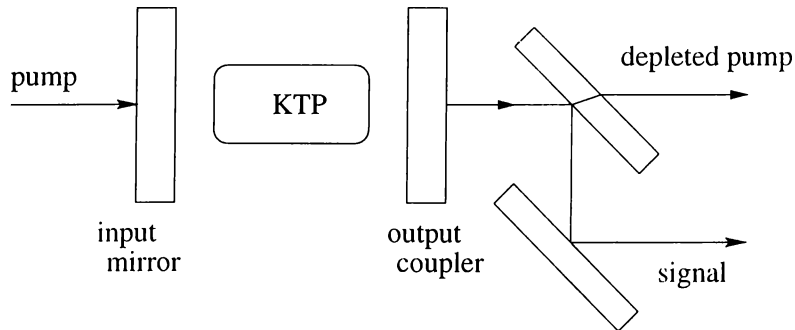


Figure 4.1: Single-pass OPO configuration.

by using a dichroic mirror. Since this dichroic cannot remove the depleted pump from the signal totally, we use an extra dichroic to remove the residual pump from the signal beam (see Figure 4.1). After these reflections from two dichroics, the total loss that the signal beam experiences is 1.5%, and the residual pump remained within the signal is 0.3% of the depleted pump.

In the second cavity configuration, the depleted pump beam is reflected back to the cavity by a high reflector (see Figure 4.2). The high reflector is placed just after the first dichroic, hence, the pump passes through the KTP crystal twice (double-pass OPO). Double passing the pump beam decreases the threshold energy and increases the conversion efficiency. The signal pulse duration also slightly increases when compared to the single-pass OPO's. In the third experimental set, since we deal with high energies (about 100 mJ), back reflecting the pump into the pump laser caused damages on our optics, so we preferred not to send the pump exactly into the laser cavity, but slightly misaligned the direction of the returned pump.

In the OPO cavities, we use an input mirror which transmits the pump, but highly reflects the signal. The input mirror is either flat or concave. The output

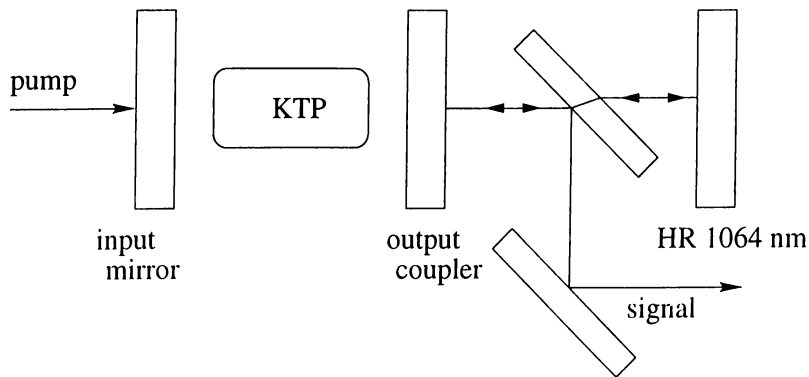


Figure 4.2: Double-pass OPO configuration.

coupling mirrors have different reflectivities (90%, 85%, 80%, 70%, and 60%), and different radii of curvatures (flat mirrors, or mirrors with 2 m or 5 m radii of curvatures). The idler light at $3.3\ \mu\text{m}$ is totally absorbed in the cavity mirrors.

In order to increase the number of round trips of the signal during a pump pulse, the shortest possible OPO cavity length (less than 25 mm) is preferred. However, the effects of the cavity length on conversion efficiencies and pump thresholds are also observed by increasing the cavity length to 3 cm, 5 cm, and 7 cm.

4.1.4 Characterization

In each experimental set, pump threshold energies, conversion efficiencies, pump depletions, temporal and spectral properties, and divergences of the OPO outputs are measured.

The energies of the signal, pump and the depleted pump are measured by an energy meter (LabMaster Ultima energy meter, by Coherent). We maximize the signal outputs of the OPO's by aligning the cavity mirrors and slightly varying the orientation of the KTP crystal. The accuracy of the energy measurements are within an error range of $\pm 5\%$.

Up to a threshold value of the pump pulse energy, no signal output is observed. Indicating the starting point of the OPO operation, the threshold energy is an important measure of performance of an OPO. Experimental measurement of the threshold energy is difficult, because as we approach to the threshold value, the signal fluctuates too much. So, we determine the threshold energies by extrapolating the lower signal energy values that can be measured. As the pump energy increases beyond the threshold, conversion efficiency begins to increase, then reaches a maximum, and after this point saturation starts. The conversion efficiencies are the power conversion efficiencies and obtained by taking the ratio of the signal energy and the corresponding pump energy values. In the experiments, we tried to avoid backconversion, and pumped the OPO's up to approximately 3-4 times the threshold values.

The pump depletion which is sometimes called as internal conversion efficiency, indicates the percentage of the pump energy used throughout the nonlinear interactions in the crystal. In order to determine the net pump depletion value, reflection losses that the pump beam experience are considered.

The pulse durations of the pump and signal pulses are measured by silicon

and germanium photodetectors, respectively.

The spectrum of the signal is measured by a monochromator (CMI 110 Monochromator, by CVI) by using a gated integrator and boxcar averager module (SR250, by Stanford Research Systems). This module generates a continuously adjustable gate in time (approximately 15–30 ns long gates for signal pulses of 7–15 ns at FWHM). We adjust the signal pulse and the gate on top of each other by observing both the pulse and the gate by an oscilloscope. The integrator integrates the input signal during this gate, and the output of the integrator is normalized by the gate width to generate a voltage proportional to the average of the signal during the gate. The input of the monochromator is the output of this integrator. Using this module, the signal pulses are averaged only over the gate durations (on the order of nanoseconds), not also over the durations between the consecutive signal pulses (on the order of milliseconds).

The pump profiles are observed by a CCD camera (Cohu 6400), and the signal profiles are observed by a tube camera (Electrophysics Micronviewer 7290A). Data from the cameras are sent to a laser beam analyzer (Spiricon LBA-100A). The diameters of the beams are determined in such a way that 86.5% of the total energy is included in a circle of this diameter.

The divergence of the signal is either determined by measuring the signal beam widths at various distances far away from the OPO or by measuring the diameter of the signal at the focus of a lens.

4.2 Experimental Results

We first give a brief summary of the experimental results. The results of the experiments are presented in the next three sections: OPO's pumped by the pulse energies up to 20–28 mJ, 15–20 mJ, and 100 mJ.

4.2.1 Summary of the Results

We designed eye-safe OPO's operating at two separate pump energy values for two distinct applications. The first OPO is pumped by an Nd:YAG laser generating 15 mJ pulses with 7 ns pulse duration, and the second OPO is pumped by an Nd:YAG laser generating 100 mJ pulses with 15 ns pulse duration. The optimum designs for these OPO's are constructed by using appropriate pump profiles and output coupler (o.c.) reflectivities.

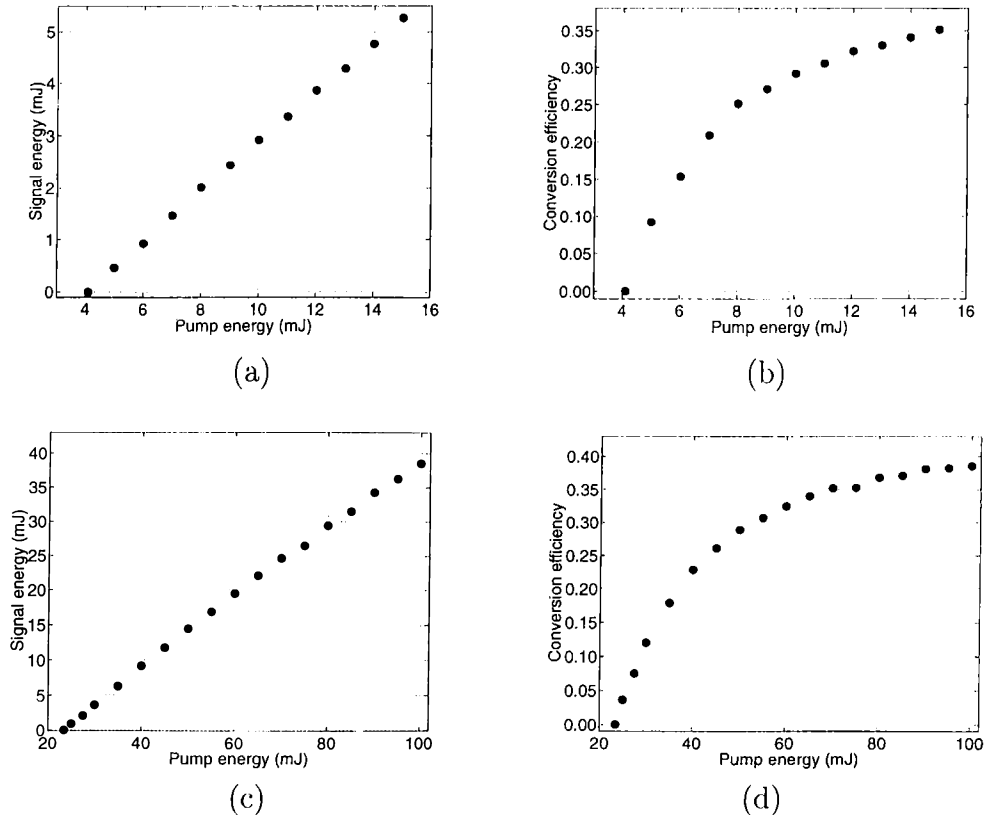


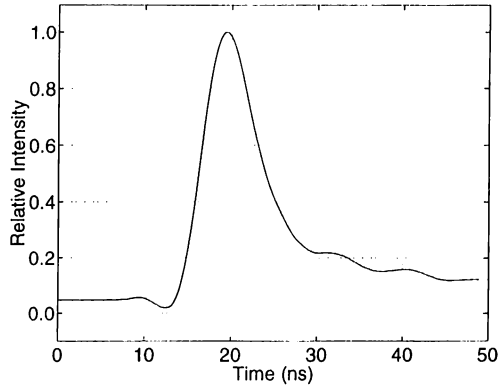
Figure 4.3: (a) Signal energy vs. pump energy and (b) conversion efficiency vs. pump energy plots of the low energy experiments. (c) Signal energy vs. pump energy and (d) conversion efficiency vs. pump energy plots of the high energy experiments.

In the low energy experiments with a $R = 70\%$ o.c., we achieved 35.1% conversion efficiency. The threshold pump energy is measured as 4.1 mJ. In the high energy experiments, the maximum conversion efficiency was 38.5%, and the threshold energy was 23.4 mJ. Figure 4.3 presents the signal energy and conversion efficiency data with respect to the pump energies of these experiments.

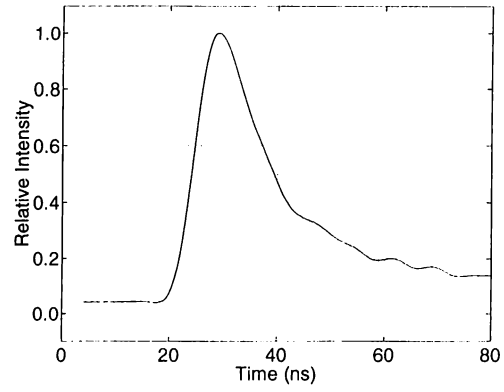
The signal duration of the low energy OPO is 6.7 ns at FWHM whereas this value is 15.4 ns for the high energy OPO. Figure 4.4 shows the oscilloscope traces of the signal pulses in these two experiments.

The OPO's generate eye-safe radiation at 1571-1573 nm. Figure 4.5 shows the spectrum of the signal in both experiments.

We measured 4.2 mrad divergence for the low energy OPO's, and 3.2 mrad divergence for the high energy OPO's. The contour plots of the signal profiles at a 30 cm distance from the OPO cavities of both OPO's are presented in Figure 4.6.

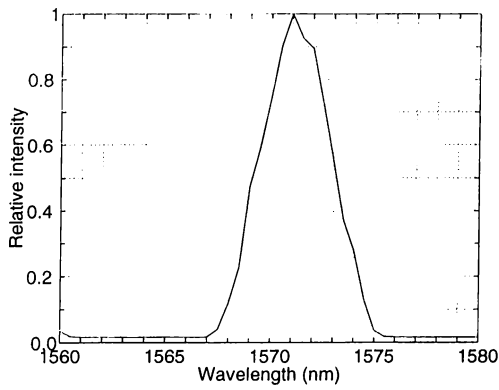


(a)

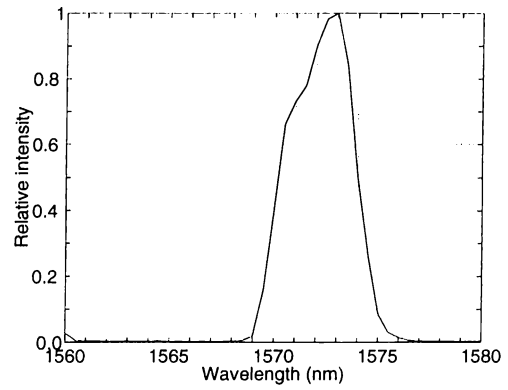


(b)

Figure 4.4: Oscilloscope traces of the signal of (a) the low energy OPO and (b) the high energy OPO.

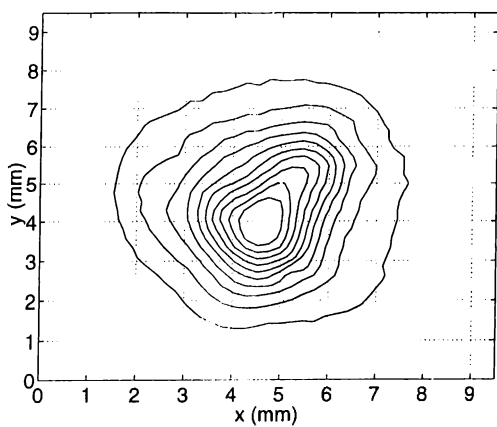


(a)

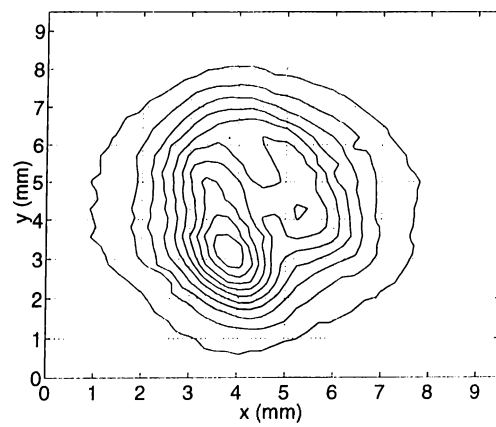


(b)

Figure 4.5: Spectrum of the signal of (a) the low energy OPO and (b) the high energy OPO.



(a)



(b)

Figure 4.6: The signal profile at 30 cm away from (a) the low energy OPO and (b) the high energy OPO.

4.2.2 OPO's Pumped up to 20-28 mJ

In this experimental set, we adjusted the pump intensity by constructing a telescope (see Figure 4.7) which decreases the radius of the Nd:YAG laser output approximately by 2.5 fold. For 1064 nm light, focal lengths of the lenses are 127.1 mm and -50.9 mm, respectively. The pump on the KTP crystal has the profile as seen in Figure 4.8 with a diameter of 2.0 mm.

Single-pass OPO's are pumped up to 28 mJ, and double-pass OPO's are pumped up to 20 mJ. In the single-pass OPO experiments, the applied peak pump intensity is about 230 MW/cm^2 where the average intensity is approximately 120 MW/cm^2 when the pump pulse energy is 28 mJ. In the double-pass OPO's, the peak and the average intensities are approximately 160 MW/cm^2 and 85 MW/cm^2 , respectively, when the pump pulse energy is 20 mJ.

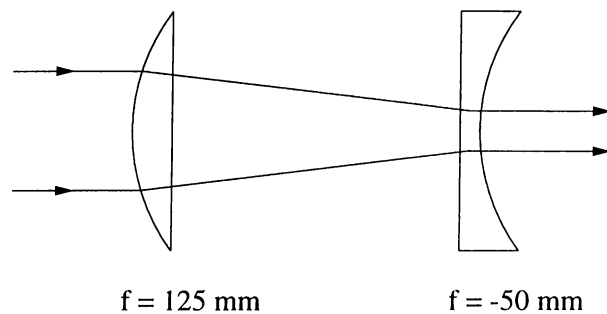


Figure 4.7: Telescope constructed for the first OPO experiment set with focal length values of 127.1 mm and -50.9 mm at 1064 nm. The telescope decreases the radius of the Nd:YAG laser output approximately by 2.5 fold.

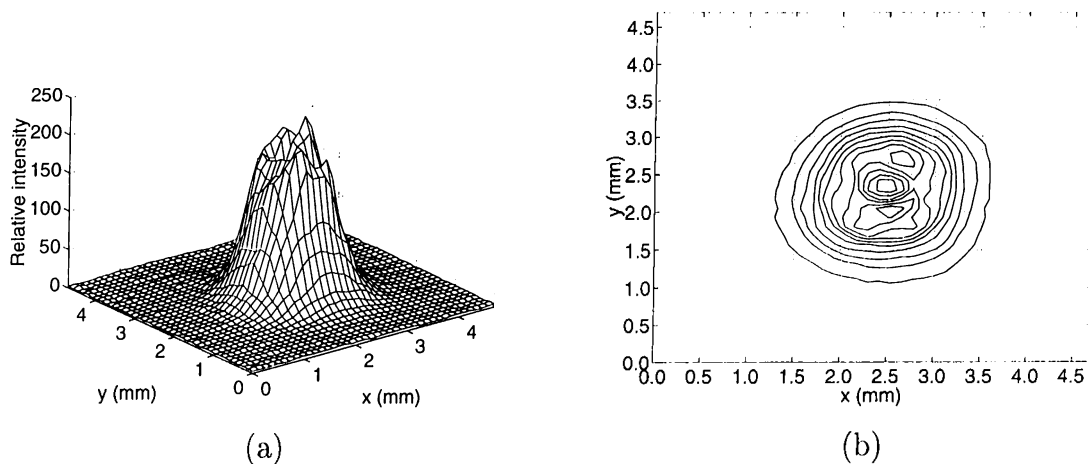


Figure 4.8: Pump profile on the KTP crystal. Pump diameter is 2.0 mm. (a) 3-D plot of the pump pulse. Intensity values are in relative units. (b) Contour plot of the pump pulse.

The results of these experiments are presented in five sections: threshold energy, conversion efficiency and pump depletion, temporal profiles, spectrum, and divergence.

(i) Threshold Energy

As the loss in an OPO cavity increases, the threshold energy increases. In the experiments, we changed the loss by using output couplers (o.c.'s) with different reflectivities. The threshold values for both the single-pass and double-pass OPO's with respect to the o.c. reflectivities are presented in Table 4.3. As the o.c. reflectivity decreases, the threshold energy increases except at a single data point in the single-pass OPO's. Double-passing the pump beam decreases the threshold approximately by twice the threshold values of the single-pass OPO's. Minimum threshold energy is 9.8 mJ in the single-pass configuration, and 5.3 mJ in the double-pass configuration with $R = 90\%$ o.c.

o.c. R (%)	Threshold of single-pass OPO (mJ)	Threshold of double-pass OPO (mJ)
90	9.8	5.3
85	10.0	5.4
80	10.1	5.6
70	12.9	5.7
60	12.4	7.2

Table 4.3: Threshold energies of the single-pass and double-pass OPO's with different output couplers.

(ii) Conversion Efficiency and Pump Depletion

In this experimental set, the maximum conversion efficiency of the single-pass OPO's is 23% when the OPO with a $R = 80\%$ o.c. is pumped by 28 mJ pump energy. We obtained maximum 6.5 mJ signal energy in this case. The pump depletion in this single-pass OPO with $R = 80\%$ o.c. is 44.1% which is also the maximum value among the OPO's with different o.c.'s. So, optimum o.c. reflectivity is 80%.

Figure 4.9 presents signal energy vs. pump energy plots for five different o.c. reflectivities. The maximum conversion efficiencies and pump depletions of the

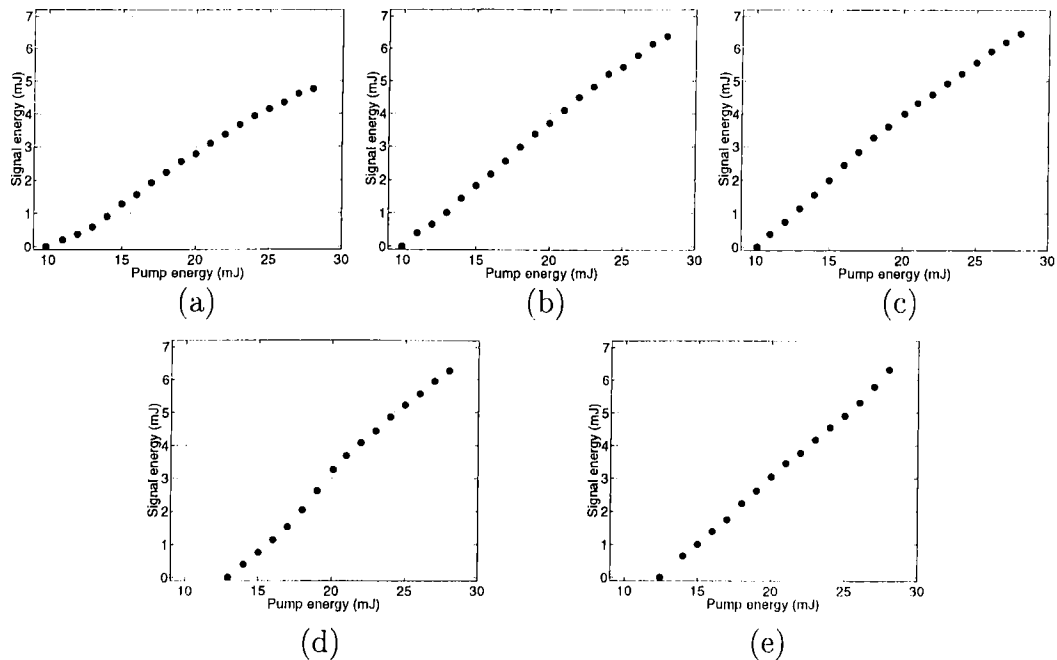


Figure 4.9: Signal energy vs. pump energy plots of the single-pass OPO's with o.c. reflectivities: (a) $R = 90\%$, (b) $R = 85\%$, (c) $R = 80\%$, (d) $R = 70\%$, (e) $R = 60\%$.

o.c. R (%)	Maximum conversion efficiency (%)	Maximum pump depletion (%)
90	17.1	37.4
85	22.8	43.4
80	23.1	44.1
70	22.4	37.9
60	22.6	37.5

Table 4.4: Maximum conversion efficiency and maximum pump depletion data of the single-pass OPO's.

single-pass OPO's are summarized in Table 4.4. The maximum conversion efficiency values vary from 17.1% with an o.c. of $R = 90\%$ up to 23.1% with an o.c. of $R = 80\%$ where the corresponding pump depletions are 37.4% and 44.1%, respectively.

In Figure 4.10 and Figure 4.11 the conversion efficiency and the pump depletion data with respect to the pump energies are shown. As the o.c. reflectivity decreases, the saturation decreases (see Figure 4.10).

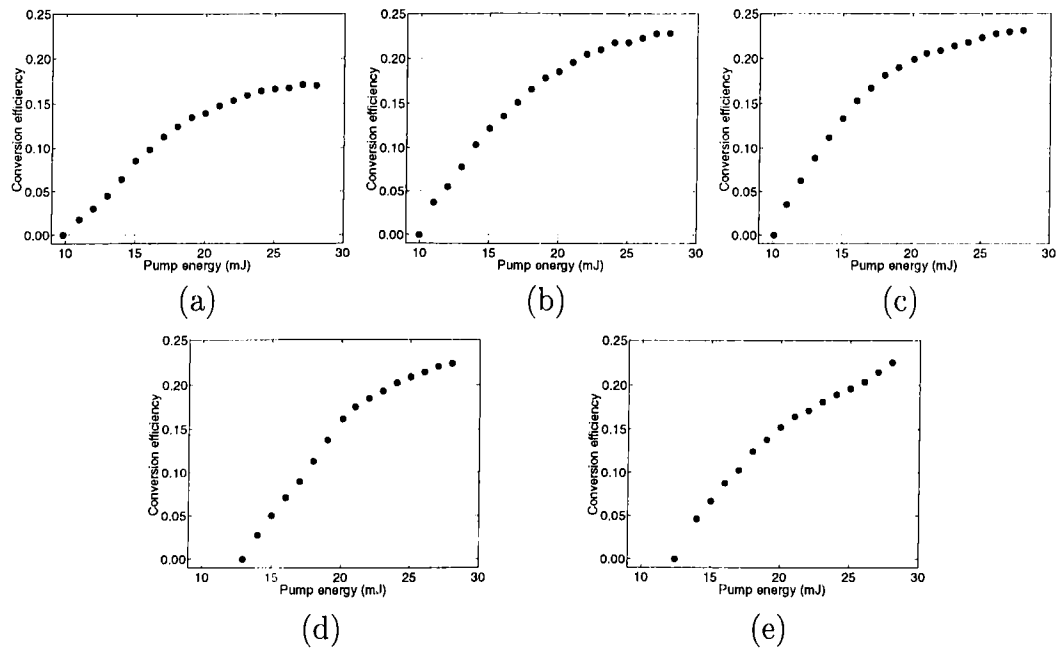


Figure 4.10: Conversion efficiency vs. pump energy plots of the single-pass OPO's with o.c. reflectivities: (a) $R = 90\%$, (b) $R = 85\%$, (c) $R = 80\%$, (d) $R = 70\%$, (e) $R = 60\%$.

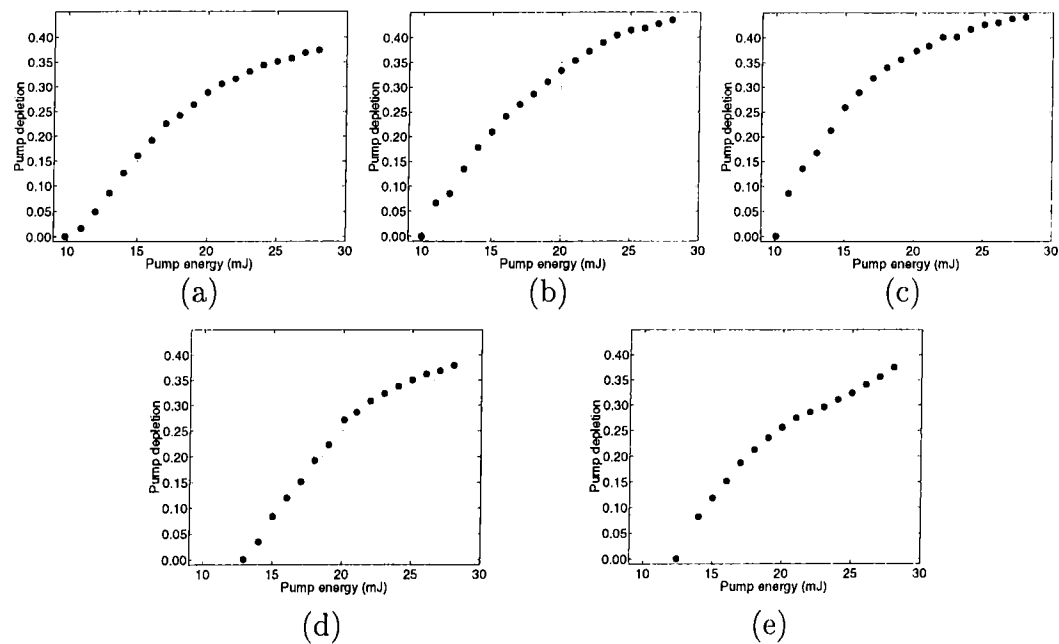


Figure 4.11: Pump depletion vs. pump energy plots of the single-pass OPO's with o.c. reflectivities: (a) $R = 90\%$, (b) $R = 85\%$, (c) $R = 80\%$, (d) $R = 70\%$, (e) $R = 60\%$.

In double-pass OPO's, the conversion efficiency increases significantly compared to the single-pass OPO's. In this case, not to damage the KTP crystal, we applied maximum 20 mJ pump energy. With $R = 70\%$ o.c., we obtained 7.1 mJ signal energy when the OPO is pumped by 20 mJ which corresponds to 35.4% conversion efficiency. This is the maximum conversion efficiency achieved, so optimum o.c. reflectivity is 70%. For the double-pass OPO's, the maximum conversion efficiencies are summarized in Table 4.5.

o.c. R (%)	Maximum conversion efficiency (%)
90	25.8
85	32.6
80	34.0
70	35.4
60	32.3

Table 4.5: The maximum conversion efficiency data of the double-pass OPO's

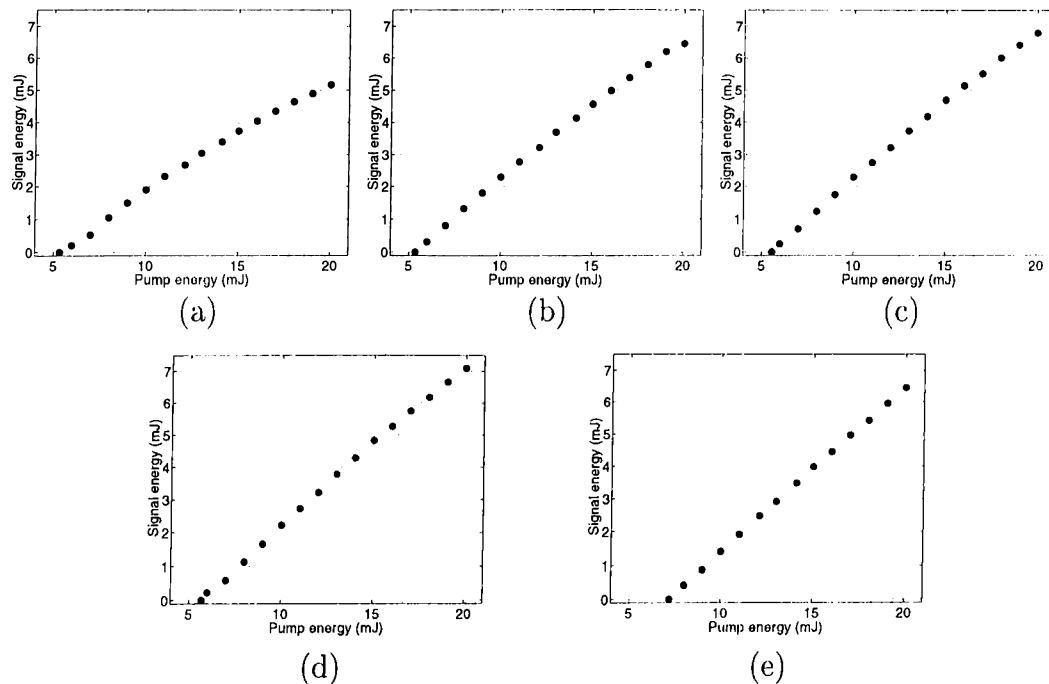


Figure 4.12: Signal energy vs. pump energy plots of the double-pass OPO's with o.c. reflectivities: (a) $R = 90\%$, (b) $R = 85\%$, (c) $R = 80\%$, (d) $R = 70\%$, (e) $R = 60\%$.

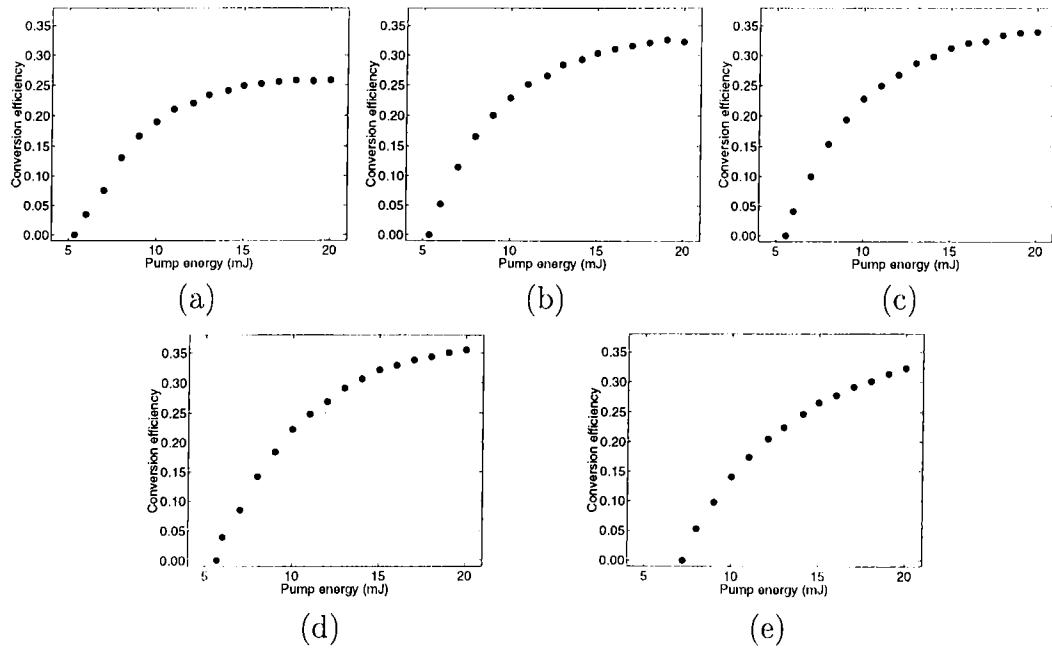


Figure 4.13: Conversion efficiency vs. pump energy plots of the double-pass OPO's with o.c. reflectivities: (a) $R = 90\%$, (b) $R = 85\%$, (c) $R = 80\%$, (d) $R = 70\%$, (e) $R = 60\%$.

In Figure 4.12 and Figure 4.13, the signal energy and conversion efficiency data of double-pass OPO's with respect to pump energy values are shown. In these plots, saturation is observed with o.c.'s of higher reflectivities.

When the pump energies are normalized by the threshold values, we can see how much the OPO's are pumped with respect to the threshold pump energy. For example, in the double-pass OPO configuration, with o.c. $R = 70\%$, the OPO

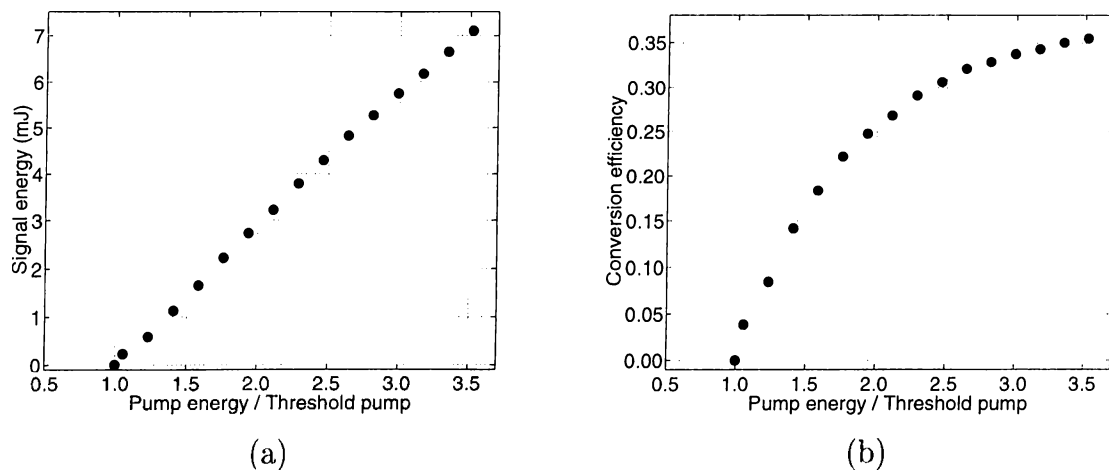


Figure 4.14: (a) Signal energy vs. pump energy normalized with respect to the threshold energy, (b) conversion efficiency vs. pump energy normalized with respect to the threshold energy of the double-pass OPO with o.c. $R = 70\%$.

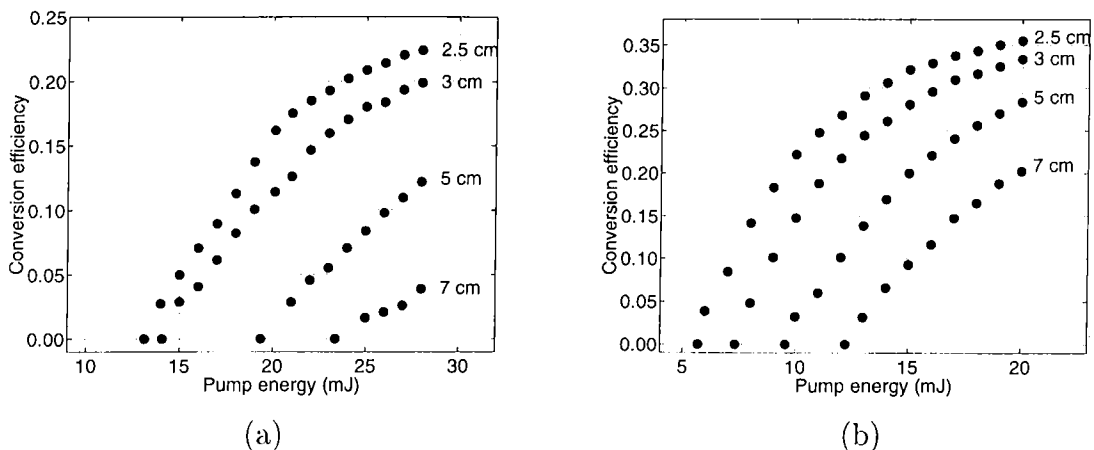


Figure 4.15: Conversion efficiency vs. pump energy data with $R = 70\%$ o.c. of 2.5 cm, 3 cm, 5 cm, and 7 cm long cavities of (a) single-pass OPO, (b) double-pass OPO.

is pumped up to 3.5 times the threshold value (see Figure 4.14).

We observed the dependence of the conversion efficiency on the OPO cavity length experimentally. As the cavity length decreases, the signal makes more round trips, and the conversion efficiency increases. In Figure 4.15, for the cavity lengths of 2.5 cm, 3 cm, 5 cm, and 7 cm conversion efficiencies of the single-pass OPO's and double-pass OPO's are shown. The change in the cavity length affects the double-pass OPO's less than the single-pass OPO's. We also observe improved oscillation stability in the double-pass OPO's compared to the single-pass OPO's.

(iii) Temporal Profiles

In the experiments, the signal and pump pulse durations of both single-pass and double-pass OPO's, and depleted pump pulse durations of the single-pass OPO's are measured. The full width at the half maximum (FWHM) of the pump pulse is 7 ns in this experiment set. The oscilloscope traces of the pump, depleted pump and signal pulses of the single-pass OPO with $R = 70\%$ o.c. are shown in Figure 4.16. In this case, depleted pump is 5.9 ns long, and the signal is 6.5 ns long. In double-pass OPO's, the signal pulses are slightly longer than the single-pass OPO's. The signal duration is 6.7 ns long (Figure 4.17) with $R = 70\%$ o.c.

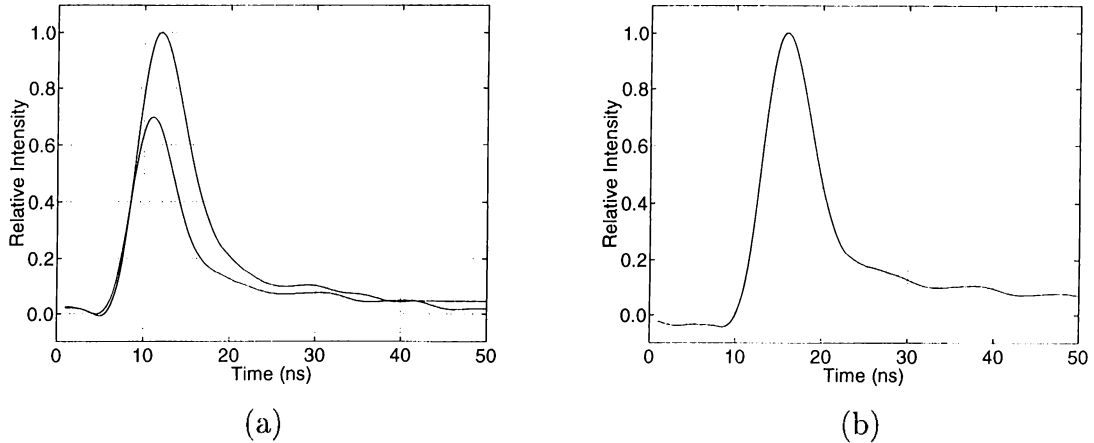


Figure 4.16: Oscilloscope traces of (a) the pump and depleted pump, (b) the signal of the single-pass OPO with $R = 70\%$ o.c.

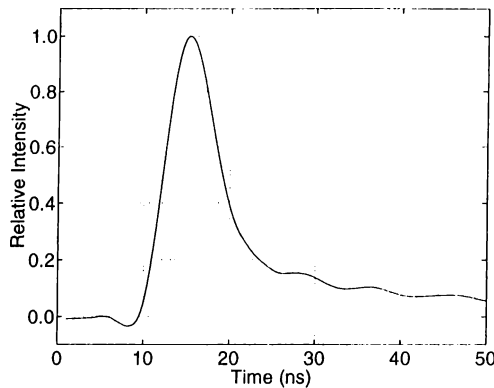


Figure 4.17: Oscilloscope trace of the signal of the double-pass OPO with $R = 70\%$ o.c.

Table 4.6 presents the pulse durations of both double-pass and single-pass OPO's with different o.c. reflectivities. As the o.c. reflectivity decreases, the useful resonator losses increase therefore signal pulse durations decrease. The

R (%)	Single-pass OPO		Double-pass OPO
	Depleted pump (ns)	Signal (ns)	Signal (ns)
90	6.3	7.9	8.6
85	6.2	7.5	7.6
80	6.4	7.4	7.5
70	5.9	6.5	6.7
60	6.3	6.0	6.3

Table 4.6: Pulse durations of both single-pass and double-pass OPO's with different o.c.'s.

minimum signal pulse duration is 6.3 ns with $R = 60\%$ o.c., and the maximum pulse duration is 8.6 ns with $R = 90\%$ o.c. with the same pump pulse duration (7 ns).

(iv) Spectrum

In Figure 4.18, the spectrum of the signal is shown. The OPO signal has its peak value at 1571 nm, which is exactly equal to the computed wavelength by using the Sellmeier coefficients. We performed spectrum measurements for each OPO, and observed similar spectral behavior.

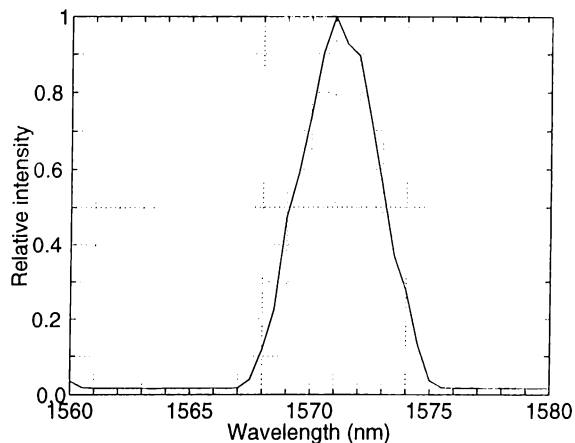


Figure 4.18: Spectrum of the signal.

(v) Divergence

The signal divergence is determined by measuring signal beamwidths at different distances from the OPO cavity. By changing the radii of curvature (RoC) of the OPO mirrors, we formed four different OPO cavities. Each OPO employs $R = 70\%$ o.c. For each cavity, the full-angle signal divergence, threshold energy and maximum conversion efficiency of both single-pass OPO's and double-pass OPO's are measured. The minimum divergence obtained in the experiments is 4.3 mrad in the double-pass OPO with a plane-parallel cavity. The divergences of the single pass OPO's are more than the double-pass OPO's. With a plane-parallel OPO cavity, single-pass OPO divergence is 5.5 mrad whereas in a double-pass plane-parallel OPO cavity, divergence is measured as 4.3 mrad. Similarly with an o.c. of 5 m RoC and plane input mirror, the single-pass and double-pass OPO divergences are 5.6 mrad and 4.6 mrad, respectively. Table 4.7 summarizes the results of these double-pass OPO experiments.

At 30 cm and 80 cm away from the double-pass OPO cavity, signal profiles are presented in Figure 4.19. The signal diameters at these two points are 7.4 mm and 8.3 mm, respectively.

RoC of input mirror	RoC of o.c.	Signal divergence (mrad)	Threshold energy (mJ)	Max. conversion efficiency (%)
∞	∞	4.3	5.6	35.4
∞	5 m	4.6	6.5	32.2
5 m	5 m	5.6	7.1	29.3
∞	2 m	5.5	7.3	26.6

Table 4.7: Signal divergence data of various double-pass OPO cavities. Minimum divergence is 4.3 mrad when the OPO cavity is plane-parallel. Also in this configuration, conversion efficiency is maximum.

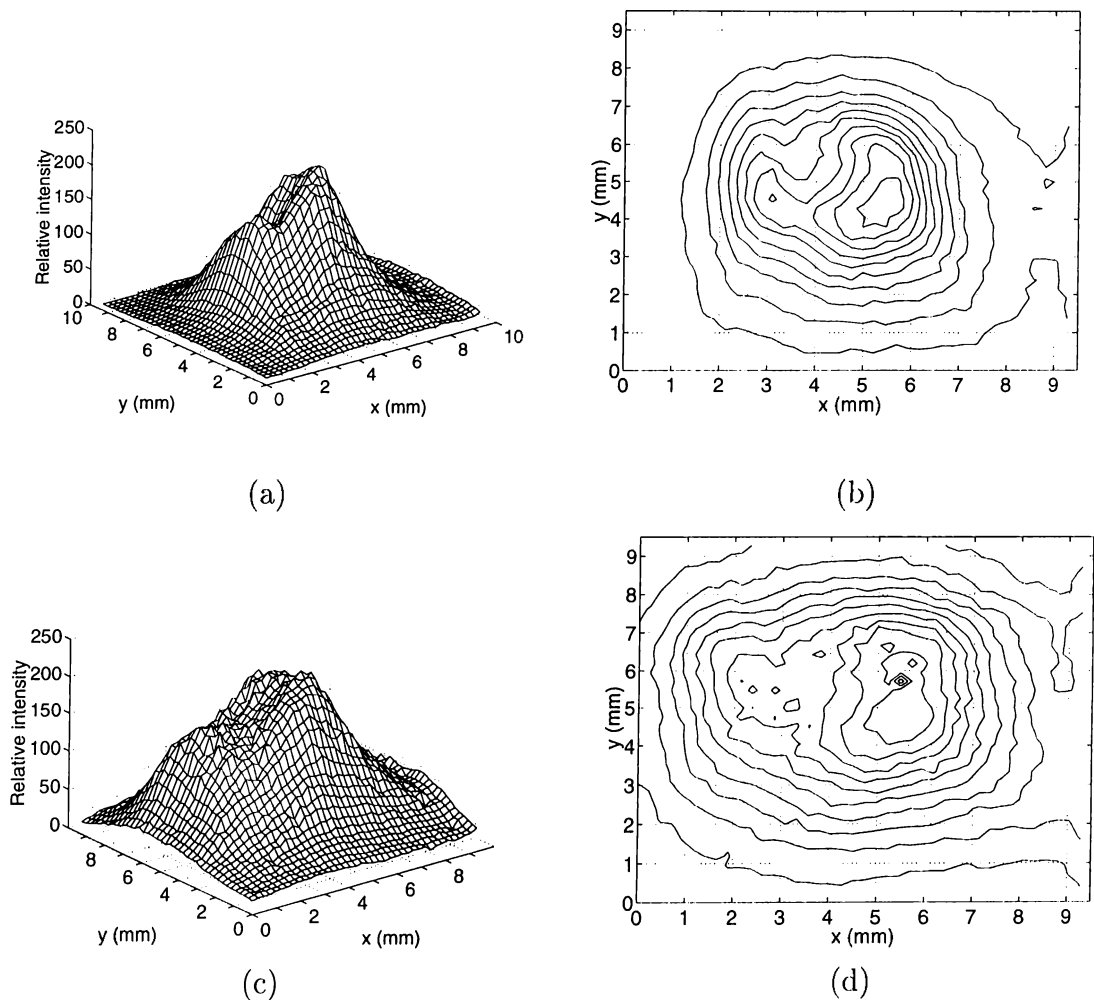


Figure 4.19: Signal profiles of (a) 3-D plot, (b) contour plot at 30 cm away from the plane-parallel double-pass OPO; (c) 3-D plot, (d) contour plot at 80 cm away from the plane-parallel double-pass OPO.

4.2.3 OPO's Pumped up to 15-20 mJ

In the previous experimental set, the maximum conversion efficiency is reached at about 20 mJ pump energies with a double-pass OPO. Since we wanted to maximize the signal output of the OPO's at 15 mJ for range-finding applications, we had to increase the pump intensity by constructing another telescope which decreases the pump diameter. With a telescope decreasing the radius of the output of the Nd:YAG laser by approximately three times, we obtained an OPO pump profile with 1.7 mm diameter. The nominal focal lengths of the lenses of this telescope are 150 mm (152.6 mm at 1064 nm) and -50 mm (-50.9 mm at 1064 nm). The pump profile on the KTP crystal is presented in Figure 4.20.

In this case, maximum 20 mJ pump (approximately 240 MW/cm^2 peak intensity and 125 MW/cm^2 average intensity) is applied in single-pass OPO experiments and 15 mJ pump (approximately 185 MW/cm^2 peak intensity and 95 MW/cm^2 average intensity) is applied in double-pass OPO experiments in order not to damage the KTP crystal with high intensities.

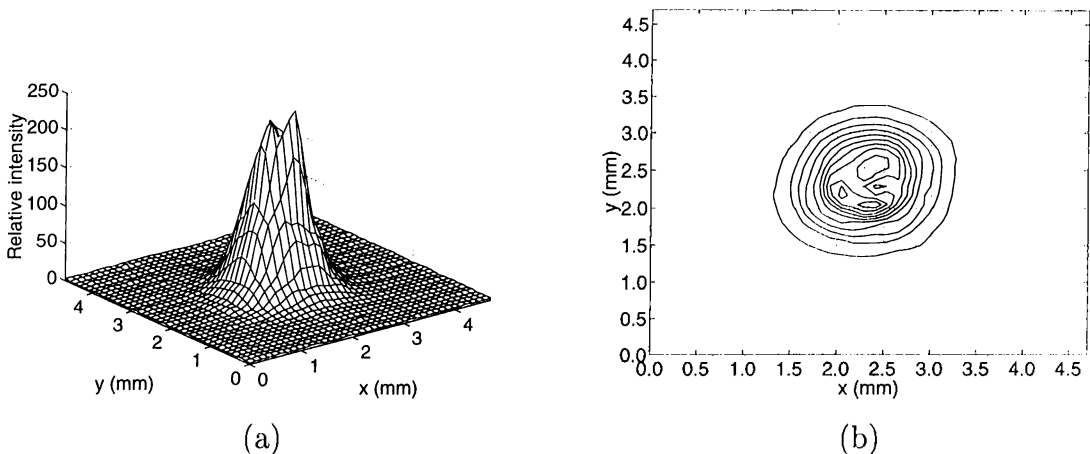


Figure 4.20: Pump profile on the KTP crystal. Pump diameter is 1.7 mm. (a) 3-D plot of the pump pulse. Intensity values are in relative units. (b) Contour plot of the pump pulse.

(i) Threshold Energy

Threshold energy values decrease approximately 30% when compared to the threshold energies of the previous experiment set because of the increase in the intensity. Table 4.8 presents the threshold energies for each o.c. reflectivity values. The maximum threshold energy in the single-pass configuration is 8.2 mJ with an o.c. of $R = 60\%$ whereas the minimum threshold energy is 7.1 mJ with an o.c. of

o.c. R (%)	Threshold of single-pass OPO (mJ)	Threshold of double-pass OPO (mJ)
90	7.2	3.4
85	7.1	3.7
80	7.3	3.7
70	8.4	4.1
60	8.2	4.6

Table 4.8: Threshold energies of the single-pass and double-pass OPO's with different o.c.'s.

$R = 85\%$. In double-pass OPO's, the threshold energies are again approximately half of the single-pass OPO thresholds (minimum 3.4 mJ with $R = 90\%$, and maximum 4.6 mJ with $R = 60\%$ o.c.'s).

(ii) Conversion Efficiency and Pump Depletion

Maximum conversion efficiency achieved in the single-pass OPO configurations is 22.7% when 20 mJ pump is applied with an $R = 60\%$ o.c. In the double-pass OPO experiments this value becomes 35.1% when 15 mJ pump is applied with an $R = 70\%$ o.c. Optimum o.c. reflectivity is 60% in the single-pass OPO's, and 70% in the double-pass OPO's. When compared with the previous pumping configuration, although we reached to the same maximum conversion efficiency values, the optimum o.c. reflectivity values decreased. In Figure 4.21, the signal energy vs. pump energy plots are presented.

Table 4.9 presents the maximum conversion efficiencies and the pump depletions of the single-pass OPO's with different o.c.'s.

In Figure 4.22 and Figure 4.23, the conversion efficiency and the pump depletion data with respect to the pump energy are shown. Except $R = 90\%$ and $R = 85\%$ o.c.'s we do not observe any saturation effect throughout the pumping range.

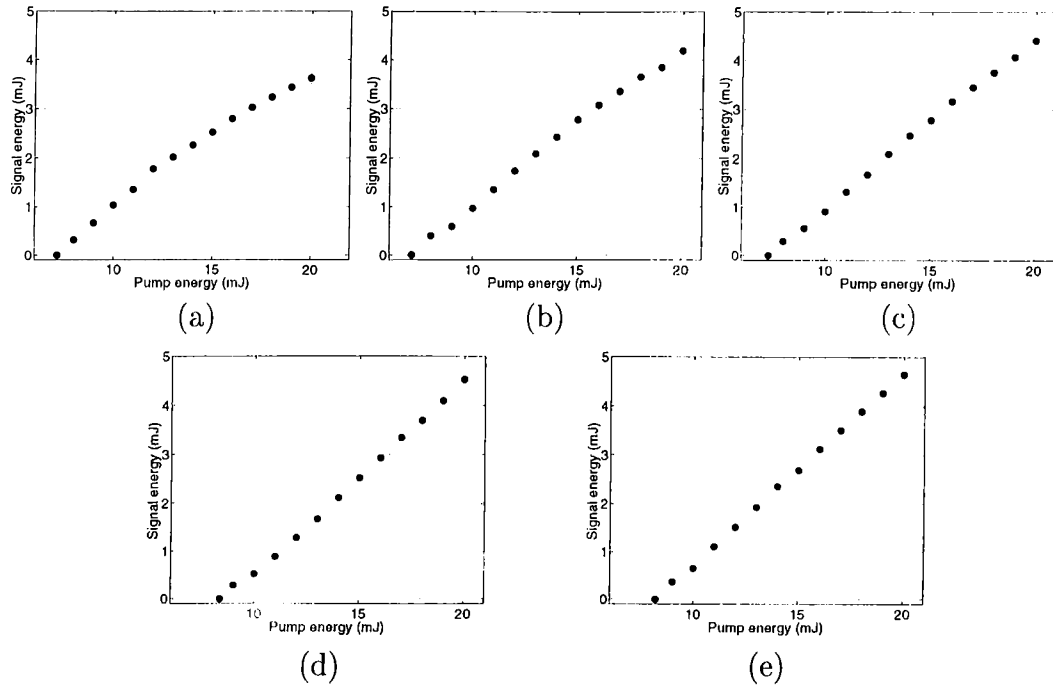


Figure 4.21: Signal energy vs. pump energy plots of the single-pass OPO's with o.c. reflectivities: (a) $R = 90\%$, (b) $R = 85\%$, (c) $R = 80\%$, (d) $R = 70\%$, (e) $R = 60\%$.

o.c. R (%)	Maximum conversion efficiency (%)	Maximum pump depletion (%)
90	18.1	39.7
85	21.0	41.0
80	22.0	40.0
70	22.7	38.1
60	23.2	39.3

Table 4.9: Maximum conversion efficiency and maximum pump depletion data of the single-pass OPO's.

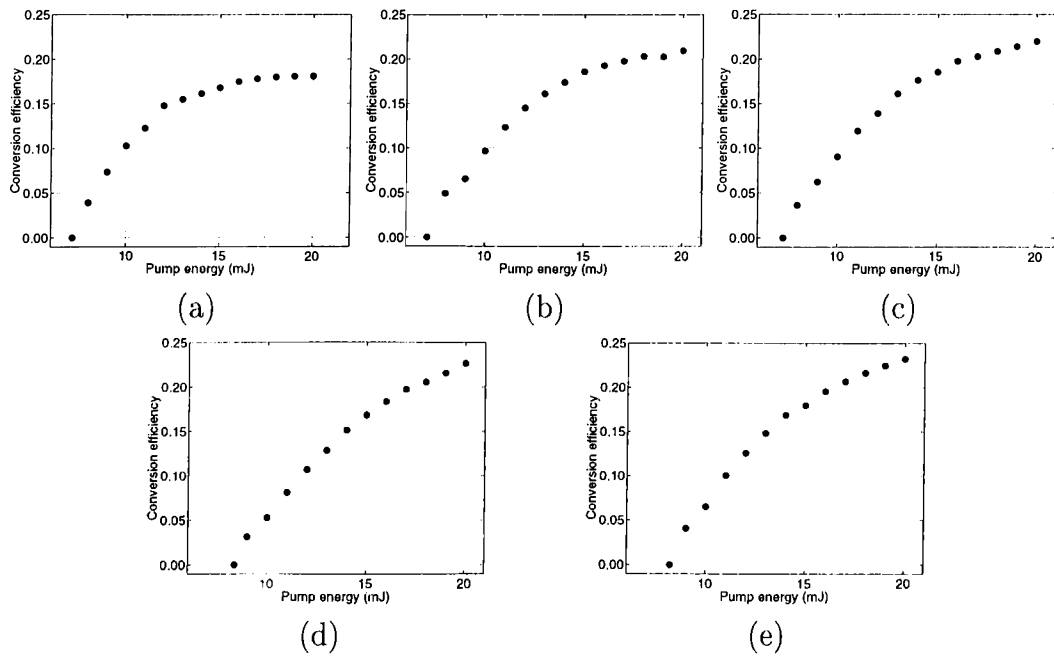


Figure 4.22: Conversion efficiency vs. pump energy plots of the single-pass OPO's with o.c. reflectivities: (a) $R = 90\%$, (b) $R = 85\%$, (c) $R = 80\%$, (d) $R = 7\%$, (e) $R = 60\%$.

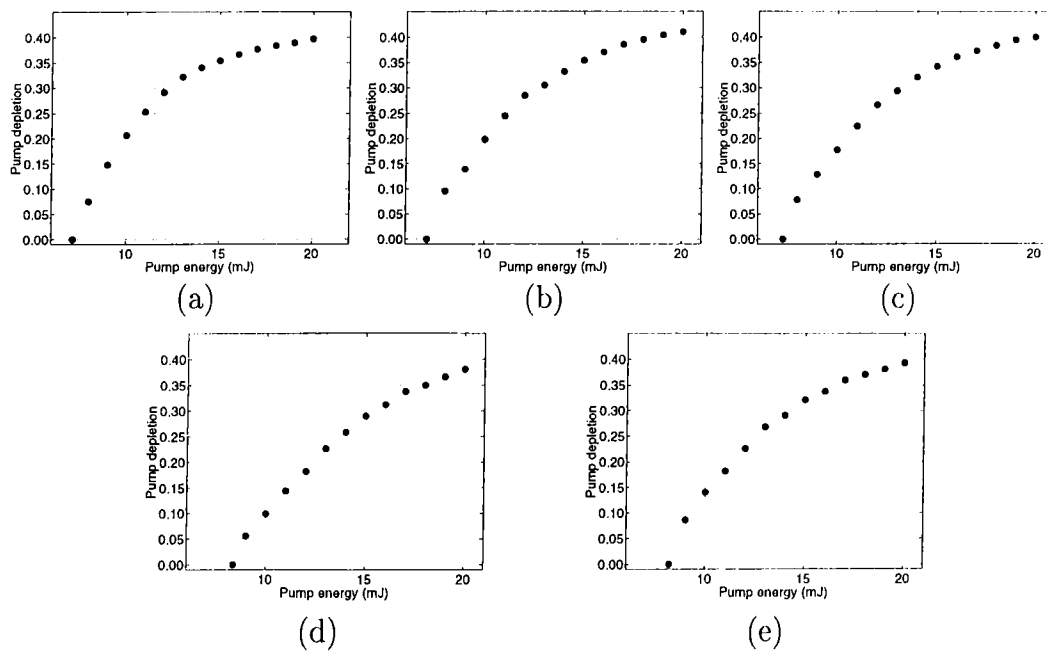


Figure 4.23: Pump depletion vs. pump energy plots of the single-pass OPO's with o.c. reflectivities: (a) $R = 90\%$, (b) $R = 85\%$, (c) $R = 80\%$, (d) $R = 70\%$, (e) $R = 60\%$.

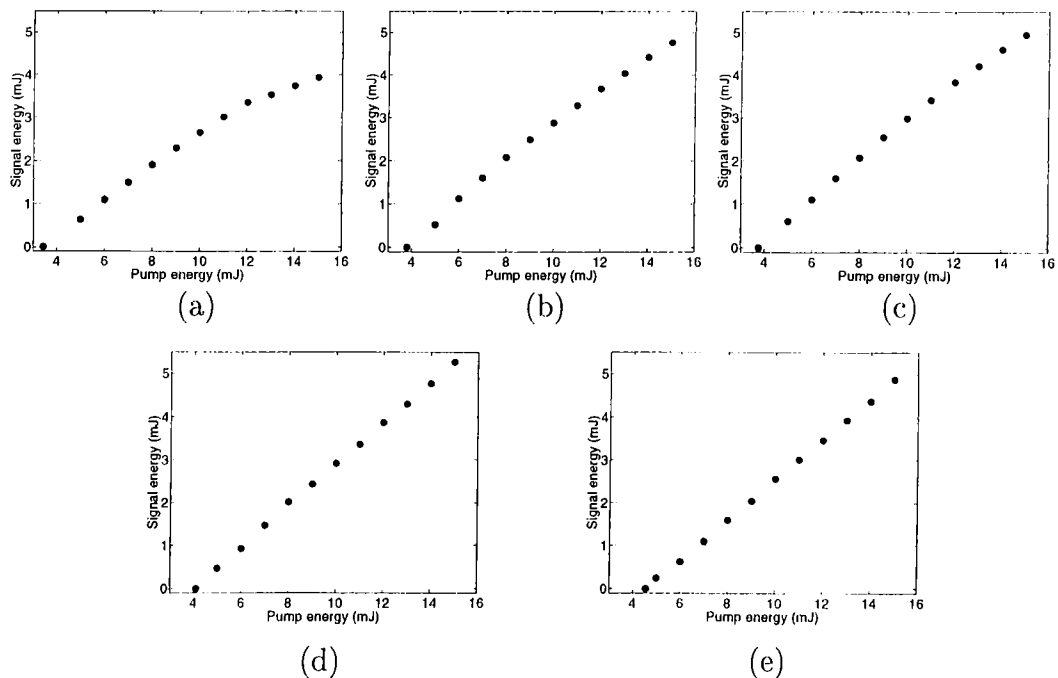


Figure 4.24: Signal energy vs. pump energy plots of the double-pass OPO's with o.c. reflectivities: (a) $R = 90\%$, (b) $R = 85\%$, (c) $R = 80\%$, (d) $R = 70\%$, (e) $R = 60\%$.

In double-pass OPO configurations, we reached approximately the same maximum conversion efficiency values as in the previous experimental set. However in this case optimum o.c. reflectivity is 70%. We obtained 5.3 mJ signal energy corresponding to 15 mJ pump energy (35.1% conversion efficiency) with $R = 70\%$ o.c. For double-pass OPO's, maximum conversion efficiencies are summarized in Table 4.10.

In Figure 4.24 and Figure 4.25 signal energies and the conversion efficiency data with respect to pump energy values are shown. The saturation decreases as the o.c. reflectivity decreases.

In the double-pass configuration with an $R = 70\%$ o.c., we pumped the OPO

o.c. R (%)	Maximum conversion efficiency (%)
90	27.9
85	31.8
80	33.0
70	35.1
60	32.5

Table 4.10: Maximum conversion efficiency data of the double-pass OPO's.

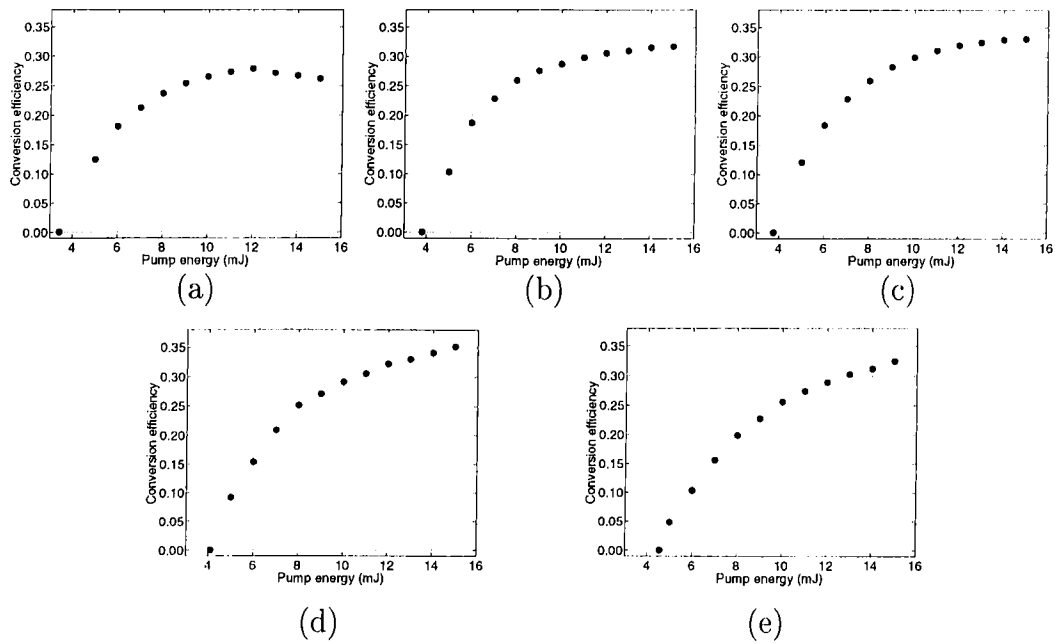


Figure 4.25: Conversion efficiency vs. pump energy plots of the double-pass OPO's with o.c. reflectivities: (a) $R = 90\%$, (b) $R = 85\%$, (c) $R = 80\%$, (d) $R = 70\%$, (e) $R = 60\%$.

more than 3.5 times the threshold value. In Figure 4.26, the signal energies and the conversion efficiencies of the double-pass OPO with $R = 70\%$ o.c. according to the normalized pump energies with respect to the pump threshold energy are presented.

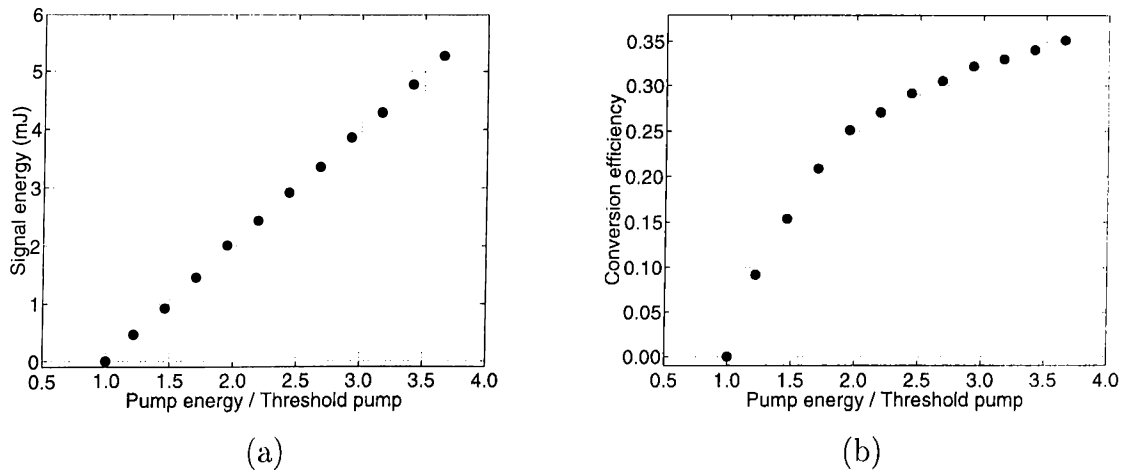


Figure 4.26: (a) Signal energy vs. pump energy normalized with respect to the threshold energy, (b) conversion efficiency vs. pump energy normalized with respect to the threshold energy of the double-pass OPO with o.c. $R = 70\%$.

The dependence of the conversion efficiency on the cavity length is presented in Figure 4.27. In this experiment set, four different cavity lengths, 2.5 cm, 3 cm, 5 cm, and 7 cm are compared. In each cavity o.c. reflectivity is 70%. The conversion efficiency decreases from 35% in the shortest cavity to 24% for 7 cm long cavity in the double-pass configuration, while in the single-pass configuration this decrease is much more drastic: from 23% to 4%.

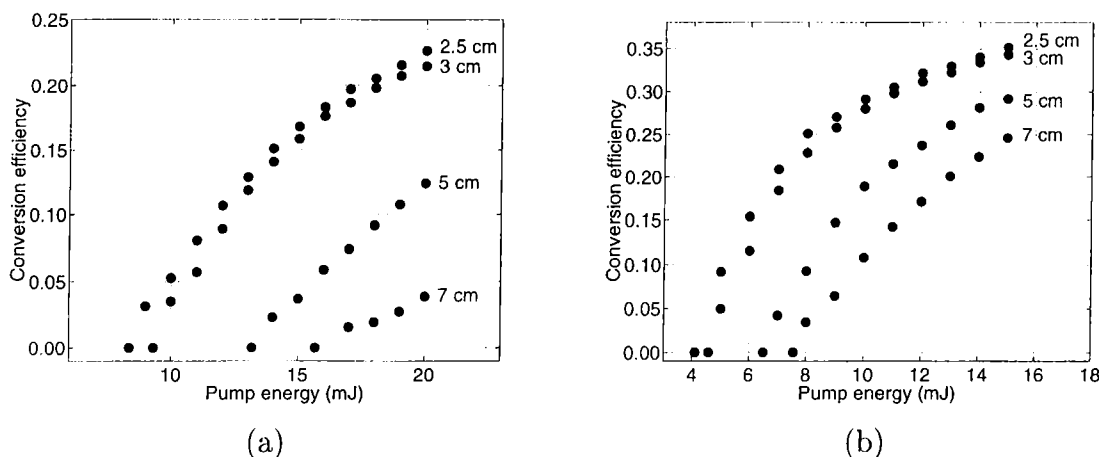


Figure 4.27: Conversion efficiency vs. pump energy data with $R = 70\%$ o.c. of 2.5 cm, 3 cm, 5 cm, and 7 cm long cavities of (a) single-pass OPO, (b) double-pass OPO.

(iii) Temporal Profiles

In this experimental set, the pump is 7 ns at FWHM. The oscilloscope traces of the pump, the depleted pump and the signal pulses of the single-pass OPO with

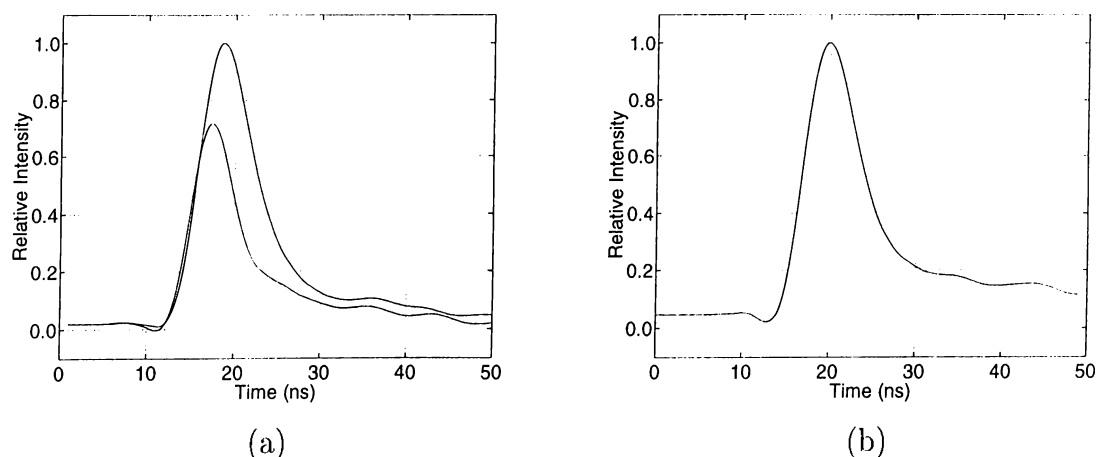


Figure 4.28: Oscilloscope traces of (a) pump and the depleted pump, (b) signal of single-pass OPO with $R = 70\%$ o.c.

$R = 70\%$ o.c. are shown in Figure 4.28. In this case, the depleted pump pulse is 6.1 ns long, and the signal pulse is 7.3 ns long.

In double-pass OPO's, the signal pulse duration is 7.5 ns long which is again slightly longer than the signal pulse duration of the single-pass OPO's with the same o.c. (see Figure 4.29).

Table 4.11 presents the pulse durations of both the double-pass and the single-pass OPO's with different o.c. reflectivities.

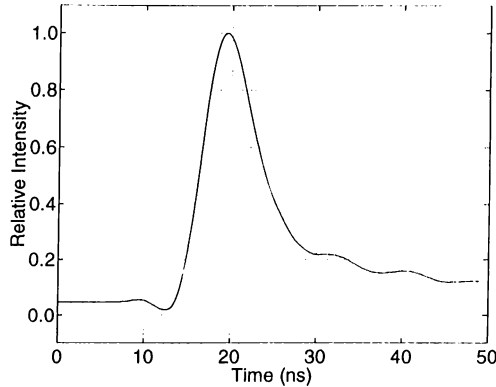


Figure 4.29: Oscilloscope trace of the signal of the double-pass OPO with $R = 70\%$ o.c.

	Single-pass OPO		Double-pass OPO
R (%)	Depleted pump (ns)	Signal (ns)	Signal (ns)
90	6.1	8.5	8.6
85	6.1	7.1	7.2
80	6.0	7.4	8.0
70	6.1	7.3	7.5
60	6.1	6.8	7.0

Table 4.11: Pulse durations of both single-pass and double-pass OPO's with different o.c.'s.

(iv) Spectrum

OPO configurations of this experimental set are the same as the previous set except the pump intensity. As far as the spectrum is concerned, no change is observed. OPO signal has its peak value at 1571 nm as in the previous experimental set.

(v) Divergence

The same types of OPO cavities as in the previous experiment set are constructed for divergence measurements. For each cavity, we measured the signal divergence, threshold energy, and maximum conversion efficiency for the single-pass OPO's and the double-pass OPO's with $R = 70\%$ o.c. The minimum divergence obtained in the experiments is 4.2 mrad in a double-pass OPO configuration with plane-parallel cavity, which is nearly the same as the measurement of the previous experimental set (4.3 mrad). At 30 cm and 70 cm away from the double-pass OPO cavity, the signal profiles are presented in Figure 4.30 with diameters of 6.4 mm and 8.0 mm, respectively. Table 4.12 summarizes the results of these experiments.

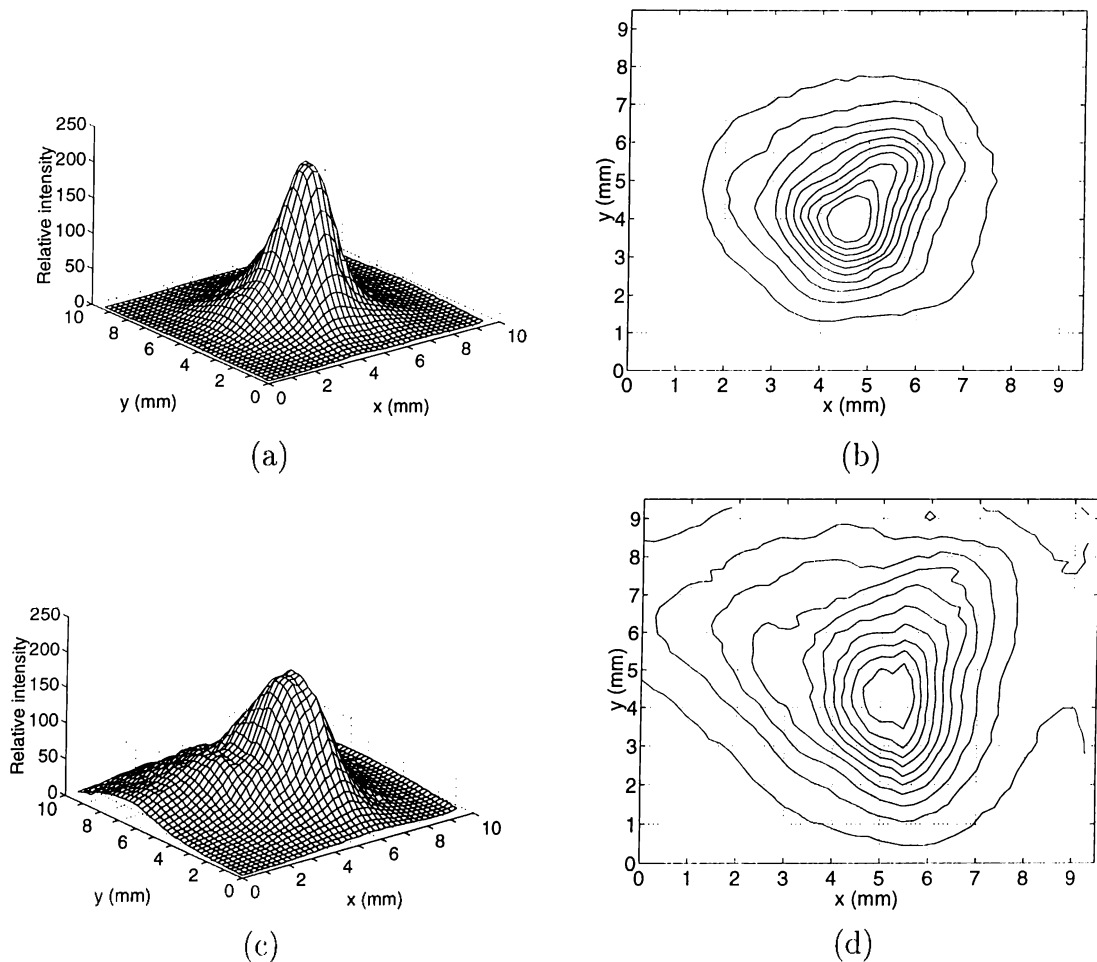


Figure 4.30: Signal profiles of (a) 3-D plot, (b) contour plot 30 cm away from the plane-parallel double-pass OPO, and (c) 3-D plot, (d) contour plot 70 cm away from the plane-parallel double-pass OPO.

RoC of input mirror	RoC of o.c.	Signal divergence (mrad)	Threshold energy (mJ)	Max. conversion efficiency (%)
∞	∞	4.2	4.1	35.1
∞	5 m	4.5	4.6	31.9
5 m	5 m	7.2	4.2	31.5
∞	2 m	5.2	4.7	28.1

Table 4.12: Signal divergence data for various double-pass OPO cavities. Minimum divergence is 4.2 mrad when the OPO cavity is plane-parallel. Also in this configuration, conversion efficiency is maximum.

4.2.4 OPO's Pumped up to 100 mJ

At this experimental set, our goal was to construct OPO's operating at higher pump energies for the target designator applications. The OPO's are designed to operate around 100 mJ, and pump pulse duration should be about 15 ns.

The pump intensity is adjusted by a telescope with nominal focal lengths of 75 mm (85.8 mm at 1064 nm) and -50 mm (-57.4 mm at 1064 nm) lenses which decreases the output radius of the Nd:YAG laser by 1.5 times. The pump diameter on the KTP crystal is 3.0 mm. The pump intensity profile is shown in Figure 4.31.

The OPO's are pumped up to 100 mJ, and we achieved the required performance for the conversion efficiency (more than 38%) with a double-pass OPO configuration. In the experimental setup, since the laser was operated at high power values, the back reflections of the OPO mirrors into the pump laser caused

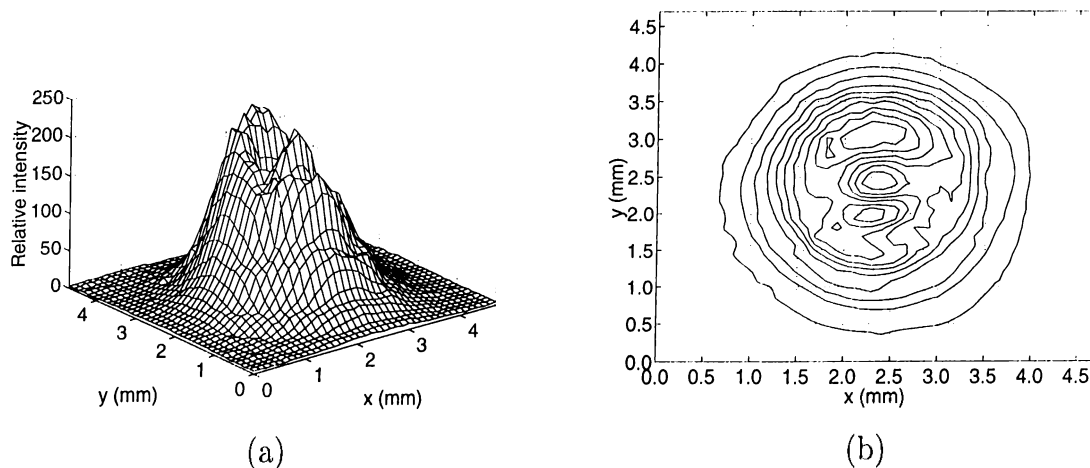


Figure 4.31: Pump profile on the KTP crystal. Pump diameter is 3.0 mm. (a) 3-D plot of the pump pulse. Intensity values are in relative units. (b) Contour plot of the pump pulse.

the pump laser to generate giant pulses which damaged our optics. So, we misaligned the cavity axis from the pump pulse direction by approximately 0.5° . By doing it this way, we could stop back reflections, and in the double-pass OPO experiments, the depleted pump is not sent back into the laser but shifted slightly from the incoming pump direction.

(i) Threshold Energy

The threshold values of the single-pass OPO experiments with o.c. reflectivities of 80%, 70%, and 60% are presented in Table 4.13 where the minimum threshold of 31.6 mJ is achieved by using an $R = 60\%$ o.c.

A double-pass OPO experiment is performed with the $R = 60\%$ o.c. where the threshold energy is 23.4 mJ.

o.c. R (%)	Threshold of single-pass OPO (mJ)
80	37.6
70	37.0
60	31.6

Table 4.13: Threshold energies of the single-pass OPO's with different o.c.'s.

(ii) Conversion Efficiency

The signal energy values with respect to the pump energy values of the single-pass OPO's are presented in Figure 4.32. As the o.c. reflectivity increases, the saturation increases (see Figure 4.33). In order to prevent saturation, we should either decrease the pump intensity by broadening the pulse area, or increase the useful loss by using o.c.'s with low reflectivities.

Table 4.14 presents the maximum conversion efficiencies and the pump depletions of the single-pass OPO's. In this case maximum conversion efficiencies are approximately equal to each other.

In single-pass OPO experiments maximum pump depletion is 46.5% (o.c. $R = 80\%$). The depletions are presented in Figure 4.34.

Since the least saturation in the single-pass OPO's is observed with $R = 60\%$ o.c.; we performed double-pass OPO experiments with this o.c. In this case

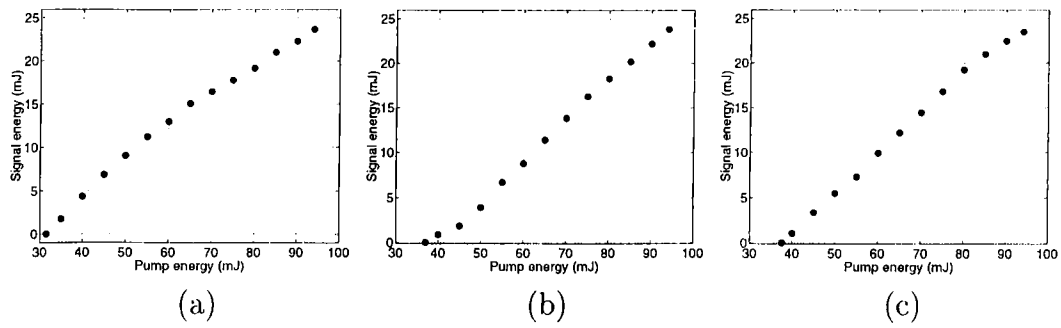


Figure 4.32: Signal energy vs. pump energy plots of the single-pass OPO's with o.c. reflectivities: (a) $R = 80\%$, (b) $R = 70\%$, (c) $R = 60\%$.

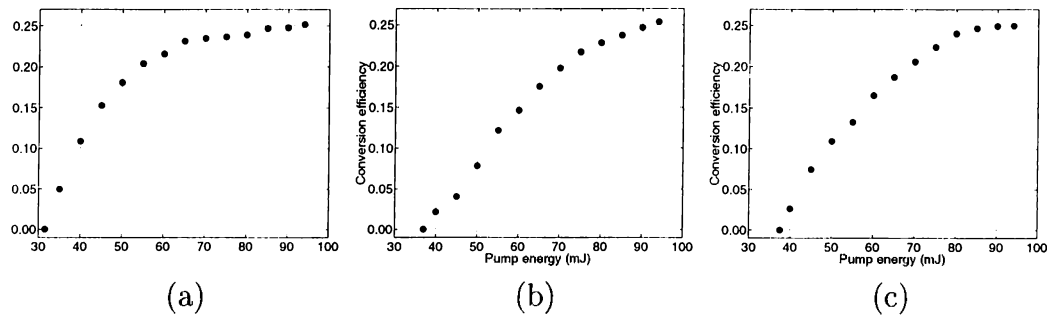


Figure 4.33: Conversion efficiency vs. pump energy plots of the single-pass OPO's with o.c. reflectivities: (a) $R = 80\%$, (b) $R = 70\%$, (c) $R = 60\%$.

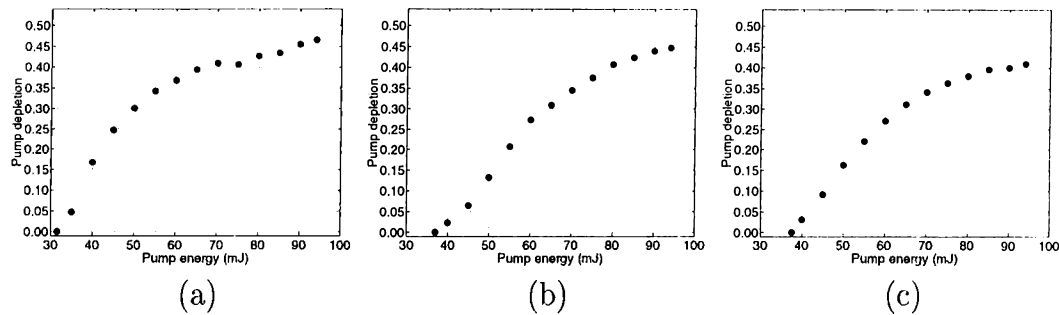


Figure 4.34: Pump depletion vs. pump energy plots of the single-pass OPO's with o.c. reflectivities: (a) $R = 80\%$, (b) $R = 70\%$, (c) $R = 60\%$.

o.c. R (%)	Maximum conversion efficiency (%)	Maximum pump depletion (%)
80	25.2	46.5
70	25.4	44.7
60	25.0	41.0

Table 4.14: Maximum conversion efficiency and maximum pump depletion data of the single-pass OPO's.

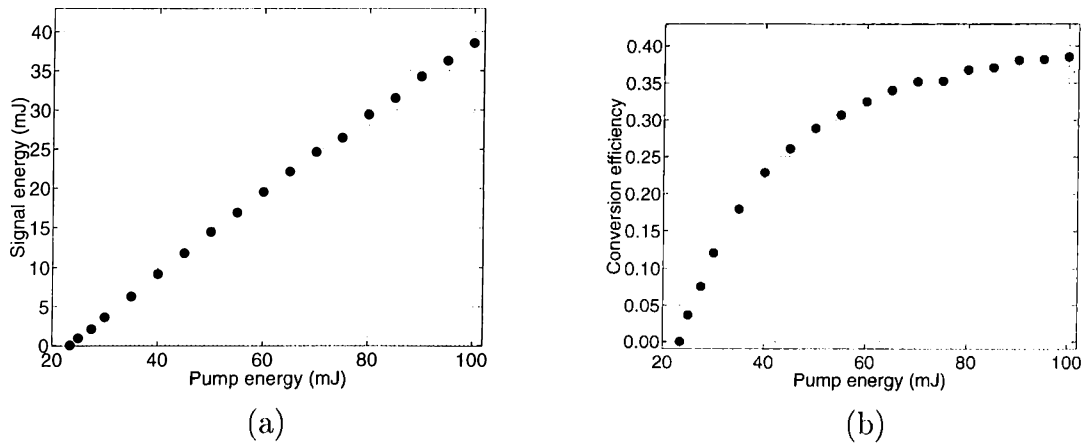


Figure 4.35: In double-pass configuration with $R=60\%$ o.c. 38.5 mJ signal is obtained when 100 mJ pump is applied to the system. (a) Pump energy versus signal energy plot, (b) pump energy versus conversion efficiency plot.

maximum conversion efficiency is measured as 38.5%. The signal energy and the conversion efficiency data with respect to the pump energies are presented in Figure 4.35. In this case, in the double-pass pumping configuration OPO was pumped more than 4 times the threshold value. In Figure 4.36, the signal energies and the conversion efficiencies of this double-pass OPO according to the normalized pump energies are presented.

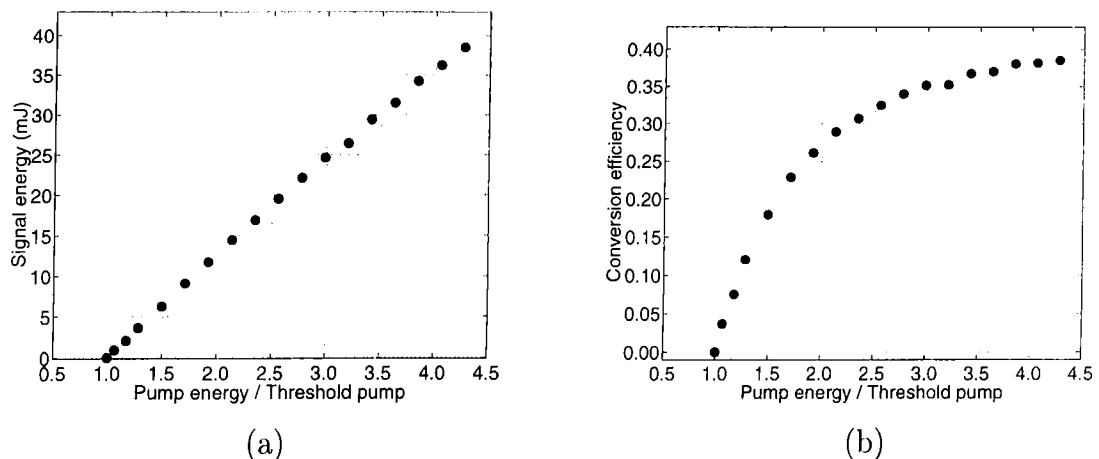


Figure 4.36: (a) Signal energy vs. pump energy normalized with respect to the threshold energy, (b) conversion efficiency vs. pump energy normalized with respect to the threshold energy of the double-pass OPO.

(iii) Temporal Profiles

In this experimental set, the pump pulse duration is adjusted to 14.5 ns by changing the Q-switch delay of the Nd:YAG laser. The signal pulse duration is measured as 15.4 ns in the double-pass configuration with an $R = 60\%$ o.c. Oscilloscope traces of the pump and the signal pulses are shown in Figure 4.37.

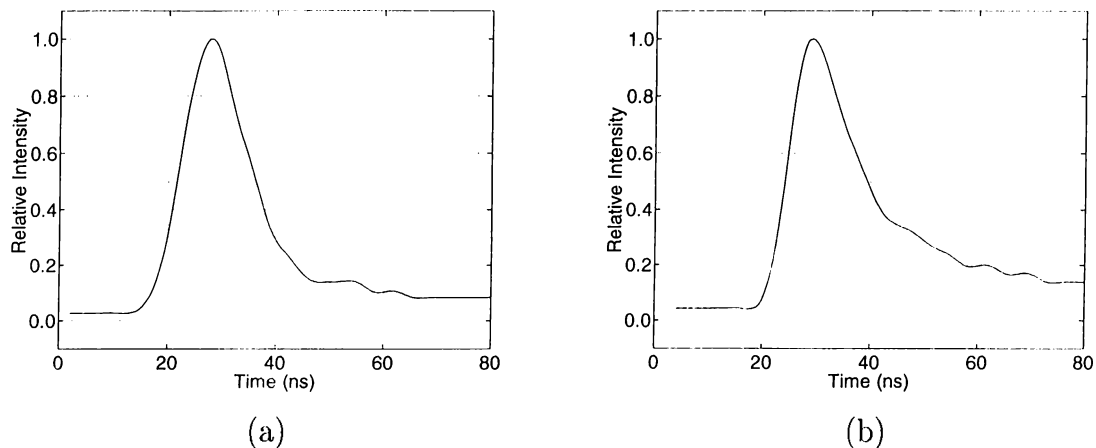


Figure 4.37: Oscilloscope traces of (a) pump and (b) signal of the double-pass OPO.

(iv) Spectrum

In order to prevent the back reflected pump to go into the laser, we slightly misaligned the OPO cavity from the axis of the pump beam. There is approximately 0.5° difference between the direction of the resonated signal beam and the pump beam. So, we disturbed the collinear propagation of the signal and the pump

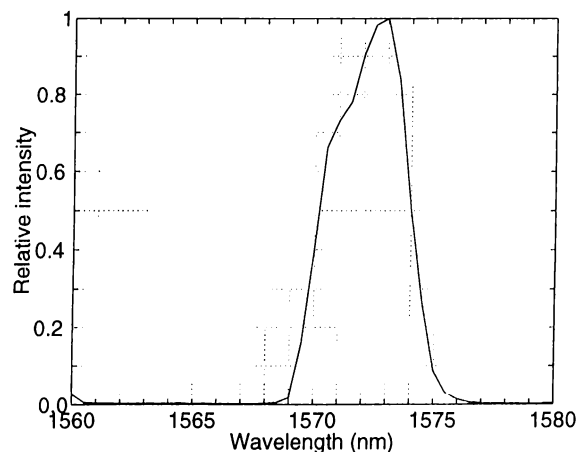


Figure 4.38: Spectrum of the signal.

beams. The phase matching is satisfied in a noncollinear way which results a change in the frequency of the resonant signal. In the experiments, the signal peak in the spectrum is measured as 1573 nm which is 2 nm different from the previous collinear experiments (see Figure 4.38). However this value is still in the eye-safe region.

(v) Divergence

In this case, the signal divergence in the double-pass geometry is measured by two different methods. In the first method, the divergence is determined by measuring the diameters of the signal beam as the signal propagates. The signal profiles at 30 cm away from the OPO and 70 cm away from the OPO are shown in Figure 4.39 where the corresponding diameters are 7.4 mm and 8.2 mm, respectively. The divergence is 2.0 mrad.

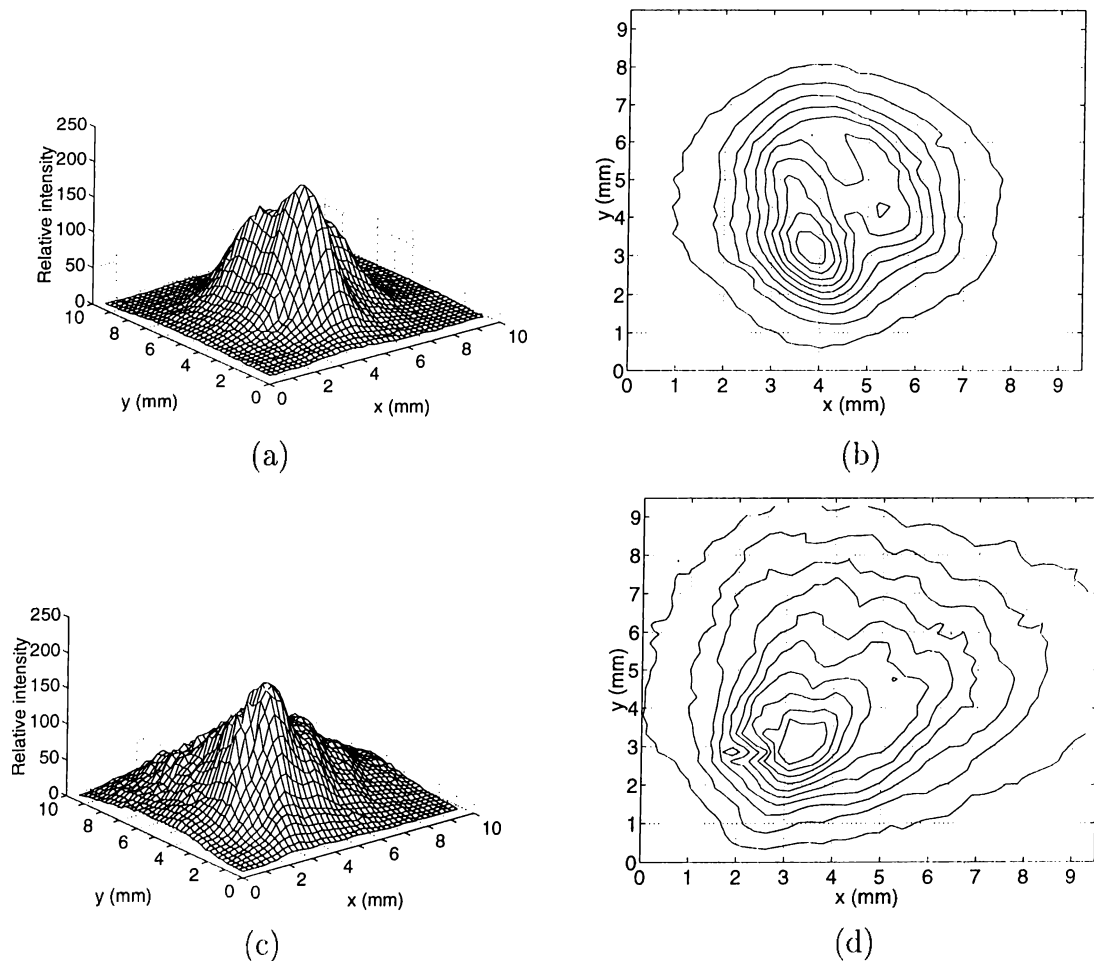


Figure 4.39: Signal profiles of (a) 3-D plot, (b) contour plot at 30 cm away from the plane-parallel double-pass OPO; (c) 3-D plot, (d) contour plot at 70 cm away from the plane-parallel double-pass OPO.

In the second method, by focusing the signal beam with a lens, we measured the diameter of the signal beam just in the focal plane. The ratio of the diameter to the focal length of the lens gives the full angle divergence of the beam. By this method, we measured the divergence as 3.2 mrad.

The experimental results show that the low energy OPO's constructed and characterized in the second experiment set (see section 4.2.3), and the high energy OPO's in the third experiment set (see section 4.2.4) meet the requirements of range finding and target designation applications.

Chapter 5

Simulations of OPO Experiments

While modeling OPO's numerically, many physical effects should be handled such as spatial beam profiles, strong energy exchange between the beams, diffraction, absorption, walkoff, and for pulsed OPO's temporal profiles of the beams.

A pulsed plane-wave OPO model for nanosecond OPO's was developed by Brosnan *et al.* in 1979 [18]. In this model, the pump depletion is neglected. Later in 1994, Terry *et al.* [36] developed an OPO model by considering optical cavity modes, but under low pump depletion assumption as in the previous model. Therefore these models can only predict threshold energies.

In 1995, Smith *et al.* [38] developed a numerical model of nanosecond OPO's. In this model, they take into account most of the physical effects of the OPO operation, such as diffraction, pump depletion, spatial and temporal beam profiles, phase velocity mismatch, and linear absorption. In the model, they assume that the nonlinear crystal is uniaxial. Therefore, if the direction of propagation is in z direction, and the optic axis of the crystal lies in the $x - z$ plane, then x -polarized (extraordinary) light walks off in the x -direction, and y polarized (ordinary) light does not walk off. This condition is also valid for biaxial crystals if the direction of propagation is along one of the principal planes. In the model, only the walkoff in the x direction is handled. The model predicts the threshold energy, and the conversion efficiency of the OPO's, and the spatial and temporal profiles of the signal beam, and it shows agreement with the experimental results.

Other than the OPO models, the computational methods for simulating second order nonlinear interactions such as SHG [78], [79], [80] or DFG [81], [82] have been developed [83], [84]. These models deal with the simulations of the evolution of fields with transverse variations in a second order nonlinear medium.

In these models either the beams are decomposed into plane wave components (Fourier space method) or coupled mode equations for each transverse position are solved independently.

In this chapter, the coupled mode equations are derived from the driven wave equation by including transverse variations of the fields. These coupled mode equations are solved at each transverse position by finite difference methods. OPO operation during the nanosecond long pulses are modeled by discretizing the time in terms of the cavity round trip time of the OPO's.

This chapter describes how we model the nanosecond OPO's, and presents the numerical method. Finally, the simulation results are compared with the experimental results.

5.1 Model

The operation of the OPO's is modeled for each pump pulse. The temporal profiles of the pump pulses are assumed to be Gaussian which is a suitable approximation for the pulses generated by Q-switched lasers. We consider a total time period where the pump pulse power decreases to 10^{-4} times its peak value, and this time interval is discretized by the cavity round trip times of the OPO's. Figure 5.1 presents a simple sketch of the discretization of the pump pulses where Δt denotes for the cavity round trip time.

Given the energy of a pump pulse and its temporal profile, the power values at each time point are computed. These power values are used to extract the

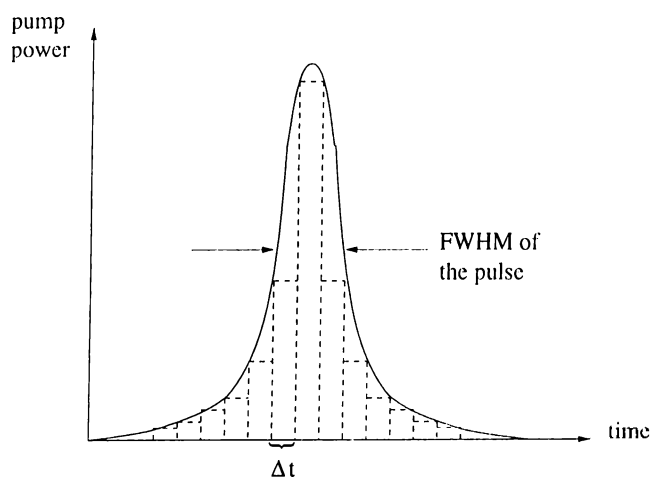


Figure 5.1: A simple sketch of the discretization of a pump pulse. The discretization step (Δt) denotes for the cavity round trip time.

intensity profiles of the pump pulse at the corresponding time points. In the experiments, we capture the pump profiles by a beam analyzer. We scale these real profiles with the computed pump power values. Therefore, the pump intensity profiles at each time point are obtained.

For each pulse, we start OPO operation with the initial pump intensity profile, and pick a signal profile with a power value of the parametric fluorescence. Initial idler intensity is zero. As these slices of three beams propagate in the nonlinear crystal, the pump gets depleted, the signal gets amplified, and some idler is generated. Since idler is totally absorbed in the OPO mirrors, at each time point, interaction starts with zero idler intensity. During the oscillation period, generated signal is partially taken out of the cavity and partially returned back. Initially, the introduced signal power from parametric fluorescence before the interaction exceeds the power of the back reflected signal. This means that gain cannot overcome loss, in other words the OPO is under threshold. For several round trips this condition may continue so in the model during this time, no signal is coupled out of the cavity, the pump is not depleted, and the interaction of the next round trip starts with the next pump profile and a corresponding signal profile by parametric fluorescence. This situation continues until the gain overcomes the loss.

In the experiments, two different cavities (single-pass or double-pass) are constructed. Therefore, we modeled each OPO separately. In the single-pass OPO cavities, the signal resonates in the cavity while the depleted pump is removed away at each round trip (see Figure 5.2). However, in the double-pass OPO's, the depleted pump is reflected back to the crystal, and this depleted pump and the returned signal interacts (see Figure 5.3). During the evolution in the nonlinear crystal, diffraction is handled, and both the phases and the amplitudes of the

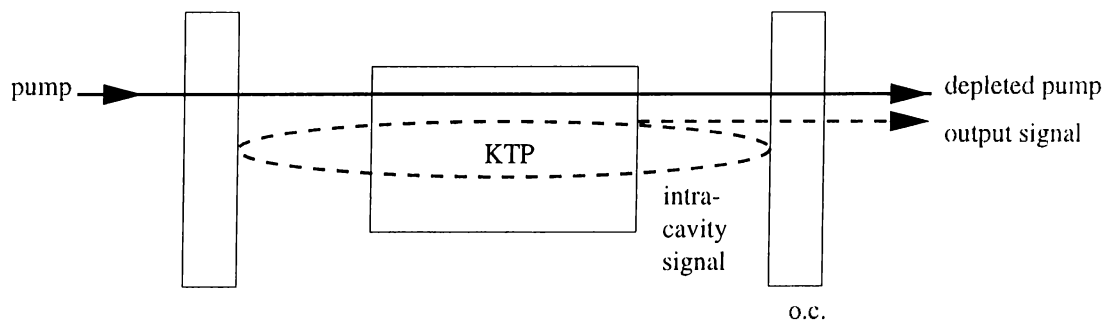


Figure 5.2: Optical parametric oscillation in a single-pass OPO cavity. Signal resonates in the cavity, while the depleted pump is taken out.

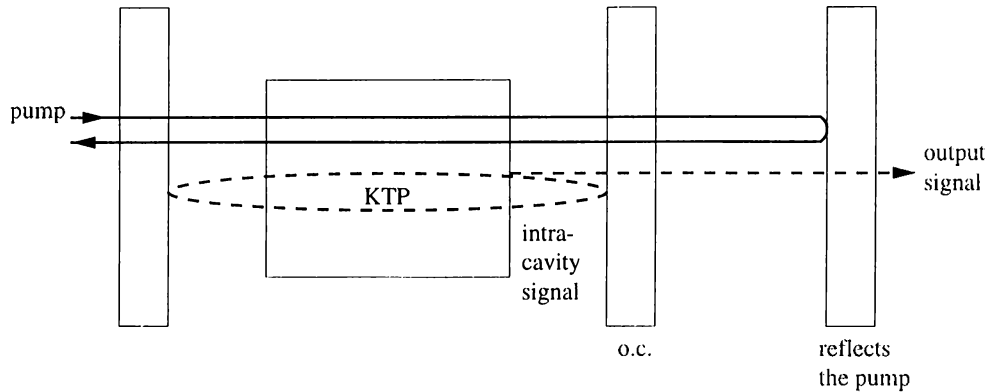


Figure 5.3: Optical parametric oscillation in a double-pass OPO cavity. Signal resonates in the cavity, the depleted pump is reflected back to the crystal, and makes a second pass.

fields are calculated by separating the real and imaginary parts of the fields. As an important remark, we consider the absorption of the KTP crystal at $3.3 \mu\text{m}$, which is the wavelength of the idler.

In the model all relevant parameters (either measured or computed) are listed in Table 5.1.

Parameters		Values	Units
Wavelengths of	signal, λ_1	1571	nm
	idler, λ_2	3297	
	pump, λ_3	1064	
Refractive indices of	signal, n_1	1.73635	
	idler, n_2	1.77102	
	pump, n_3	1.74754	
Effective nonlinear coefficient	d_e	3.6	pm/V
Crystal length		22.4	mm
Cavity length		25.0	mm
Pump pulse duration at FWHM		7-15	ns
Absorption coefficients of	signal, α_1	0	cm^{-1}
	idler, α_2	0.45	
	pump, α_3	0	
Useless loss that signal experiences	R_L	4%	

Table 5.1: Values of the physical parameters used in the model.

5.2 Analysis of the Coupled Mode Equations

In Chapter 2, the coupled mode equations (Equations (2.21)–(2.22)) are presented for plane waves. However, while modeling practical experiments, it is inadequate to accept the beams as plane waves. The beams have transverse variations, so x and y dependence of the beams must be considered.

In the driven wave equation

$$\nabla^2 \mathbf{E} - \frac{n^2}{c^2} \frac{\partial^2}{\partial t^2} \mathbf{E} = \mu_0 \frac{\partial^2}{\partial t^2} \mathbf{P}^{(2)} \quad (5.1)$$

with z -direction as the direction of propagation, the Laplacian (∇^2) can be expressed as

$$\nabla^2 = \frac{\partial^2}{\partial z^2} + \nabla_T^2 \quad (5.2)$$

where ∇_T^2 is the transverse Laplacian. In rectangular coordinates, the transverse Laplacian is

$$\nabla_T^2 = \frac{\partial^2}{\partial x^2} + \frac{\partial^2}{\partial y^2}. \quad (5.3)$$

Therefore, the coupled mode equations become

$$\frac{\partial}{\partial z} E_1 = -j \frac{d_e \omega_1}{n_1 c} E_3 E_2^* - \frac{j}{2k_1} \left[\frac{\partial^2}{\partial x^2} E_1 + \frac{\partial^2}{\partial y^2} E_1 \right] \quad (5.4)$$

$$\frac{\partial}{\partial z} E_2 = -j \frac{d_e \omega_2}{n_2 c} E_3 E_1^* - \frac{j}{2k_2} \left[\frac{\partial^2}{\partial x^2} E_2 + \frac{\partial^2}{\partial y^2} E_2 \right] - \alpha_2 E_2 \quad (5.5)$$

$$\frac{\partial}{\partial z} E_3 = -j \frac{d_e \omega_3}{n_3 c} E_1 E_2 - \frac{j}{2k_3} \left[\frac{\partial^2}{\partial x^2} E_3 + \frac{\partial^2}{\partial y^2} E_3 \right] \quad (5.6)$$

In Equation (5.5), $-\alpha_2 E_2$ term represents the idler absorption in the crystal. Since at the idler wavelength (3.3 μm) of the experiments, KTP has absorptions [36]. Also, when d_e and α_2 vanish, one can see that these coupled mode equations turn into the paraxial Helmholtz equations.

Equations (5.4)–(5.6) are in the form of partial differential equations (PDE's), and the problem of their solutions is an initial value problem. Finite difference techniques is one of the methods solving for such problems numerically [85].

In order to solve Equations (5.4)–(5.6), the fields (E_i 's) are separated into real and imaginary parts as

$$E_i = A_i + jB_i \quad i = 1, 2, 3 \quad (5.7)$$

and the following six equations are obtained:

$$\frac{\partial}{\partial z} A_1 = -\frac{d_e \omega_1}{n_1 c} (A_3 B_2 - B_3 A_2) + \frac{1}{2k_1} \left[\frac{\partial^2}{\partial x^2} B_1 + \frac{\partial^2}{\partial y^2} B_1 \right] \quad (5.8)$$

$$\frac{\partial}{\partial z} B_1 = -\frac{d_e \omega_1}{n_1 c} (A_3 A_2 + B_3 B_2) - \frac{1}{2k_1} \left[\frac{\partial^2}{\partial x^2} A_1 + \frac{\partial^2}{\partial y^2} A_1 \right] \quad (5.9)$$

$$\frac{\partial}{\partial z} A_2 = -\frac{d_e \omega_2}{n_2 c} (B_1 A_3 - B_3 A_1) - \alpha_2 A_2 + \frac{1}{2k_2} \left[\frac{\partial^2}{\partial x^2} B_2 + \frac{\partial^2}{\partial y^2} B_2 \right] \quad (5.10)$$

$$\frac{\partial}{\partial z} B_2 = -\frac{d_e \omega_2}{n_2 c} (A_1 A_3 + B_3 B_1) - \alpha_2 B_2 - \frac{1}{2k_2} \left[\frac{\partial^2}{\partial x^2} A_2 + \frac{\partial^2}{\partial y^2} A_2 \right] \quad (5.11)$$

$$\frac{\partial}{\partial z} A_3 = -\frac{d_e \omega_3}{n_3 c} (-B_1 A_2 - A_1 B_2) + \frac{1}{2k_3} \left[\frac{\partial^2}{\partial x^2} B_3 + \frac{\partial^2}{\partial y^2} B_3 \right] \quad (5.12)$$

$$\frac{\partial}{\partial z} B_3 = -\frac{d_e \omega_3}{n_3 c} (A_1 A_2 - B_1 B_2) - \frac{1}{2k_3} \left[\frac{\partial^2}{\partial x^2} A_3 + \frac{\partial^2}{\partial y^2} A_3 \right]. \quad (5.13)$$

The stability is an important consideration while solving initial value PDE's with explicit methods. If a numerical method introduces errors which rapidly overcome the desired solution and cause totally unrelated results, then this method is unstable. Before solving these equations, the stability of the equations for the chosen finite differencing type (such as forward differencing, backward differencing or central differencing) should be considered. In this case, the stability analysis is performed by using the von Neumann Stability analysis (or Fourier method) [85], [86].

While determining stability of the Equations (5.8)-(5.13), one can consider the PDE's without the added nonlinear terms. Therefore the equations turn into the form of a two dimensional flux-conservative equation such as

$$\frac{\partial}{\partial z} u = -c \left[\frac{\partial^2}{\partial x^2} u + \frac{\partial^2}{\partial y^2} u \right] \quad (5.14)$$

where c is any constant. In the case of difference equations with constant coefficients, the eigenmodes of the solutions have the form:

$$u_{l,m}^n = \epsilon^n e^{jkl\Delta x} e^{jkm\Delta y} \quad (5.15)$$

where k is real spatial wave number and can have any value, and $u_{l,m}^n$ indicates the value of $u(x_l, y_m, z_n)$ at discrete points of

$$x_l = l\Delta x$$

$$y_m = m\Delta y \quad (5.16)$$

$$z_n = n\Delta z$$

with l, m, n are integers, and $\Delta x, \Delta y,$ and Δz are grid spacings. In the evolution of these equations a single eigenmode is the successive integer powers of ϵ . If for some k ,

$$|\epsilon(k)| > 1 \quad (5.17)$$

then the equations are unstable. In the unstable case, at least one exponentially growing mode exists. Here, ϵ is called the amplification factor.

In the Equations (5.8)–(5.13), differential terms are coupled two by two. Therefore these terms can be expressed in a matrix form as

$$\frac{\partial}{\partial z} \begin{bmatrix} A_i \\ B_i \end{bmatrix} = \frac{1}{2k_i} \left(\frac{\partial^2}{\partial x^2} \begin{bmatrix} B_i \\ -A_i \end{bmatrix} + \frac{\partial^2}{\partial y^2} \begin{bmatrix} B_i \\ -A_i \end{bmatrix} \right) \quad i = 1, 2, 3 \quad (5.18)$$

then for the stability analysis, an eigenmode of

$$\begin{bmatrix} A_{i,m}^n \\ B_{i,m}^n \end{bmatrix} = \epsilon^n e^{jk_x l \Delta x} e^{jk_y m \Delta y} \begin{bmatrix} A_0 \\ B_0 \end{bmatrix} \quad i = 1, 2, 3 \quad (5.19)$$

is used where k_x and k_y are real spatial wavenumbers. This eigenmode solution is used in the discretized PDE's that are formed by central differencing in both $x, y,$ and z directions

$$\frac{A_{i,m}^{n+1} - A_{i,m}^{n-1}}{2\Delta z} = \frac{1}{2k_i} \left(\frac{B_{i+1,m}^n - 2B_{i,m}^n + B_{i-1,m}^n}{\Delta x^2} + \frac{B_{i+1,m}^n - 2B_{i,m}^n + B_{i-1,m}^n}{\Delta y^2} \right) \quad (5.20)$$

$$\frac{B_{i,m}^{n+1} - B_{i,m}^{n-1}}{2\Delta z} = -\frac{1}{2k_i} \left(\frac{A_{i+1,m}^n - 2A_{i,m}^n + A_{i-1,m}^n}{\Delta x^2} + \frac{A_{i+1,m}^n - 2A_{i,m}^n + A_{i-1,m}^n}{\Delta y^2} \right) \quad (5.21)$$

for $i = 1, 2$ and 3 . For simplicity, one can choose the grid spacings in the x and y directions equal to each other:

$$\Delta x = \Delta y = \Delta \quad (5.22)$$

After inserting the eigensolution (Equation (5.19)) into Equations (5.20) and (5.21), the following equation is obtained:

$$\begin{bmatrix} 1/\epsilon - \epsilon & \frac{-2\Delta z}{k_i\Delta^2}(\sin^2(\frac{k_x\Delta}{2}) + \sin^2(\frac{k_y\Delta}{2})) \\ \frac{2\Delta z}{k_i\Delta^2}(\sin^2(\frac{k_x\Delta}{2}) + \sin^2(\frac{k_y\Delta}{2})) & 1/\epsilon - \epsilon \end{bmatrix} \begin{bmatrix} A_0 \\ B_0 \end{bmatrix} = \begin{bmatrix} 0 \\ 0 \end{bmatrix} \quad (5.23)$$

There is a solution for this equation if the determinant of the matrix is zero. In this case, we obtain four distinct roots of ϵ

$$\begin{aligned} \epsilon = & \pm j \frac{\Delta z}{k_i\Delta^2}(\sin^2(\frac{k_y\Delta}{2}) + \sin^2(\frac{k_x\Delta}{2})) \\ & \pm \sqrt{1 - (\frac{\Delta z}{k_i\Delta^2}(\sin^2(\frac{k_y\Delta}{2}) + \sin^2(\frac{k_x\Delta}{2})))^2}. \end{aligned} \quad (5.24)$$

For all k_x and k_y , $|\epsilon| = 1$ only if

$$\Delta z \leq k_i\Delta^2. \quad (5.25)$$

Therefore, the finite differencing is stable if appropriate grid spacings satisfying this inequality are chosen. This result also indicates that there is no amplitude dissipation introduced by the numerical method because of the unity amplitude of the eigensolutions.

5.3 Simulation Results

For each experimental setup, we simulated the experiments and presented the simulation results in comparison with the experimental data. In the plots, the filled circles represent the experimental data, and the hollow circles represent the simulation results.

5.3.1 Simulations of the Low Energy OPO's

In the simulations, the results usually fit the experimental data as the pump energy values increase beyond the threshold value (see Figure 5.4). Figure 5.4 shows the signal energy values with respect to the pump energy data of a single-pass OPO with $R = 80\%$ o.c., both presenting the experimental data (filled circles) and the simulation results (hollow circles).

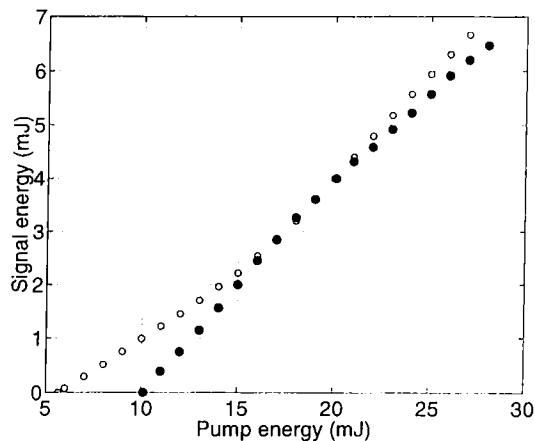


Figure 5.4: Signal energy vs. pump energy data of the single-pass OPO with $R = 80\%$ o.c. The filled circles represent the experimental data, and the hollow circles represent the simulation results.

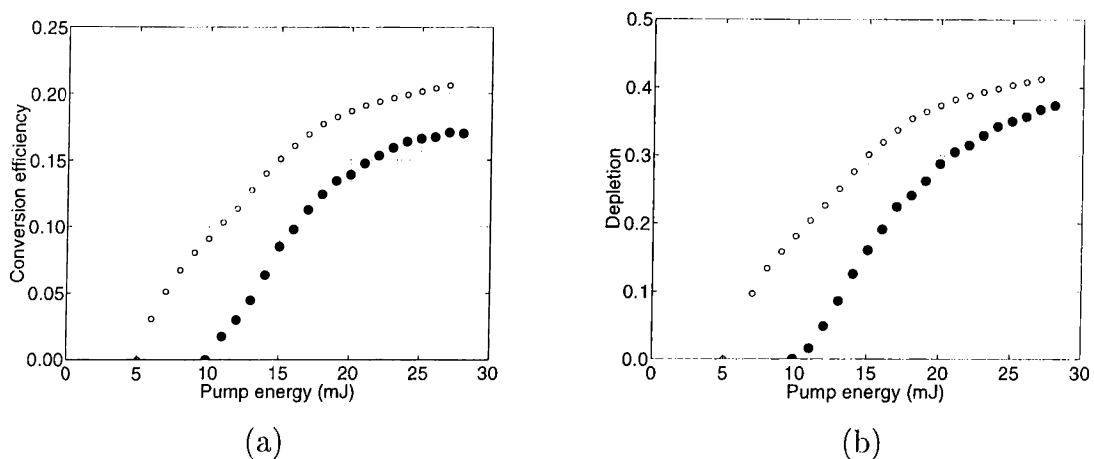


Figure 5.5: Simulation and experimental results of the (a) conversion efficiency vs. pump energy data of the single-pass OPO with $R = 90\%$ o.c., (b) pump depletion vs. pump energy data of the single-pass OPO with $R = 90\%$ o.c.

Simulations are performed for each o.c., and maximum deviation of the simulation results from the experimental results is obtained with the $R = 90\%$ o.c. of a single-pass OPO configuration (see Figure 5.5). In this case, the maximum conversion efficiency and the pump depletion values are approximately 15% more than the experimental results.

Similar results are obtained in double-pass OPO simulations. Figure 5.6 presents the output signal energy vs. input pump energy data of the double-pass OPO employing the $R = 80\%$ o.c. In this case, the corresponding conversion efficiency plot is shown in Figure 5.7.

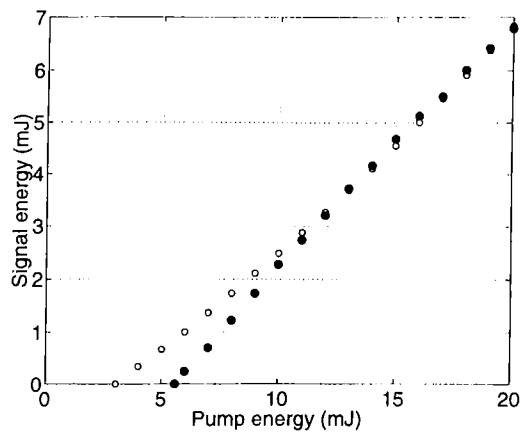


Figure 5.6: Simulation and experimental results the signal energy vs. pump energy data of the double-pass OPO with $R = 80\%$ o.c.

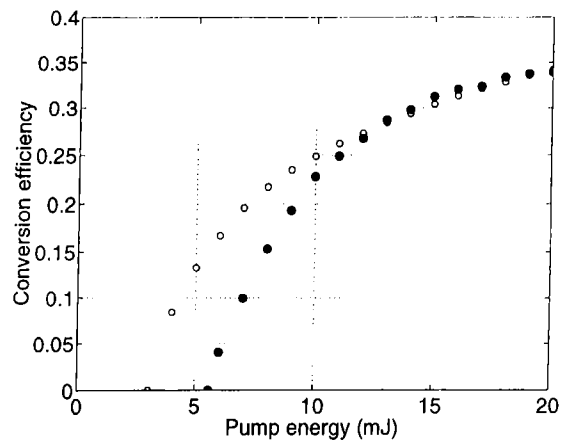


Figure 5.7: Simulation and experimental results of the conversion efficiency vs. pump energy data of the double-pass OPO with $R = 80\%$ o.c.

The simulations and experimental results of the time traces of the pump, depleted pump and signal pulses of a single-pass OPO with $R = 70\%$ o.c. are presented (see Figure 5.8). As seen in the figure, the peak of the signal pulse is approximately 2 ns delayed from the peak of the pump pulse whereas an approximately equal delay was observed in the experiments. The FWHM of the signal pulse of the simulations (5.5 ns) is slightly less than the experimental results (6.8 ns).

In the experiments, by changing the cavity length, the change in the conversion efficiency was observed. The simulations of such experiments are presented in Figure 5.9, where the cavity lengths are 2.5 cm, 3 cm, 5 cm, or 7 cm. These OPO's are double-pass OPO's, each one employing an o.c. of $R = 70\%$. In the

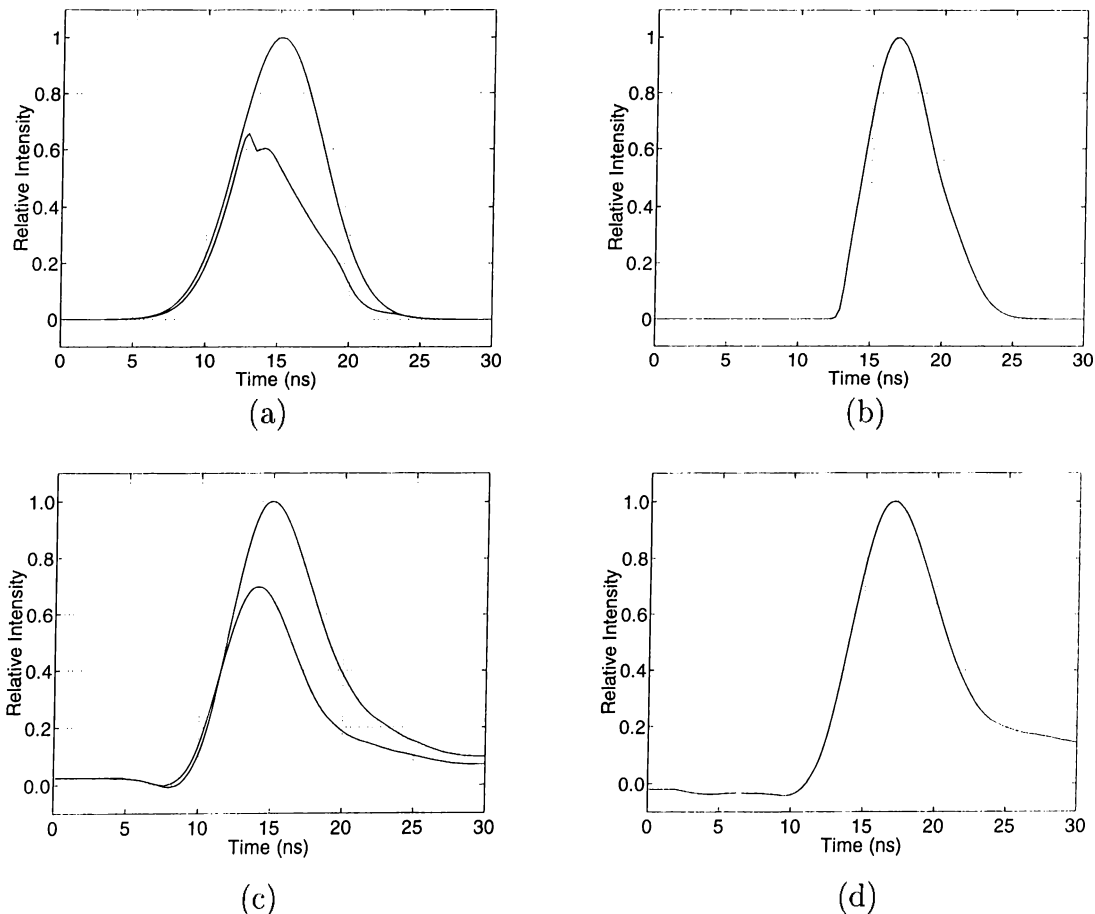


Figure 5.8: Simulations of the time traces of (a) pump and the depleted pump, (b) signal pulse, and experimental measurements of the time traces of (a) pump and the depleted pump, (b) signal pulse of the single-pass OPO with $R = 70\%$ o.c.

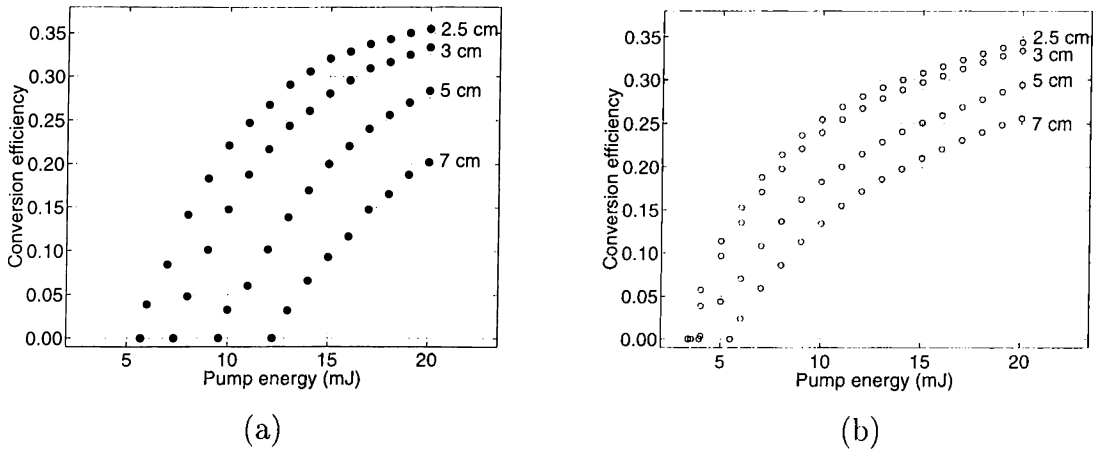


Figure 5.9: Conversion efficiency plots with cavity lengths of 2.5 cm, 3 cm, 5 cm, and 7 cm. These OPO's are double-pass, and employ o.c.'s of $R = 70\%$. (a) Experimental results, (b) simulation results.

simulations, as the cavity length decreases, the results approach to the experimental results. For example, when the cavity length is 2.5 cm, the maximum conversion efficiency obtained in the experiments and in the simulations are 35% and 34%, respectively. However if the cavity length is increased to 7 cm, the corresponding efficiency values are 20% and 26%. A similar pattern is also observed in single-pass OPO cavities.

In the second experimental set, where the OPO's are pumped up to 15 mJ in the double-pass configuration, and up to 20 mJ in the single-pass configuration, similar results are obtained. Figure 5.10 presents the conversion efficiency v.s. pump energy data with $R = 70\%$ o.c. In this case, the model fits the experiments beyond the threshold.

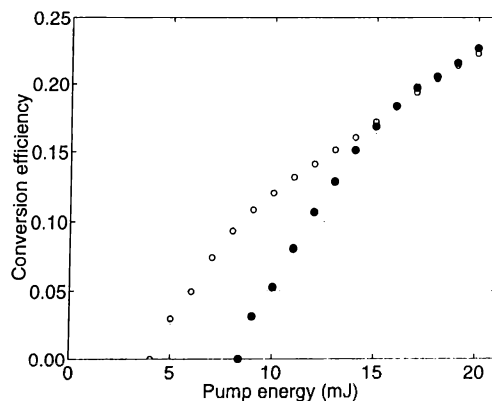


Figure 5.10: Simulation and experimental results of the conversion efficiency vs. pump energy data of the single-pass OPO with $R = 70\%$ o.c. obtained in the second experiment set.

5.3.2 Simulations of the High Energy OPO's

High energy OPO's with single-pass and double-pass cavity configurations are modeled as the low energy OPO's. In this case, the simulation results are also in qualitative agreement with the experimental results.

In the experiments, a double-pass OPO with $R = 60\%$ o.c. was constructed, and maximum 38.5% conversion efficiency was obtained. In Figure 5.11, these results are presented with the simulation results. The threshold pump energy of the simulations is approximately 10 mJ, while this value was measured as 23 mJ in the experiments. However, there is a qualitative agreement.

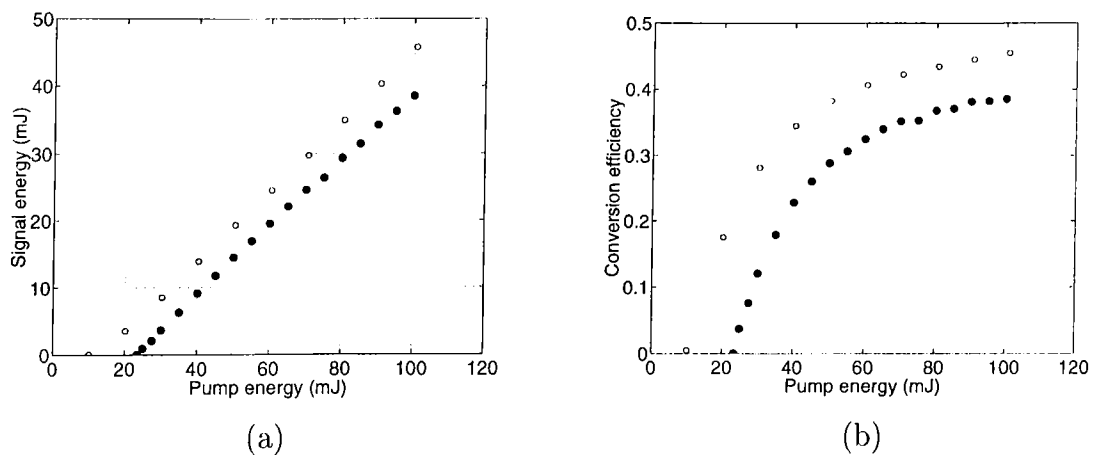


Figure 5.11: Simulation and experimental results of the (a) signal energy vs. pump energy, and (b) conversion efficiency vs. pump energy data of the double-pass OPO with $R = 60\%$ o.c.

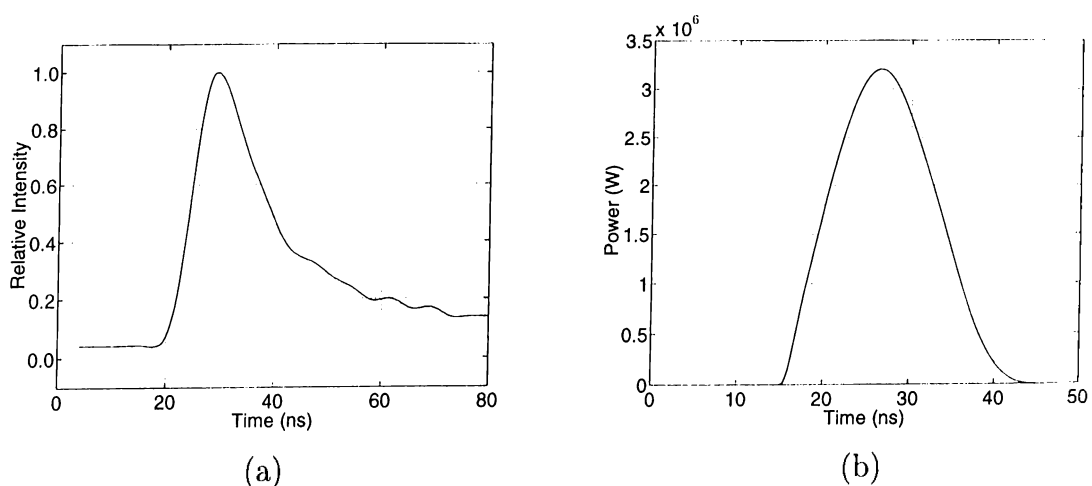


Figure 5.12: (a) Experimental measurement of the time trace of the signal pulse, and (b) simulation of the time trace of the signal pulse of the double-pass OPO with $R = 60\%$ o.c.

With the double-pass cavity configuration and $R = 60\%$ o.c., the signal pulse duration at FWHM was measured as 15 ns, while the corresponding value is 14 ns in the simulations (see Figure 5.12).

5.4 Discussions

As a conclusion, a numerical OPO model including temporal, and spatial beam profiles, pump depletion, diffraction, and absorption of the nonlinear crystal is developed. The measured pump intensity profiles, energy values, and temporal profiles are used as inputs to the model. The results of this model is presented in comparison with the experimental data. The numerical model is in qualitative agreement with the experimental results.

The simulation results are close to the experimental data when the OPO's are pumped beyond the threshold energy. However the model cannot predict the threshold energy values. This deviation may depend on inappropriate modeling of the initial parametric fluorescence.

In the model, absorption of KTP at $3.3 \mu\text{m}$ wavelength is handled by adding a distributive loss term to the coupled mode equations [9]. However, the effective nonlinear coefficient (d_e) value may differ for each polarization density due to the loss in the nonlinear crystal. In the model, we ignored such an effect and assumed a fixed d_e value.

As another assumption, the wavelength of the pump and the signal beams are assumed to be fixed constants, so the spectral linewidth of these beams are ignored.

In the model, each pump pulse duration is discretized by the cavity round trip times. As an improvement of the model, this discretization can be increased by decreasing the time periods shorter than the cavity round trip times.

Chapter 6

Conclusions

In this thesis, we constructed and characterized KTP OPO's generating eye-safe radiation pumped at either low energies (less than 30 mJ) or at high energies (at 100 mJ). The OPO's were pumped by a Q-switched Nd:YAG laser generating 7 ns or 15 ns long pulses at 1064 nm. These OPO's generate eye-safe laser light at 1.57 μm .

In the experiments, OPO cavities with shortest possible lengths have been constructed. In nanosecond OPO's, by decreasing the cavity length the number of signal round trips increases. This leads an increase in the conversion efficiency of the OPO's. The cavities are constructed in two different configurations (single-pass or double-pass). Double-passing the pump beam through the OPO cavity provides higher efficiency and lower threshold energy when compared to the single-pass OPO's.

In the low energy OPO experiments, 4.1 mJ threshold energy and 35.1% conversion efficiency were achieved when the OPO was pumped at 15 mJ. In the high energy OPO experiments, the threshold energy was 23.4 mJ, and the conversion efficiency was 38.5% when the OPO was pumped at 100 mJ. The signal durations were 6.7 ns and 15.4 ns for low and high energy applications, respectively. In the low energy OPO's, the wavelength of the signal was at 1571 nm. In the high energy OPO's, because of a slight shift of the input pump and the OPO cavity, a signal beam at 1573 nm was obtained. The divergence of these OPO's were approximately 4 mrad for low energy OPO's, and 3 mrad for high energy OPO's. With all these properties, these OPO's can be used for practical applications.

The history of the experimental work on nanosecond OPO's employing various crystals have also been investigated. In the literature, eye-safe OPO experiments

employing KTP crystals were reported by Marshall *et al.* between 1991–1993 [27], [28], [29]. They obtained 47% conversion efficiency by using a flux grown KTP crystal, when the OPO was pumped at 20 mJ.

Finally, a model of the experiments by using finite difference techniques is provided. In this model, we take into account the temporal and spatial profiles of the beams. The model also includes pump depletion, diffraction, and absorption in the KTP crystal. The simulation results are in qualitative agreement with the experimental results.

As a future goal, nanosecond OPO models employing Fourier space methods can be developed. By this method, the coupled mode equations which are in the form of PDE's are transformed into ordinary differential equations. The ordinary differential equations can be solved by some other numerical methods, such as Runge-Kutta methods. An improved model including other physical effects, such as spectral properties, modeling the effective nonlinear coefficient in a lossy medium can also be constructed.

References

- [1] J. A. Giordmaine and R. C. Miller “Tunable coherent parametric oscillation in LiNbO_3 at optical frequencies,” *Physical Review Letters*, vol. 14, pp. 973–976, 1965.
- [2] K. Sentrayan, A. Michael, U. N. Singh, and V. S. Kushawaha “Effect of buffer gas on the generation of eye-safe $1.54 \mu\text{m}$ radiation using the stimulated Raman scattering technique in CH_4 ,” *Optics and Laser Technology*, vol. 29, pp. 275–279, 1997.
- [3] F. A. L’esperance, ed. *Ophthalmic Lasers*. C. V. Mosby, 1989.
- [4] R. W. Boyd, ed. *Nonlinear Optics*. Academic Press, Inc., 1992.
- [5] G. B. Thomas and R. L. Finney, eds. *Calculus and Analytic Geometry*. Addison-Wesley Publishing Company, Inc., 1992.
- [6] C. L. Tang and L. K. Cheng, eds. *Fundamentals of Optical Parametric Processes and Oscillators*. Harwood Academic Publishers, 1995.
- [7] R. A. Baumgartner and R. L. Byer “Optical parametric amplification,” *IEEE Journal of Quantum Electronics*, vol. 15, pp. 432–444, 1979.
- [8] M. Abramowitz and I. A. Stegun, eds. *Handbook of Mathematical functions with formulas, graphs, and mathematical tables*. Dover, 1965.
- [9] H. Rabin and C. L. Tang, eds. *Treatise in Quantum Electronics*. Academic, New York, 1973.
- [10] C. L. Tang, W. R. Bosenberg, T. Ukachi, R. J. Lane, and L. K. Cheng “Optical parametric oscillators,” *Proceedings of IEEE*, vol. 80, pp. 365–373, 1992.

- [11] L. E. Myers and W. R. Bosenberg “Quasi-phase-matched optical parametric oscillators in bulk periodically poled LiNbO₃,” *Journal of Optical Society of America B*, vol. 12, pp. 2102–2116, 1995.
- [12] L. E. Myers, R. C. Eckardt, M. M. Fejer, R. L. Byer, and W. R. Bosenberg “Multigrating quasi-phase-matched optical parametric oscillators in periodically poled LiNbO₃,” *Optics Letters*, vol. 21, pp. 591–593, 1996.
- [13] L. E. Myers and W. R. Bosenberg “Periodically poled Lithium Niobate and quasi-phase-matched optical parametric oscillators,” *IEEE Journal of Quantum Electronics*, vol. 33, pp. 1663–1672, 1997.
- [14] J. E. Bjorkholm “Efficient optical parametric oscillation using doubly and singly resonant cavities,” *Applied Physics Letters*, vol. 13, pp. 53–56, 1968.
- [15] S. E. Harris “Tunable optical parametric oscillators,” *Proceedings of IEEE*, vol. 57, pp. 2096–2113, 1969.
- [16] R. W. Wallace “Stable, efficient optical parametric oscillators pumped with doubled Nd:YAG,” *Applied Physics Letters*, vol. 17, pp. 497–499, 1970.
- [17] R. L. Herbst, R. N. Fleming, and R. L. Byer “A 1.4-4 μm high energy angle-tuned LiNbO₃ parametric oscillator,” *Applied Physics Letters*, vol. 25, pp. 520–522, 1974.
- [18] S. J. Brosnan and R. L. Byer “Optical parametric oscillation threshold and linewidth studies,” *IEEE Journal of Quantum Electronics*, vol. 15, pp. 415–431, 1979.
- [19] R. Lavi, A. Englander, and R. Lallouz “Highly efficient low-threshold tunable all-solid-state intracavity optical parametric oscillator in the mid infrared,” *Optics Letters*, vol. 21, pp. 800–802, 1996.
- [20] K. Kato “High-efficiency high-power parametric oscillation in KNbO₃,” *IEEE Journal of Quantum Electronics*, vol. 18, pp. 451–452, 1982.
- [21] R. Urschel, A. Fix, R. Wallenstein, D. Rytz, and B. Zysstet “Generation of tunable narrow-band midinfrared radiation in a type-I potassium niobate optical parametric oscillator,” *Journal of Optical Society of America B*, vol. 12, pp. 726–730, 1995.

- [22] W. R. Bosenberg and R. H. Jarman “Type-II phase-matched KNbO₃ optical parametric oscillator,” *Optics Letters*, vol. 18, pp. 1323–1325, 1993.
- [23] P. Rambaldi, M. Douard, B. Vezin, and D. Rytz “Broadly tunable KNbO₃ OPOs pumped by Ti:sapphire lasers,” *Optics Communications*, vol. 142, pp. 262–264, 1997.
- [24] R. L. Burnham, R. A. Stolzenberger, and A. Pinto “Infrared optical parametric oscillator in potassium titanyl phosphate,” *IEEE Photonics Technology Letters*, vol. 1, pp. 27–28, 1989.
- [25] J. T. Lin and J. L. Montgomery “Generation of tunable mid-IR (1.8–2.4 μm) laser from optical parametric oscillation in KTP,” *Optics Communications*, vol. 75, pp. 315–320, 1990.
- [26] K. Kato “Parametric oscillation at 3.2 μm in KTP pumped at 1.064 μm ,” *IEEE Journal of Quantum Electronics*, vol. 27, pp. 1137–1140, 1991.
- [27] L. R. Marshall, J. Kasinski, A. D. Hays, and R. L. Burnham “Efficient optical parametric oscillator at 1.6 μm ,” *Optics Letters*, vol. 16, pp. 681–683, 1991.
- [28] L. R. Marshall, J. Kasinski, and R. L. Burnham “Diode-pumped eye-safe laser source exceeding 1% efficiency,” *Optics Letters*, vol. 16, pp. 1680–1682, 1991.
- [29] L. R. Marshall and A. Kaz “Eye-safe output from noncritically phase-matched parametric oscillators,” *Journal of Optical Society of America B*, vol. 10, pp. 1730–1736, 1993.
- [30] T. D. Raymond, W. J. Alford, A. V. Smith, and M. S. Bowers “Frequency shifts in injection-seeded optical parametric oscillators with phase mismatch,” *Optics Letters*, vol. 19, pp. 1520–1522, 1994.
- [31] F. Huisken, M. Kaloudis, J. Marquez, Y. L. Chuzavkov, S. N. Orlov, Y. N. Polivanov, and V. V. Smirnov “Single-mode KTiOPO₄ optical parametric oscillator,” *Optics Letters*, vol. 20, pp. 2306–2308, 1995.
- [32] W. R. Bosenberg and D. R. Guyer “Single-frequency optical parametric oscillator,” *Applied Physics Letters*, vol. 61, pp. 387–389, 1992.

- [33] M. G. Jani, R. C. Powell, B. Jassemnejad, and R. Stolzenberger “Pump wavelength tuning of a near-infrared optical parametric oscillator,” *Applied Optics*, vol. 31, pp. 1998–2000, 1992.
- [34] M. G. Jani, J. T. Murray, R. R. Petrin, R. C. Powell, D. N. Loiacono, and G. M. Loiacono “Pump wavelength tuning of optical parametric oscillations and frequency mixing in KTiOAsO_4 ,” *Applied Physics Letters*, vol. 60, pp. 2327–2329, 1992.
- [35] H. H. Zenzie and P. F. Moulton “Tunable optical parametric oscillators pumped by Ti:sapphire lasers,” *Optics Letters*, vol. 19, pp. 963–965, 1994.
- [36] J. A. C. Terry, Y. Cui, Y. Yang, W. Sibbett, and M. H. Dunn “Low-threshold operation of an all-solid-state ktp optical parametric oscillator,” *Journal of Optical Society of America B*, vol. 11, pp. 758–769, 1994.
- [37] Y. Tang, C. F. Rae, C. Rahlff, and M. H. Dunn “Low threshold, high-efficiency, widely tunable infrared source from a KTP-based optical parametric oscillator,” *Journal of Optical Society of America B*, vol. 14, pp. 3442–3451, 1997.
- [38] A. V. Smith, W. J. Alford, T. D. Raymond, and M. S. Bowers “Comparison of a numerical model with measured performance of a seeded, nanosecond KTP optical parametric oscillator,” *Journal of Optical Society of America B*, vol. 12, pp. 2253–2267, 1995.
- [39] D. J. Armstrong, W. J. Alford, T. D. Raymond, A. V. Smith, and M. S. Bowers “Parametric amplification and oscillation with walkoff-compensating crystals,” *Journal of Optical Society of America B*, vol. 14, pp. 460–474, 1997.
- [40] W. R. Donaldson and C. L. Tang “Urea optical parametric oscillator,” *Applied Physics Letters*, vol. 44, pp. 25–27, 1984.
- [41] M. J. Rosker and C. L. Tang “Widely tunable optical parametric oscillator using urea,” *Journal of Optical Society of America B*, vol. 2, pp. 691–696, 1985.
- [42] M. J. Rosker, K. Cheng, and C. L. Tang “Practical urea optical parametric oscillator for tunable generation throughout the visible and near-infrared,” *IEEE Journal of Quantum Electronics*, vol. 21, pp. 1600–1606, 1985.

- [43] G. C. Catella, J. H. Bohn, and J. R. Luken “Tunable high-power urea optical parametric oscillator,” *IEEE Journal of Quantum Electronics*, vol. 24, 1988.
- [44] M. Ebrahimzadeh and M. H. Dunn “Optical parametric fluorescence and oscillation in urea using an excimer laser,” *Optics Communications*, vol. 69, pp. 161–165, 1988.
- [45] M. Ebrahimzadeh, M. H. Dunn, and F. Akerboom “Highly efficient visible urea optical parametric oscillator pumped by a XeCl excimer laser,” *Optics Letters*, vol. 14, pp. 560–562, 1989.
- [46] A. J. Henderson, M. Ebrahimzadeh, and M. H. Dunn “Characterization of urea optical parametric oscillators pumped by excimer lasers,” *Journal of Optical Society of America B*, vol. 7, pp. 1402–1410, 1990.
- [47] J. G. Haub, M. J. Johnson, B. J. Orr, and R. Wallenstein “Continuously tunable, injection-seeded β -barium borate optical parametric oscillator: Spectroscopic applications,” *Applied Physics Letters*, vol. 58, pp. 1718–1720, 1991.
- [48] J. G. Haub, M. J. Johnson, and B. J. Orr “Spectroscopic and nonlinear-optical applications of a tunable β -barium borate optical parametric oscillator,” *Journal of Optical Society of America B*, vol. 10, pp. 1765–1777, 1993.
- [49] Y. X. Fan, R. C. Eckardt, R. L. Byer, C. Chen, and A. D. Jiang “Barium borate optical parametric oscillator,” *IEEE Journal of Quantum Electronics*, vol. 25, pp. 1196–1199, 1989.
- [50] L. K. Cheng, W. R. Bosenberg, and C. L. Tang “Broadly tunable optical parametric oscillation in β -BaB₂O₄,” *Applied Physics Letters*, vol. 53, pp. 175–177, 1988.
- [51] Y. X. Fan, R. C. Eckardt, R. L. Byer, J. Nolting, and R. Wallenstein “Visible BaB₂O₄ optical parametric oscillator pumped at 355 nm by a single axial mode pulsed source,” *Applied Physics Letters*, vol. 53, pp. 2014–2016, 1988.
- [52] W. R. Bosenberg, L. K. Cheng, and C. L. Tang “Ultraviolet optical parametric oscillation in β -BaB₂O₄,” *Applied Physics Letters*, vol. 54, pp. 13–15, 1989.

- [53] W. R. Bosenberg, W. S. Pelouch, and C. L. Tang “High efficiency and narrow linewidth operation of a two crystal β -BaB₂O₄,” *Applied Physics Letters*, vol. 55, pp. 1953–1954, 1989.
- [54] W. R. Bosenberg and C. L. Tang “Type II phase matching in a β -barium borate optical parametric oscillator,” *Applied Physics Letters*, vol. 56, pp. 1819–1821, 1990.
- [55] H. Komine “Optical parametric oscillation in a beta-barium borate crystal pumped by an XeCl excimer laser,” *Optics Letters*, vol. 13, pp. 643–645, 1988.
- [56] M. Ebrahimzadeh, A. J. Henderson, and M. H. Dunn “An excimer-pumped β -BaB₂O₄ optical parametric oscillator tunable from 354 nm to 2.370 μ m,” *IEEE Journal of Quantum Electronics*, vol. 26, pp. 1241–1252, 1990.
- [57] Y. Wang, Z. Xu, D. Dneg, W. Zheng, X. Liu, B. Wu, and C. Chen “Highly efficient visible and infrared β -BaB₂O₄ optical parametric oscillator with pump reflection,” *Applied Physics Letters*, vol. 58, pp. 1461–1463, 1991.
- [58] E. A. Stappaerts, E. A. and H. Komine “High-power wavelength converters with feedback,” *Optics Letters*, vol. 19, pp. 563–565, 1994.
- [59] L. A. W. Gloster, Z. X. Jiang, and T. A. King “Characterization of an Nd:YAG pumped β -BaB₂O₄ optical parametric oscillator in collinear and noncollinear phase-matched configurations,” *IEEE Journal of Quantum Electronics*, vol. 30, pp. 2961–2969, 1994.
- [60] L. A. W. Gloster, I. T. McKinnie, and T. A. King “Noncollinear phase matching in a type I barium borate optical parametric oscillator,” *Optics Communications*, vol. 112, pp. 328–332, 1994.
- [61] S. Lee, S. Kim, D. Ko, J. Han, and J. Lee “High-efficiency and low-threshold operation of the pump reflection configuration in the noncollinear phase matching optical parametric oscillator,” *Optics Communications*, vol. 144, pp. 241–244, 1997.
- [62] S. Wu, G. A. Blake, Z. Sun, and J. Ling “Simple, high-performance type II β -BaB₂O₄ optical parametric oscillator,” *Applied Optics*, vol. 36, pp. 5898–5901, 1997.

- [63] K. Kato “Parametric oscillation in LiB_3O_5 pumped at $0.532 \mu\text{m}$,” *IEEE Journal of Quantum Electronics*, vol. 26, pp. 2043-2045, 1990.
- [64] Y. Wang, Z. Xu, D. Dneg, W. Zheng, B. Wu, and C. Chen “Visible optical parametric oscillation in LiB_3O_5 ,” *Applied Physics Letters*, vol. 59, pp. 531-533, 1991.
- [65] G. Robertson, A. Henderson, and M. Dunn “Attainment of high efficiencies in optical parametric oscillators,” *Optics Letters*, vol. 16, pp. 1584-1586, 1991.
- [66] G. Robertson, A. Henderson, and M. H. Dunn “Broadly tunable LiB_3O_5 optical parametric oscillator,” *Applied Physics Letters*, vol. 60, pp. 271-273, 1992.
- [67] M. Ebrahimzadeh, G. Robertson, and M. H. Dunn “Efficient ultraviolet LiB_3O_5 optical parametric oscillator,” *Optics Letters*, vol. 16, pp. 767-769, 1991.
- [68] Y. Tang, Y. Cui, and M. H. Dunn “Lithium triborate optical parametric oscillator pumped at 266 nm,” *Optics Letters*, vol. 17, pp. 192-194, 1992.
- [69] Y. Cui, D. E. Withers, C. F. Rae, C. J. Norrie, Y. Tang, B. D. Sinclair, W. Sibbett, and M. H. Dunn “Widely tunable all-solid-state OPO for the visible and near infrared,” *Optics Letters*, vol. 18, pp. 122-124, 1993.
- [70] Y. Cui, D. E. Withers, C. F. Rae, C. J. Norrie, Y. Tang, B. D. Sinclair, W. Sibbett, and M. H. Dunn “Widely tunable all-solid-state optical parametric oscillator for the visible and near infrared,” *Optics Letters*, vol. 18, pp. 122-124, 1993.
- [71] G. J. Hall and A. I. Ferguson “ LiB_3O_5 optical parametric oscillator pumped by a Q-switched frequency doubled all-solid-state laser,” *Optics Letters*, vol. 18, pp. 1511-1513, 1993.
- [72] T. Schröder, K. J. Boller, A. Fix, and R. Wallenstein “Spectral properties and numerical modelling of a critically phase matched nanosecond LiB_3O_5 optical parametric oscillator,” *Applied Physics B*, vol. 58, pp. 425-438, 1994.

- [73] R. C. Eckardt, Y. X. Fan, R. L. Byer, C. L. Marquardt, M. E. Storm, and L. Esterowitz “Broadly tunable infrared parametric oscillator using AgGaSe_2 ,” *Applied Physics Letters*, vol. 49, pp. 608–610, 1986.
- [74] J. Kirton “A 2.54 μm -pumped type II AgGaSe_2 mid-IR optical parametric oscillator,” *Optics Communications*, vol. 115, pp. 93–98, 1995.
- [75] T. H. Allik, S. Chandra, D. M. Rines, P. G. Schunemann, J. A. Hutchinson, and R. Utano “Tunable 7-12 μm optical parametric oscillator using a Cr,Er:YSGG laser to pump CdSe and ZnGeP_2 crystals,” *Optics Letters*, vol. 22, pp. 597–599, 1997.
- [76] D. A. Roberts “Simplified characterization of uniaxial and biaxial nonlinear optical crystals: A plea for standardization of nomenclature and conventions,” *IEEE Journal of Quantum Electronics*, vol. 28, pp. 2057–2074, 1992.
- [77] V. G. Dmitriev, G. G. Gurzadyan, and D. N. Nikogosyan, eds. *Handbook of Nonlinear Optical Crystals*. Springer-Verlag, Berlin, 1997.
- [78] S. Sheng and A. E. Siegman “Nonlinear-optical calculations using fast-transform methods: Second-harmonic generation with depletion and diffraction,” *Physical Review A*, vol. 21, pp. 599–606, 1980.
- [79] M. A. Dreger and J. K. McIver “Second-harmonic generation in a nonlinear, anisotropic medium with depletion and depletion,” *Journal of Optical Society of America B*, vol. 7, pp. 776–784, 1990.
- [80] P. Pliszka and P. P. Banerjee “Nonlinear transverse effects in second-harmonic generation,” *Journal of Optical Society of America B*, vol. 10, pp. 1810–1819, 1993.
- [81] M. Nieto-Vesperinas and G. Lera “Solution to non-linear optical mixing equations with depletion and diffraction: Difference-frequency generation,” *Optics Communications*, vol. 69, pp. 329–333, 1989.
- [82] T. Nishikawa and N. Uesugi “Transverse beam profile characteristics of traveling-wave parametric generation in KTiOPO_4 crystals,” *Optics Communications*, vol. 124, pp. 512–518, 1996.

- [83] G. Arisholm “General numerical methods for simulating second-order nonlinear interactions in birefringent media,” *Journal of Optical Society of America B*, vol. 14, pp. 2543–2549, 1997.
- [84] J. A. Fleck and M. D. Feit “Beam propagation in uniaxial anisotropic media,” *Journal of Optical Society of America*, vol. 73, pp. 920–926, 1983.
- [85] W. F. Ames, ed. *Numerical Methods for Partial Differential Equations*. Academic Press, Inc., 1992.
- [86] W. H. Press, ed. *Numerical recipes in C : the art of scientific computing*. Cambridge University Press, 1988.